The Key Laboratory of Weak Light Nonlinear Photonics,
Ministry of Education

Annual Report 2007

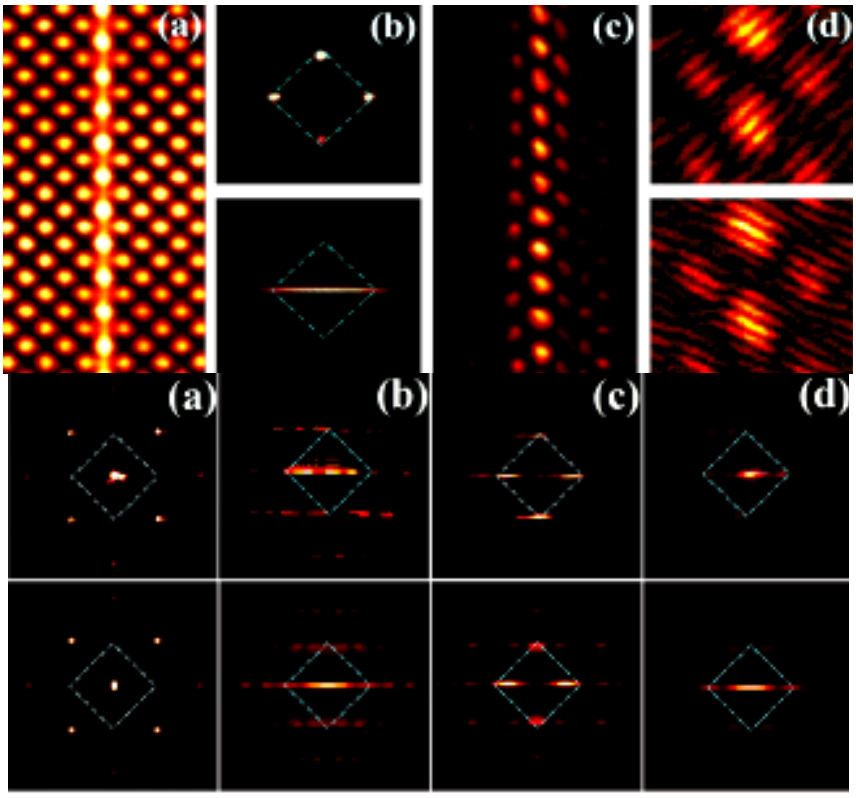

南开大学弱光非线性光子学

教育部重点实验室

Annual Report 2007

The Key Laboratory of Weak Light Nonlinear Photonics,
Ministry of Education

南开大学弱光非线性光子学

教育部重点实验室

◀▼在介观光学及其应用研讨会上，研讨会顾问委员甘子钊院士和实验室主任许京军教授分别致辞。

（2007.1.2-5）

▼ 南安普敦大学 Nikolay Zheludev 教授来我院进行学术访问。

（2007.4.19-21）

◀▼泰达学院为泰达应用物理学院新任院长 Romano A. Rupp 教授举行致聘仪式，许京军副校长为他颁发了聘书。

（2007.5.10）

◀ 香港大学 Kwong-Yu Chan 教授来我院进行学术访问。

（2007.5.17）

▼ “纳米生物科学中韩联合研讨会”参会人员合影。

（2007.8.27-29）

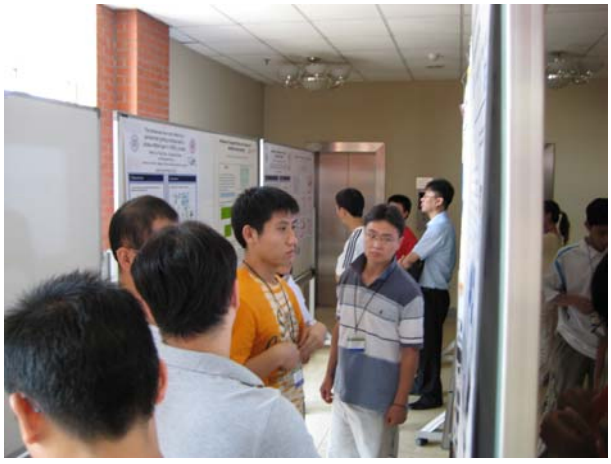

◀ ▼纳米生物科学中韩联合研讨会张贴报告会场和口头报告会场。

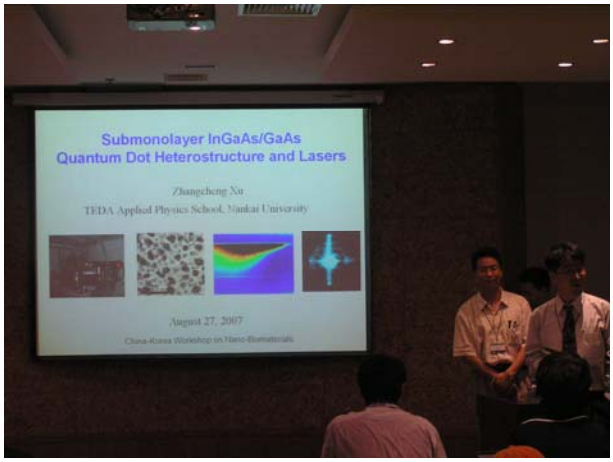

▼ 泰达应用物理学院院长 Romano A. Rupp 教授、明斯特大学应用物理学院院长 Cornelia Denz 教授和实验室主任许京军教授在中德暑期学校开幕式上。

（2007.9.10）

▼ “中德暑期学校：光学前沿-从非线性光学到极限光学”师生合影。

（2007.9.10-9.20）

▼ 弱光非线性光子学教育部重点实验室学术委员会扩大会议在泰达应用物理学院召开，重点实验室主任许京军教授和各方向负责人就实验室过去一年的工作做了汇报。

（2007.11.3）

◀▼学术委员会主任王占国院士主持了学术委员会会议，会议就重点实验室科研方向调整等问题进行了讨论并审批了实验室开放基金。

前　言/Preface

During the year 2007, the work at our lab was mainly focused on photonics materials and advanced fabrication techniques, weak light nonlinear optics and quantum coherent optics, spectral characterization and sensing technology, nonlinear physics and new photonics devices, semiconductor quantum photonics materials and devices. In this repost, we present a short summary of the results achieved in each line of activity of 2007.

All the activities summarised here have been done in the frame of international projects, cooperation agreements, and contracts with NSFC, MOE, MOST and Tianjin Municipal government. Without their supports, the progress in our research and education will never occur. Thank all these sponsors for their strong supports.

In addition, our staff and students spent some of their sleeping hours besides their waking hours on their research work and often made personal sacrifices in order to make our research better and faster. Thank you for your contributions to our own lab due to your wonderful research works.

We also benefit a lot from our colleagues from other units all over world, who provide us advices and supports. Many thanks.

Finally we are confident that what we will achieve more in the future.

Prof. Dr. Jingjun Xu

Director，The Key laboratory of

Weak Light Nonlinear Photonics

目　录/Contents

人员结构/Organization

实验室主任/Director

许京军　教　授

实验室副主任/Deputy Directors

张国权　教　授

孙　骞　教　授

学术秘书/Academical Secretary

禹宣伊　副教授

研究方向负责人/Research Group Leaders

弱光非线性及量子相干光学	许京军　教　授
非线性物理与光子技术	田建国　教　授
光子学材料及先进制备技术	孔勇发　教　授
光谱表征及传感技术	臧维平　教　授
半导体生长技术和半导体器件	舒永春　教　授

学术委员会/Academic Committee

主　任/Chairman

王占国　院　士

委　员/ Committee Members

沈德忠　院　士
薛其坤　院　士
姚建年　院　士
陈志刚　教　授
龚旗煌　教　授
陆　卫　研究员
田建国　教　授
王慧田　教　授
徐现刚　教　授
许京军　教　授
许宁生　教　授
资　剑　教　授

外籍学术顾问委员

D. Kip	教　授	德国 Cauthburge 大学
L. Hessenlink	教　授	美国斯坦福大学物理系
R. A. Rupp	教　授	奥地利维也纳大学实验物理所
T. Volk	教　授	俄罗斯国家晶体研究所
Y. Tomita	教　授	日本电气通信大学

杰出人才/Intelligent Staff

教育部“长江奖励计划”特聘教授
1999　许京军
2006　陈志刚

国家杰出青年基金获得者
1998　许京军
2001　田建国

教育部“优秀青年教师资助计划”入选者
2002　张国权
2003　宋　峰

教育部“跨世纪优秀人才培养计划”入选者
1998　许京军
2000　田建国
2001　孙　骞
2002　孔勇发

教育部“新世纪优秀人才支持计划”入选者
2004　张国权
2004　宋　峰
2005　臧维平
2005　李宝会
2006　徐章程

首批新世纪百千万人才工程国家级人选
2004　田建国

国家海外青年学者合作研究基金获得者
2005　陈志刚

“天津市授衔专家”称号获得者
2005　许京军
2005　田建国

教育部“长江学者和创新团队发展计划”创新团队基金资助

弱光非线性光子学重点实验室人员名录/Name List

研究人员/Scientific Staff（37 人）

王占国　许京军　田建国　Romano A. Rupp　陈志刚　张国权　孔勇发　孙　骞　宋　峰
臧维平　舒永春　徐章程　姚江宏　赵丽娟　刘士国　张　玲　朱　箭　曹亚安　孙甲明
张天浩　李玉栋　徐晓轩　张心正　周文远　乔海军　邢晓东　禹宣伊　余　华　吴　强
孙同庆　武　莉　楼慈波　高　峰　唐柏权　刘智波　李祖斌　薄　方

技术人员/Technical Staff（3 人）

黄自恒　陈绍林　马玉祥

行政人员/ administrative Staff（1 人）

梁　建

博士生/Ph.D Students（53 人）

蔡　卫　刘建彬　祁轶舲　唐莉勤　孙立萍　涂燕飞　潘雷霆　李　威　王振华　李　俊
宋道红　齐新元　窦宜领　胡　毅　柳永亮　李福新　陈树琪　叶　青　孙美秀　程　化
郝召锋　鄢小卿　李林枫　张　冰　刘智波　李祖斌　温宏胜　王文杰　曹永强　张冠杰
张雅婷　胡　欣　刘如彬　施曙东　于小晨　任相魁　王燕丽　刘淑静　韩　琳　王　喆
王俊俏　边　飞　张学智　任孟昕　郝志强　叶卓艺　李建威　刘富才　师丽红　刘加东
胡志键　崔国新　齐继伟

硕士生/M.S. Students（140 人）

殷长秋　刘龙昌　杨程亮　许宁宁　王慎之　钱学波　刘祥明　刘海旭　陈　聪　平维杰
杨　东　辛非非　段长莎　陈　楠　陈星宇　边　飞　张文定　刘莹莹　周　波　白香港
邵伟伟　徐玉惠　刘　宇　钱　坤　王秉慧　吴　超　刘春锋　王文娟　孟　扬　潘立彬
杨一宏　付世鹏　邢　冲　张力舟　张校亮　李　行　安保国　贺珍妮　南晓宇　朱宝刚
潘君成　张　森　张　婷　彭　灏　宋　宇　孙　磊　胡　茜　窦树岗　陈喜杰　王磊磊
董江舟　袁继翔　刘　刚　詹　鹤　吕　玮　于晓明　孙建成　安亚南　林军海　张雅婷
张　玲　马晓明　王玲玲　翟晓辉　王恩君　陈天琳　方扩军　王红旗　吴胜青　赵延雷
叶志诚　陈　晨　崔　楠　罗青青　李　丹　刘志伟　张　雁　程振洲　李　腾　曲菲菲
王青如　侯春宵　宋令枝　李俊梅　弭志强　蔡　虹　邹昌光　田　彬　张　鑫　宋　杰
陈　凯　周凯迪　孙秀峰　范　伟　杨　威　杨大鹏　张　攀　尹美荣　李奇楠　梁　兴
祁国春　杨正广　梅　灿　李　辉　石　凡　谭信辉　金妮娜　谢　楠　高光宇　胡金霞
惠王伟　张墨林　马雅盛　赵子宇　余　璇　梅剑春　曹　雪　张威威　张新霞　杨　阳
张俊杰　王静密　程　辉　王　醉　朱鸿雁　李昕睿　高冬子　匡元江　崔　磊　王利忠
周晓东　季鸣元　骆兰军　王文涛　赵红艳　樊学芳　李　伟　侯春宵　宋令枝　郑一凡

承担课题/Projects under Researching

序号	项 目 名 称	项 目 来 源	起止时间	负责人
1	纳/微结构非线性光学、光调控与器件应用研究	973 项目	2007.5-2012.8	许京军
2	人工结构材料的能带设计、制备和效应的基础研究	973 项目	2007.7-2008.12	陈志刚
3	介观光学与新一代纳/微光子器件研究	973 项目	2007.1-2011.12	孙骞
4	硅基发光材料与光互联的基础研究（南开部分）	973 项目	2007.7-2012.12	孙甲明
5	氧化物介观薄膜原子尺度可控制备与超快紫外器件研究（南开部分）	973 项目	2007.5- 2011.4	孔勇发
6	表面等离子体亚波长光学（SPSO）应用基础研究	973 项目	2006.1-2007.12	宋峰
7	光泵浦 1064nm 半导体垂直外腔表面发射激光器芯片材料的制备	863 项目	2006.12-2008.12	舒永春
8	四价掺杂铌酸锂晶体	863 新材料技术	2007.12-2010.11	孔勇发
9	基于掺镁近化学比铌酸锂的波长可调高速全光波长转换器	863 项目	2006.1-2008.12	陈云琳
10	关联光子学微结构阵列的光传输与调控研究	国家重大科学研究计划	2007.01-2011.12	田建国

11	量子相干系综的光学性	国家自然科学基金重点项目	2004.01-2007.12	许京军
12	新型结构高活性的纳米 TiO2 可见光催化剂的制备	国家自然科学基金	2005.1- 2007.12	曹亚安
13	半导体量子点激光材料瞬态光谱特性及超快现象研究	国家自然科学基金	2005.1-2007.12	姚江宏
14	光感应阵列波导中的分立衍射与分立孤子	国家自然科学基金	2005.1-2007.12	刘思敏
15	并行式飞秒激光三维纳米光子学微结构加工技术研究	国家自然科学基金	2005.01-2007.12	李玉栋
16	掺镁铌酸锂光学微结构级联二阶非线性频率变换的研究	国家自然科学基金	2006.1-2007.12	陈云琳
17	光强与时间控制的光学图像和信息处理器件的原理及技术研究	国家自然科学基金	2006.1-2008.12	张春平
18	光感应二维非线性光子晶体及其性能的研究	国家自然科学基金	2006.1-2008.12	孔勇发
19	卟啉有机超分子激发态光学非线性研究	国家自然科学基金	2006.1-2008.12	田建国
20	高活性可见光催化剂界面光生电荷转移的原位瞬态分析	国家自然科学基金	2006.1-2008.12	曹亚安
21	980nm InGaAs 亚单层量子点激光器	国家自然科学基金	2006.1-2008.12	徐章程
22	用宽带荧光上转换飞秒时间分辨光谱技术研究 CdS 纳米体系中超快弛豫过程	国家自然科学基金	2006.1-2008.12	赵丽娟
23	基于一维光自带隙结构的光限制效应研究	国家自然科学基金	2007.1-2009.12	臧维平

24	弱关联光子晶格体系中飞秒光传播特性及其导致的非线性光学效应	国家自然科学基金	2007.1-2009.12	吴强
25	光学相干周期微结构系综的光学性质	国家自然科学基金	2007.1-2009.12	张国权
26	光折变非线性表面光波导及其应用研究	国家自然科学基金	2007.01-2009.12	张天浩
27	紫外弱光非线性光子学效应、材料及器件	科技部国际合作重点项目	2005.01-2007.12	许京军
28	弱光非线性光子学效应、材料与器件的研究	长江学者和创新团队发展计划	2005.01-2007.12	许京军
29	铌酸锂晶体光子学基质平台的研究	教育部跨世纪优秀人才培养计划基金	2003.1-2007.12	孔勇发
30	弱关联光子学晶格体系中光波传播特性的研究	教育部新世纪优秀人才支持计划	2005.1-2007.12	张国权
31	稀土掺杂材料的发光与激光特性的研究	教育部新世纪优秀人才支持计划	2005.1-2007.12	宋峰
32	非线性光学机制研究	教育部新世纪优秀人才支持计划	2006.1-2008.12	臧维平
33	近红外有机/无机量子点复合材料和器件	教育部新世纪优秀人才支持计划	2006.1-2008.12	徐章程
34	弱光非线性光子学效应、材料及器件研究	教育部直属高校聘请外籍教师重点项目	2007.1-2007.12	许京军
35	多功能高分辨率 OCT 成像系统	天津市科技发展计划	2005.4-2007.12	田建国
36	高增益短长度光纤器件的研究	天津市攻关培育项目	2005.1-2007.12	宋峰

37	光泵浦 980nm 半导体垂直外腔表面发射激光器芯片的制备	天津市重点基金项目	2006.4-2008.12	舒永春
38	矿石检测小型化激光拉曼光谱仪	天津市科技支撑计划重点项目	2007.4－2009.10	徐晓轩
39	紫外弱光非线性光子学效应、材料及器件	天津市国际科技合作计划项目	2005.04-2007.12	许京军
40	若干新型弱光非线性效应及其应用的研究	天津市国际科技合作项目	2006.4-2009.3	张国权
41	弱光非线性光学新效应和机制	天津市科技创新能力与环境建设平台项目	2006.7-2009.6	孙骞
42	用相位编码方法在铌酸锂表面构造亚微米金属微结构	天津市自然科学基金	2007.4-2009.9	张心正
43	长江学者启动基金	985	2006.3-2009.2	陈志刚
44	InGaAs/GaAs 亚单层量子点的分子束外延生长	教育部留学回国人员科研启动基金	2005.1-2007.12	徐章程
45	引智项目	国家外国专家局	2007.1-2007.12	张心正
46	聚合物/无机量子点红外复合材料中的载流子动力学	中科院上海技物所红外物理国家重点实验室开放课题	2007.6-2009.6	徐章程
47	微流体系光动力学的基础研究	南开大学创新基金	2007.1-2008.12	禹宣伊
48	掺锆铌酸锂晶体抗光折变性能研究	南开大学创新基金	2007.1-2008.12	刘士国

仪器设备/Facilities

仪器设备名称	规格型号	购置时间
激光器工作站	899-29	2005.09
飞秒激光器	VF-T2S	2000.08
皮秒激光器	PY61	2003.11
纳秒激光器	Panther OPO	2003.11
光纤激光器	PLY-20-M	2003.11
可调频再生放大器	Spitfire F-1K	2000.04
时间分辨光谱及瞬态吸收光谱系统	Spectrapro.300i	2000.04
光谱分析仪	AQ6315A	2005.09
显微拉曼光谱仪	MKI2000	1998.09
分子速外延生长炉	Riber Compact 21T	2003.09
提拉法晶体生长炉	研制	2002.04
晶体切割研磨抛光系统	Logitech 系列	2001.06
扫描探针显微镜	Nanoscope ⅢIa	2006.08

注：除开放基金外，所有仪器设备均为有偿使用

研究工作报告/Scientific Report

非线性物理与光子技术/ Nonlinear Physics and Photonics Techniques

负责人：田建国

本研究方向涉及有机材料光学非线性、亚波长微结构、生物光子学、以及非线性表面波等方面。本年度发表论文 14 篇，申请发明专利 3 项；在研课题经费 273 万元。2007 年度“非线性物理与光子技术”方向主要在以下方面取得了进展：

Our research mainly focused on optical nonlinearities of organic materials, sub-wavelength microstructure, bio-photonics, and nonlinear surface waves. 14 papers have been published in international academic journals, and three patents applied for. The total fund is 2.73 millions. During this year we achieved some important results as following:

在有机材料光学非线性方面，我们对作为参考材料的二硫化碳进行了蓝光波段的非线性测量，发现在 420-460nm 的范围内二硫化碳具有较大的非线性吸收特性；其次，通过对卟啉的质子化的研究发现，相对于基本的四苯基卟啉，硫杂化卟啉质子化后在一个较宽的光谱范围内非线性吸收都有更大的提高；在卟啉修饰碳纳米管的光限制效应研究的研究中，取得了较大的进展，我们对三种不同卟啉共价连接修饰的碳纳米管的光限制效应进行了研究，发现卟啉修饰后的碳纳米管的光限制效应有较大提高，如图 1。通过对这三种卟啉修饰碳纳米管的紫外吸收和荧光特性的研究，我们认为光限制效应的提高除了反饱和吸收和非线性散射两种光限制机制的结合外，还可能有来自卟啉与碳纳米管之间光致电子转移效应的贡献。此外，我们将非线性测量的椭圆法和 Z 扫描法这两种测量方法结合起来，提出一种新的测量非线性系数的技术，它结合了椭圆法和 Z 扫描法的优点，使 $\chi^{(3)}_{xyyx}$ 的测量变得更简单。

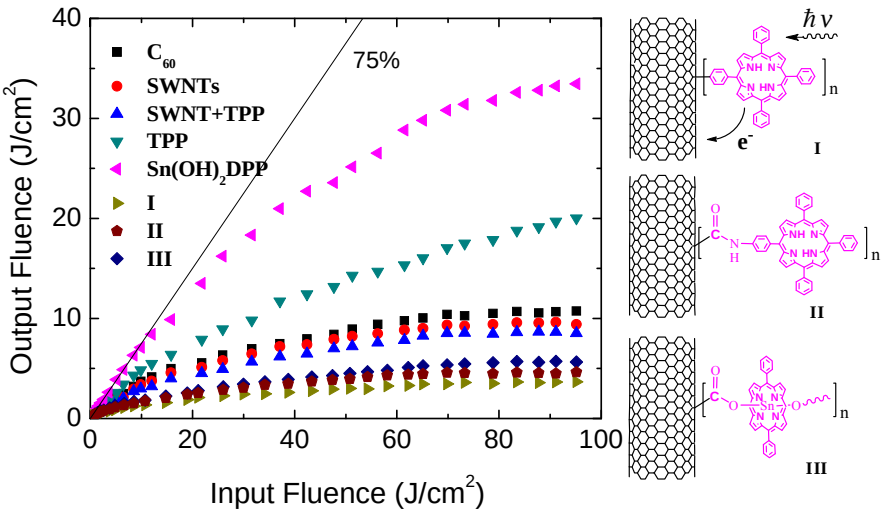

图 1 卟啉修饰单壁碳纳米管的光限制效应

Fig.1 Optical limiting of porphyrin-SWNT supramolecular system

Optical nonlinearities of organic materials, such as porphyrin, CS_2, have been measured. Firstly, nonlinear absorption of carbon disulfide was studied using nanosecond pulses, and large nonlinear absorption was found in the wavelength region of 420–460 nm. Secondly, the nonlinear absorption of two porphyrin diacids were studied and enhanced nonlinear absorption properties were found relative to their parent neutral complexes. Furthermore, the introduction of S-atoms into the porphyrin core makes it a better candidate for optical limiting relative to the simple porphyrin. Thirdly, in the studies of porphyrin-SWNT supramolecular system, three kinds of the porphyrins covalently functionalized SWNTs offered superior performance to C_{60}, the individual SWNT and porphyrins by combination of nonlinear mechanism of reverse saturable absorption and nonlinear scattering, and the photoinduced electron or energy transfer between porphyrin moiety and SWNT also play an important role in improvements of optical limiting effect.

在亚波长微结构的增透特性方面，我们尝试设计了可以使亚波长孔缝获得增强透射的新结构。相对于拥有同样出射孔径的普通狭缝，漏斗狭缝结构的透射率获得增强。如果在漏斗结构的出射面设置周期凹槽或者周期调制的介质膜，在适当条件下就可以得到准直光束发射。初步研究也发现，在不同形状凹槽的作用下，有两种增强透射机制存在，分别对应两个增强透射峰。

Enhanced transmission through sub-wavelength hole arrays and a single sub-wavelength aperture with periodic corrugations surrounded have been investigated extensively. We report the similar phenomenon through a funnel-type aperture with a sub-wavelength outlet in a thick silver film, which was obtained numerically by using finite-difference time-domain method. Properties of the transmission spectrum can be modulated by geometric parameters of the funnel-type aperture. With periodic grooves or dielectric gratings on the out-put surface of the structure, beaming light emission can be obtained.

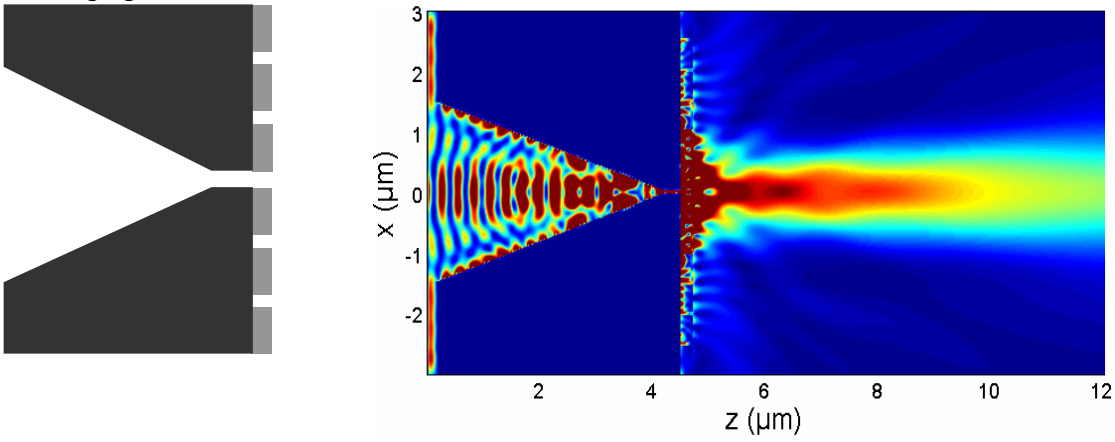

图 2 漏斗形狭缝的增强透射

Fig. 2 Enhanced transmission through sub-wavelength funnel-type aperture.

在生物光子学方面，我们研究了新型有机光色材料的光吸收特性以及光限制效应，理论计算了在非均匀光强照射下利用细菌视紫红质的光学新事物滤波器的特性及其分析，为新事物滤波器的实际应用提供了有用的信息。研究了生物组织表面的粗糙度对利用表面漫反射测量和拟合获得其光学性质的影响，其结果对生物组织光学性质的测量有重要的意义。

In the studies of bio-photonics, we investigated the light absorption properties and optical limiting effect of novel organic photochromic materials. Secondly, a nylon bar with different surface roughness is used as a simulation sample of biological tissue for the determination of optical properties by using the spatially resolved steady-state diffuse reflection technique. Results showed that the reduced scattering coefficient decreases with the decrease of the surface roughness of the nylon bar and reaches to a constant for the lower surface roughness, and the absorption coefficient increases with the decrease of the surface roughness of the nylon bar. Consequently, the optical properties of the tissues obtained by the spatially resolved steady state diffuse reflection technique should be modified.

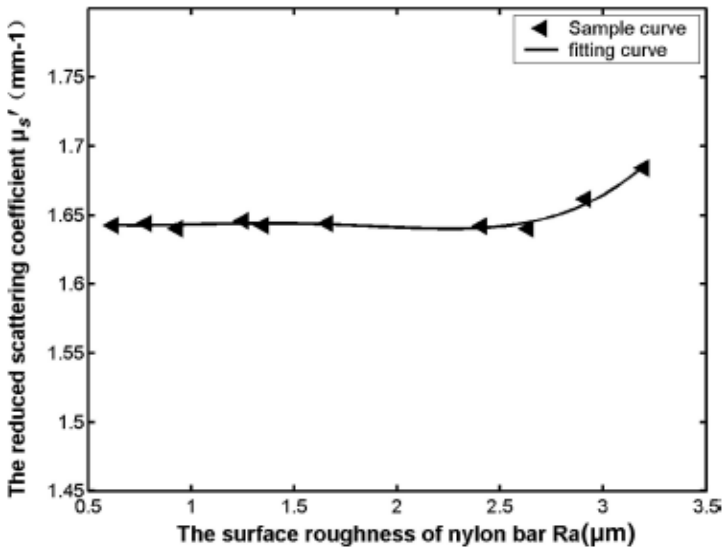

图 3 散射系数与尼龙棒表面粗糙度的关系

Fig.3 The reduced scattering coefficients as a function of the surface roughness *Ra* of the nylon bar.

在光折变非线性表面波研究方面，在 SBN 晶体表面实现了二次谐波产生的巨增强。开展了扩散、漂移、光生伏打等各种光折变非线性效应对 PR SW 影响。开展局域非线性如漂移、光生伏打非线性离散表面波的研究。漂移非线性具有很好的外电场调控特性，光生伏打非线性具有很强的弱光非线性特性，并且二者还具有可擦洗、固定的优越性。

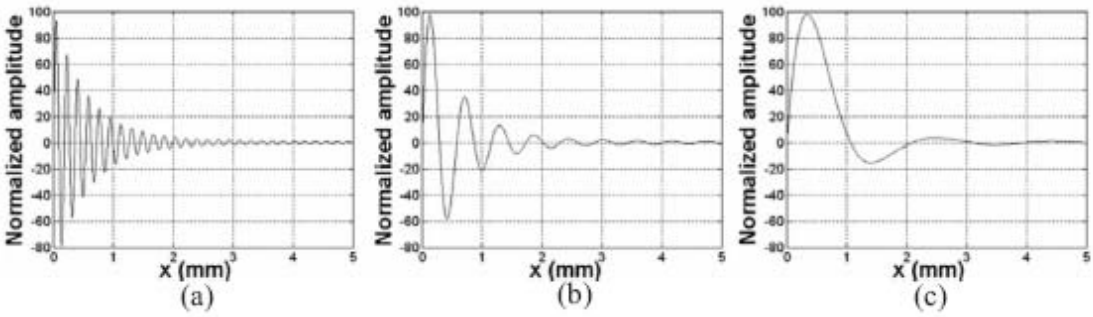

图 4 光折变表面波模型

Fig.4 Profile of the PR SW modes with a diffusion mechanism

A giant enhancement of surface SHG excited by the photorefractive surface waves was

observed at the surface of the $BaTiO_3$ and $Sr_{0.6}Ba_{0.4}NbO_3$(SBN:60) crystals The photorefractive surface waves with photorefractive nonlinearity of diffusion, drift, and photovoltaic effect is studied numerically for the first time. We found out that the essential cause of photorefractive surface waves is diffusion mechanism, but not drift and photovoltaic effects. The photovoltaic effect only has strong influence on the profile of photorefractive surface waves; the applied external electric field can also change the profile of the surface waves, and even destroy the mode upon a threshold, which provides a possible method to transform the modes of surface waves between high-frequency modes and low-frequency modes.

光子学材料及先进制备技术/ Photonics Materials and Advanced Fabrication Techniques

负责人：孔勇发

本方向涉及非线性光学晶体、微晶玻璃陶瓷、光子学微结构、纳米光子学、低维功能材料等方面。本年度发表论文 20 篇，其中影响因子 3.0 以上文章 6 篇；获得发明专利一项，申请发明专利 4 项。在研课题经费 306 万元。取得的代表性成果如下：

In this field, we mainly focused on the nonlinear optical crystals, micro-crystal glass ceramics, photonic microstructure, nano-photonics, and nanoparticulate films. 20 papers were published in international academic journals, including 6 papers with impact factor more than 3.0, and one patent was issued and four patents applicanted. The total reasearching founds are more than 3 millions. This year, we obtained some important results, they are mainly shown as following:

发明了掺锆铌酸锂晶体，其抗光折变能力达到 2.0×10^{7} W/cm^2 以上（如图 1），比掺镁铌酸锂晶体高两个量级以上，光致折射率变化饱和值仅有 7.1×10^{-7}，比掺镁铌酸锂晶体低一个量级；且掺杂阈值仅为 2.0 mol%，远低于掺镁铌酸锂晶体的 4.6 mol%，分凝系数也比镁更接近于 1.0，易于生长高光学质量单晶。因此掺锆铌酸锂晶体是比被誉为“中国之星”的掺镁铌酸锂晶体更加优异的抗光折变非线性光学材料，具有更加广阔的应用前景。

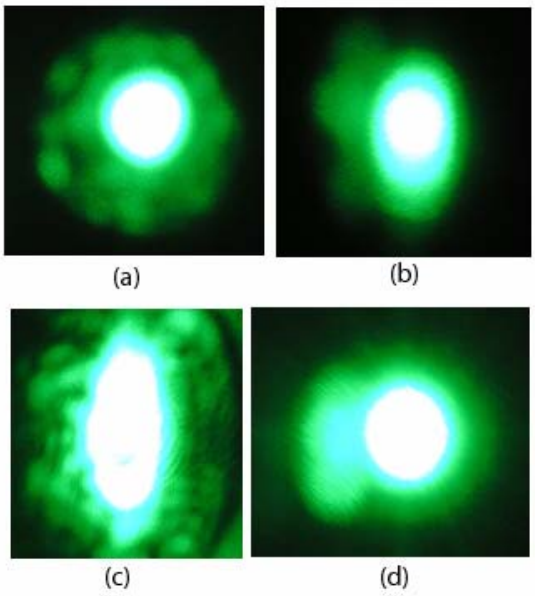

图 1 用 514.5nm 氩离子激光照射 5 分钟后掺锆铌酸锂晶体的透射光斑
样品：(a), (b) and (c) Zr1.7LN；(d) Zr2LN. 光强：(a) 1.3×10^{3} W/cm^2, (b) 1.3×10^{4} W/cm^2, (c) and (d) 2.0×10^{7} W/cm^2.

Fig.1 Distortion of transmitted argon laser beam spots after 5 min of irradiation.
(a), (b) and (c) Zr1.7LN; (d) Zr2LN. The light intensities are
(a) 1.3×10^{3} W/cm^2, (b) 1.3×10^{4} W/cm^2, (c) and (d) 2.0×10^{7} W/cm^2.

ZrO_2-doped lithium niobate crystals were grown. The doping threshold for optical damage resistance is below 2.0 mol% ZrO_2 while the distribution coefficient is close to one. Above threshold the optical damage resistance of ZrLN is two orders of magnitude higher than that of Mg6.5LN. The refractive index change of sample Zr2LN is one order of magnitude smaller than that of sample Mg6.5LN. The experimental results support the conclusion that ZrLN might replace

MgLN since it has better properties and possibly a broader range of practical applications.

采用提拉法生长出透明的 Er^{3+}:$KLa(WO_4)_2$（简称 Er:KLW）晶体，并确定了较佳的生长工艺。X 射线粉末衍射分析结果表明该晶体为四方晶系白钨矿结构（$I4_1/a$ 空间群），晶格常数为 a＝b＝5.444(3)Å，c＝12.120(6)Å。测量了 Er:KLW 晶体的拉曼谱，发现了 380cm^{-1}、450cm^{-1} 和 808cm^{-1} 等钨酸根的特征振动峰。测量了晶体的吸收光谱，应用 J-O 理论计算了晶体中 Er^{3+}离子的强度参量(Ω_2,Ω_4,Ω_6)；荧光光谱测量结果表明该晶体在 1529nm 附近有很强的荧光发射峰，利于产生受激辐射。Er^{3+}、Yb^{3+}双掺的 $KLa(WO_4)_2$ 晶体被初步生长，相关性质的研究正在进行中。

The transparent Er^{3+}:$KLa(WO_4)_2$ crystal was grown used by Czochralski method. The result of X-ray diffraction shows that the crystal belongs to space group $I4_1/a$ and the lattice parameters are a＝b＝5.444(3)Å，c＝12.120(6)Å. The Raman spectrum was measured at room temperature, and the characteristic peaks of tungstate group have been found. The intensity of parameter Ω of J-O coefficients were calculated by the absorption spectrum. The results of the fluorescence spectra show that the strong fluorescence emission peak was around 1529nm. Er^{3+}/Yb^{3+}:$KLa(WO_4)_2$ crystal was grown tentatively, and the related properties was studying.

构建了 Na_2O-SrO-B2O_3 体系富硼区相图，同时用粉末法解析了新化合物 $NaSrB_5O_9$ 的晶体结构。生长了新化合物 $Na_3SrB_5O_{10}$ 的单晶体，并进行结构解析。鉴于该化合物的网络状硼氧基团结构，尝试进行 Eu^{3+}离子掺杂，无须还原气氛可将 Eu^{2+}离子稳定在室温。合成新化合物 $NaMgBO_3$ 并用粉末从头算法进行了晶体结构解析，并深入分析了结构与性质的关系，该化合物可能具有较大的双折射。发现系列锂硼酸盐，具有潜在的离子导电性质。构建 K_2O-MgO-B_2O_3 体系相图，并合成一个新的三元化合物。

The subsolidus phase relations of the B-rich part of the ternary systems Na_2O–SrO–B_2O_3 was determined. The crystal structure of new compound $NaSrB5O_9$ was refined by Rietveld method. High quality single crystal of $Na_3SrB_5O_{10}$ was selected for single crystal diffraction, and the structure was determined. The three dimensional net-work structure of BO groups makes the compound possible to stabalize the doped Eu^{3+} into Eu^{2+} without a reducing atmosphere. A novel orthoborate, $NaMgBO_3$, has been successfully synthesized by standard solid-state reaction, and the crystal structure has been determined from powder X-ray diffraction data. Isolated planar $[BO_3]^{3-}$ anionic groups were found as the fundamental building units. The subsolidus phase relations of the ternary systems K_2O–MgO–B_2O_3 have being investigated. A new ternary compound was found and the structure determination is underway.

对于氟氧化物玻璃陶瓷中红外波段的荧光发射进行了详细的研究，其在 1530nm 除具有较宽的半宽，适合光纤材料。成功制备出 Tm^{3+}/Yb^{3+}的掺杂蓝色上转换发光玻璃陶瓷材料，其上转换蓝色荧光肉眼可见。制备了透明碲酸盐玻璃基质。实验中发现可以通过热处理的方式在玻璃基体中构造纳米级的微晶，并可通过腐蚀的方式获得粉末状纳米团簇，现在已经可以通过分散剂的作用获得 100nm 左右的均匀粉体，具体研究正在进行中。

The emission at 1530nm and its application are discussed in optical communications at glass ceramics co-doped with Er^{3+} and Yb^{3+} ions. Under the excitation of 785nm laser, the emission

integral intensity of 1530nm increases about five times in the glass ceramics than that in the glass. The results indicate that it is a promising candidate for developing broadband optical amplifiers in wavelength-division multiplexed (WDM) system. The blue up- conversion luminescent glass ceramics co-doped with Er^{3+} and Yb^{3+} ions are prepared, which have bright blue emission excited by 980nm laser. The inorganic nanoparticles are prepared by glass corrosion method. The nanoparticle size is about 100nm and homogeneous disperse.

以光栅衍射理论为基础，从理论上分析研究了微结构晶体衍射效率与占空比和折射率的关系。采用波长为 532nm，最大功率为 80mw 的连续激光为光源，分别对周期极化掺镁铌酸锂微结构晶体和周期极化同成分铌酸锂微结构晶体的占空比及极化反转引起的折射率变化进行了测试。在实验研究过程中，准确的测得了微结构晶体的周期、占空比和折射率的变化等重要参数。与此同时，通过分别测量两种不同样品折射率的变化，发现掺杂对极化微结构晶体折射率改变影响较大。通过该实验，我们提供了一种新的无需和晶体直接接触，更不需要对晶体进行化学腐蚀的微结构探测方法。

Based on the grating diffraction theory, the duty cycle and refractive index change of the periodically poled microstructure (PPMS) crystal are studied theoretically by light diffraction efficiency. The duty cycle and refractive index change of both PPMS $LiNbO_3$:MgO and PPMS $LiNbO_3$ were investigated using a laser of wavelength 532nm and maximal power 80mw, respectively. The refractive index change of PPMS $LiNbO_3$:MgO is larger than that of PPMS $LiNbO_3$.

对准相位匹配光参量振荡器进行了理论研究，推导了聚焦高斯光束条件下准相位匹配光参量理论，详细讨论了准相位匹配单谐振参量振荡器中各参数对参量增益以及振荡阈值的影响，给出了谐振腔及晶体长度、抽运光脉宽以及信号光输出透过率同泵光能量阈值的定量关系。在此理论研究的基础上，对准相位匹配周期极化掺镁铌酸锂微结构光学参量振荡进行了实验研究。通过改变微结构周期，实现了信号光从 1.45~1.72μm 的输出，最小阈值为 30μJ。在温度 30℃，抽运功率为 300mW，最大信号光输出为 56mW，斜率效率达 18.7%。由于掺镁铌酸锂微结构抗光损伤性能显著提高，无需在高温下进行运转，使得掺镁铌酸锂微结构光学参量振荡器在常温条件下实现连续运转成为可能。

Based on analyzing optical parametric oscillator (OPO) in the quasi-phase- matched condition, the relationship between the grating period and parametric gain has been discussed in singly-resonant optical parametric oscillators in this work. Then, the dependence of threshold energy on the cavity length, the crystal length, the pump pulse width and the signal wave output coupling were analyzed in detail. Finally, the theory in this work was proved applicable by our experiments. Pumped by Q-swithed Nd:YAG laser, using different periods of PPMgLN, a tunable signal wave from 1.45~1.72μm was obtained. At 30°C, signal output of 56mW was obtained with a pump power of 300mW, and the slope efficiency was 18.7%. PPMgLN OPO can operate continuously at room temperature for its higher resistance against photorefractive damage. Moreover, it demonstrated that the size of PPMgLN OPO may be improved comparing to PPLN OPO.

发现了斜切 Si(111)表面的 Ge 微米线的自组织生长现象。如图 2 所示，在斜切角小于 0.1 度的 Si(111) 表面上形成了 Ge 岛（图 2a），而在斜切角为 4 度的 Si(111)表面上形成了 Ge 微米线阵列（图 2b）。发现了原位退回量子点材料可以减小压电场效应对量子点辐射寿命的影响。如图 3 所示，InGaAs/GaAs 量子点经过原位退火后，发光效率（载流子寿命）提高（减小）。成功制备出了具有宽吸收带的 MEH-PPV/PbS 量子点复合材料，为研制高性能的光伏器件，研究纳米复合材料的光学性质打下了基础。

We discovered the self-organized Ge micro-wires grown on vicinal Si (1 1 1) surfaces. As shown in Fig. 2a), when the mis-cut angle of Si (1 1 1) surface is less than 0.1 degrees, Ge islands will be formed. However, when the mis-cut angle is 4 degrees, array of Ge micro-wires will appear (Fig. 2b). We found that in-situ annealing of quantum dot materials can reduce the effect of piezoelectric field on the radiative lifetime. As shown in Fig. 3, the emission efficiency (carrier lifetime) of InGaAs/GaAs quantum dots will increase (decrease) after in-situ annealing. MEH-PPV/PbS quantum dot composite with wide absorption band has been successfully synthesized. This material will be used to fabricate high-performance photo-voltaic devices. And the optical properties of this kind nano-composite will be investigated in the near future.

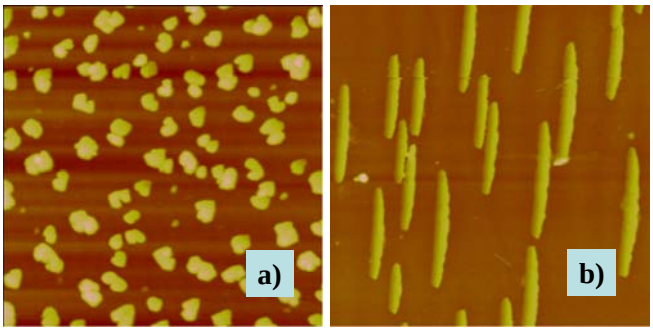

图 2　Si (111)上生长的 Ge 结构的原子力显微镜图片(5×5 μm^2).

Fig.2　The AFM images (5×5 μm^2) of Ge on Si (1 1 1) surfaces.

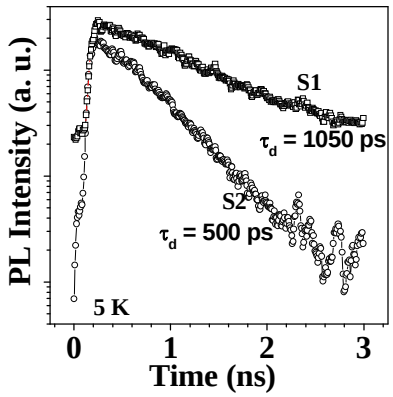

图 3　InGaAs/GaAs 量子点的瞬态光致发光谱，S1 和 S2 分别表示未退火和退火的样品

Fig.3　The transient PL spectra of InGaAs/GaAs quantum dots. S1 and S2 represent the as-grown and annealed samples, respectively.

采用溶胶-凝胶制备方法和掺杂调控技术，研制出系列 In 离子掺杂高活性纳米 TiO_2 可见

光催化剂, 如：$Ti_{x-1}O_2$-In_x, $Ti_{x-1}O_2$-In_x-N, $Ti_{x-1}O_2$-In_x-N-Sn。该系列催化剂的紫外-可见光催化活性已超过 N 离子掺杂 TiO_2 可见光催化剂。研制出纳米 $Ti_{(1-x)}Zr_xO_2$ 固溶体催化剂、B 离子掺杂 TiO2-xBx 催化剂和镍离子表面处理的 TiO_2 催化剂。研究其能带结构，并分析了紫外-可见光催化机理。

Using sol-gel method and doping technology, prepared series In ion doped high visible photocatalytic activity nano-TiO_2 catalyst, such as $Ti_{x-1}O_2$-In_x, $Ti_{x-1}O_2$-In_x-N, $Ti_{x-1}O_2$-In_x-N-Sn. Both the UV and visible light photocatalytic activity of this series catalysts is higher than the N doped TiO_2 catalyst. Part of these results has applied for three patents. Developed nano- $Ti_{1-x}Zr_xO_2$ solid solution catalysts, B doped $TiO_{2-x}B_x$ catalysts and TiO_2 catalysts with surface modified by Ni^{2+}. Furthermore, studied on the band structures of these catalysts and analyzed the mechanisms of photocatalysis in UV and Vis light.

利用掺杂、自组装等技术，制备出 TiO_2 可见光纳米管（如图 4）、海胆状 TiO_2 纳米球生长纳米金粒子（如图 5）、CuO 二维表面纳米结构薄膜、ZnO 纳米柱等特种纳米结构材料，并进行超疏水、超亲水和可见光催化等功能性研究，建立制备新型光电功能材料的新技术。

Prepared the TiO_2 nanotube with visible light response（Fig.4）, Au/TiO_2 sea-urchin-like micrometer-scale spheres（Fig.5）, the two dimension surface nanostructures CuO film and ZnO nanocolumn and other special nanostructures materials. And researched the functionality of these materials, such as super-hydrophilicity, super-hydrophobicity and visible light photocatalysis. Novel methods of preparing new photoelectric functional materials have established.

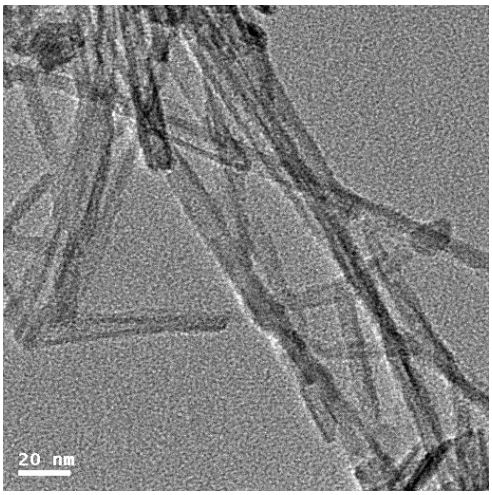

图 4　TiO_2 可见光纳米管

Fig.4 The TiO_2 nanotube with visible light response

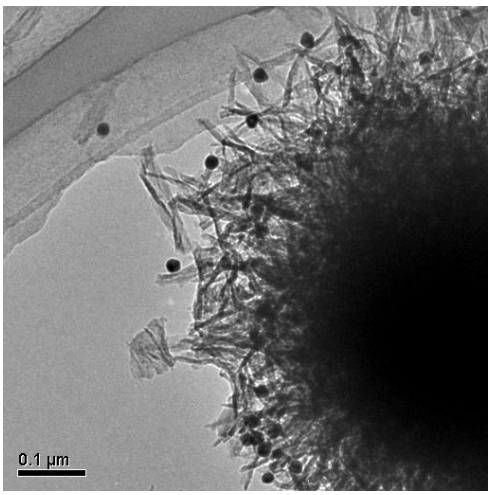

图 5 海胆状 TiO_2 纳米球生长纳米金粒子

Fig.5 Au/TiO_2 sea-urchin-like micrometer-scale spheres

弱光非线性及量子相干光学/ Weak Light Nonlinear Optics and Quantum Coherent Optics

负责人：许京军

本方向主要开展微/纳结构制备、微/纳非线性光调控、量子非线性光学与调控、飞秒超快探测技术以及光折变材料与新效应等方面的研究。2007 年度本方向共发表论文 24 篇，撰写英文专著章节 2 章，主要取得如下进展：

The main research topics in this group are fabrication of micro/nano-structure, nonlinear optical manipulation in micro/nano-structure, quantum nonlinear optics, ultrafast detection and analysis by using fs technology and photorefractive nonlinear optics. We published 24 papers in various academic Journals and contributed 2 book Chapters for “Photorefractive Materials and Their Applications 3” (Springer Series in Optical Science) and “Nonlinear Optics and Applications” (Research Signpost). The main research progresses in 2007 are as follows.

我们设计了层叠体光栅结构，研究表明层叠体光栅结构具有很强的结构色散效应，可以实现对光速有效的调控。理论计算表明，对于相同厚度和光栅结构参数，层叠体光栅的光速调控能力可以得到几个数量级的增强（依赖于光栅的总长度），并且通过选择适当的光栅结构参数，可以保持慢光或者快光脉冲较高的透过率，这对于实际的器件应用来说是非常重要的。

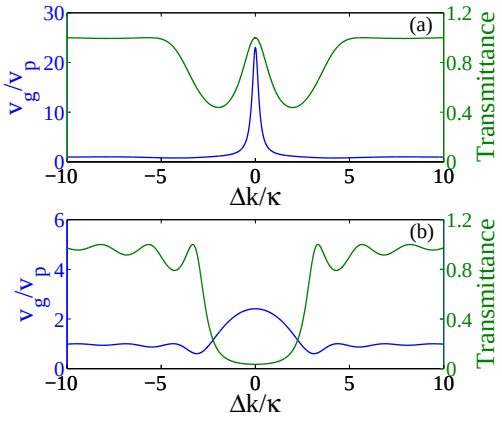

图1. 层叠体光栅(a)和均匀体光栅(b)的光速调控能力（蓝色线）和透过率（绿色线）比较。

Fig. 1 Transmission (green curves) and normalized group velocity (blue curves) for the stratified and phase-shifted gratings (a) and the homogeneous gratings (b), respectively.

We designed a stratified and phase-shifted volume index grating. This stratified and phase-shifted volume index grating was found to have a very strong dispersion, and therefore, was able to modify the group velocity of lights. We showed that the ability to control the group velocity of lights was significantly enhanced for the stratified and phase-shifted grating as compared to the homogeneous grating with same grating parameters. Furthermore, it is possible to keep high transmission for delayed/advanced light by selecting appropriate grating parameter. The high transmission is very important for practical device applications.

理论研究表明，在红宝石晶体中利用粒子数的相干布居振荡效应只能实现慢光效应。我们在红宝石晶体中不仅实现了慢光，而且观测到超光速传输现象。我们认为红宝石晶体中不仅存在由粒子数相干布居振荡效应所引起的慢光传输，同时还存在由非简并光波位相耦合的色散效应所引起的光速调控效应。由于光波位相耦合过程的色散效应既可以产生慢光，也可以产生超光速传输现象。因此，由于两种机制之间的竞争，在适当条件下，既可以产生慢光传输，也可以产生超光速传输。同时，我们还分析了光脉冲在传输过程中发生畸变的原因。

Based on the coherent population oscillation effect, it was proved theoretically that only slow light can be observed in ruby. However, we observed not only slow light but also fast light in ruby at appropriate conditions. We believe that a dispersive nondegenerate wave-mixing is responsible for the observed fast light. The dispersive nondegenerate wave-mixing can lead to slow lights as well as fast lights, and fast light appears when the nondegenerate wave-mixing with a negative dispersion slope dominates. We also analyzed the pulse profile deformation during the pulse propagation in ruby.

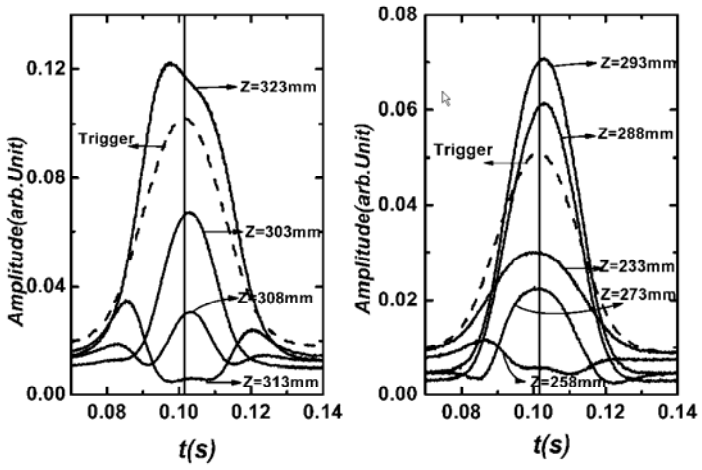

图2. 光脉冲经过10cm长的红宝石晶体之后波形，显示出慢光传输和超光速传输现象，其中虚线所示的是参考脉冲波形，实线为不同间距Z条件下的透射脉冲波形。

Fig. 2 Pulse profiles after the ruby showing the slow light and fast light propagation. The dashed curve is the reference pulse, while the solid curves are the transmitted pulse at various distance z.

带隙孤子作为非线性周期介质的一种基本现象已经在生物、凝聚态物理、玻色-爱因斯坦凝聚及非线性光学等系统中被广泛地研究。近年来在周期性光学系统中，国际上几个实验小组通过相位整形或布拉格角入射激发的方式实现了落于第一布拉格反射禁带空间带隙孤子。我们在SBN晶体中通过自散焦光学非线性制备了二维脊背型光子晶格，并研究了其带隙孤子的形成与性质。我们的实验发现即使是单束光正入射（图3c）的情况下，通过合理控制非线性的强度同样可以实现带隙孤子（如图3e）。干涉图（图3f、g）清晰地显示了第一带隙孤子所固有的棋盘式的相位关系结构（邻近点反相位）分布；非线性空间频谱图（图3h）也由线性情况下覆盖整个第一布里渊区（图3d）聚集到反常衍射区的四个M高对称点。相近参数下的数值模拟（图3底行）也进一步证实了我们的实验结果。

The formation of gap solitons is a fundamental phenomenon of wave propagation in

nonlinear periodic media. It has been studied in various branches of science including biology, condensed matter physics, Bose-Einstein condensates, as well as nonlinear optics. Typically, these gap solitons were observed with off-axis excitations in which the probe beam was launched at an angle to match the edge of the first Brillouin Zone (BZ). We reported the first theoretical prediction and experimental demonstration of spatial gap soliton by a single-beam on-axis excitation in a self-defocusing photonic lattice. These gap solitons have their propagation constant residing in the first bandgap of the periodic lattice. While a narrow circular beam can evolve into a 2D gap soliton as long as its k-space spectrum covers the entire first BZ (or more precisely, the four high-symmetry M points of the first Bloch band), self-trapping of a narrow stripe beam (whose spectrum is anisotropic and covers only two opposite M points) into a gap soliton is nontrivial. We monitor the nontrivial staggered phase structure of the gap solitons by interferograms and the far-field BZ spectrum.

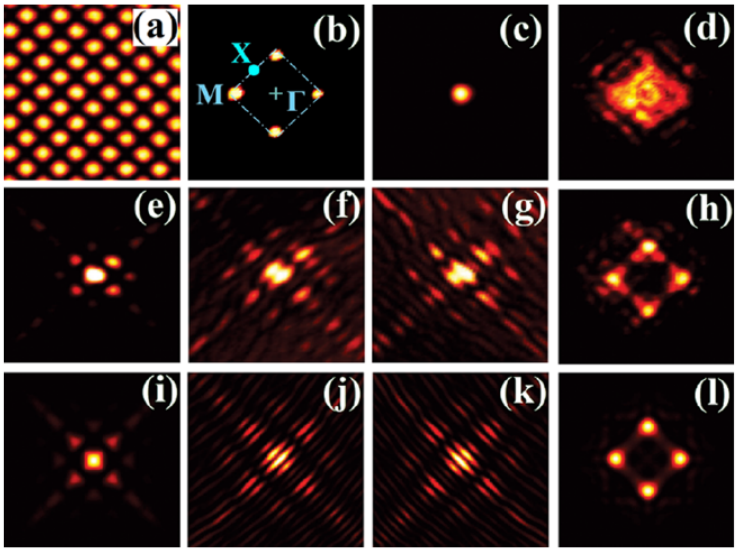

图3. 二维自散焦光子晶格中带隙孤子的形成、空间频谱及其空间相位分布。

Fig. 3 The formation, the spatial power spectrum and the phase structure of the gap soliton in a 2D self-defocusing photonics lattice.

在进一步的实验中，我们通过对非线性的控制成功地将入射到光子晶格中的一束条形光（图4a）演化到带隙孤子串（图4c）。首次实现利用带隙孤子串在非线性周期晶格中诱导线缺陷。更为有趣的是非线性空间频谱（图4b下）在竖直方向无激发（图4b上）的情况下的上下两个M对称点上也出现能量。说明带隙孤子的激发并不需要严格的带边激发，打破了传统认识上的激发要求，更有利于带隙孤子的实现。

Surprisingly, we find that a stripe beam can evolve into the gap soliton train (whose spectrum covers all four M points after nonlinear spectrum reshaping), suggesting that a gap soliton can arise from Bloch modes even if these modes are not initially excited or weakly excited. The gap soliton trains could be considered as nonlinearity-induced line defects in photonic bandgap structures.

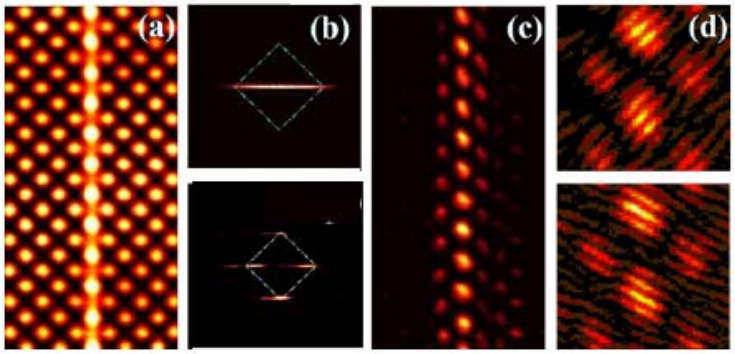

图4. 二维自散焦光子晶格中带隙孤子串的形成、空间频谱及其空间相位分布。

Fig. 4 The formation, the spatial power spectrum and the phase structure of the gap soliton train in a 2D self-defocusing photonics lattice.

在光诱导“脊背”型光子晶格中我们还首次实现反相位和同相位类偶极带隙孤子对（如图5）。从相位和空间频谱分布图我们可以清晰地区分线性和非线性态的不同特征。理论分析发现，其稳定性取决于初始的激发态。

We reported the experimental demonstration of dipole-like spatial GSs in a two-dimensional (2D) optically induced “backbone” lattice with a saturable self-defocusing nonlinearity. Our experiments showed that two mutually coherent dipole-like beams (out of phase or in phase) can evolve into a self-trapped state. The spatial power spectra and phase structures of these dipoles were dramatically different for linear and nonlinear propagation. Our theoretical analysis showed that the stability of these high-order solitons depends strongly on the initial excitation conditions (such as relative location and phase between the two beams).

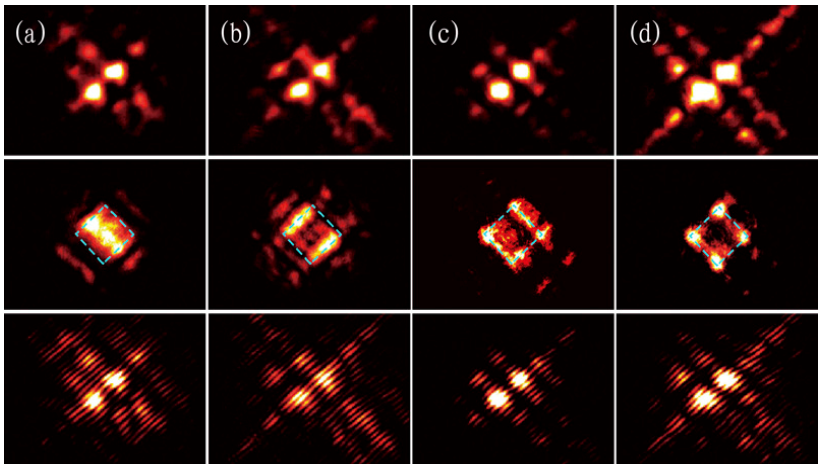

图5 对角激发类偶极带隙孤子实验结果。其中(a,b)是同相位，（c,d）是反相位。图(a)和(c)分别是线性情况。图(b,d)分别是非线性情况。从上至下分别是光强分布图、傅立叶面光谱图、干涉图。图中蓝色虚线框代表第一布里渊区。

Fig. 5 Experimental results on in phase (a,b) and out of phase (c,d) dipole-like gap solitons under diagonal excitation. Shown are output patterns (top), corresponding Fourier spectra (middle), and interferograms (bottom) for linear (a, c) and nonlinear (b, d) propagation.

利用铌酸锂晶体的自散焦效应，我们在铌酸锂晶体中构建了“脊背”型光子学晶格。当探测光正入射或者以布拉格角入射，在格点激发或者格点间隙激发等四种激发条件下，分别实现了带隙孤子，并研究了带隙孤子形成过程中其空间功率谱的能量转移过程。此外，利用棱镜耦合法观测了一维光子晶格中的离散孤子，通过一个柱面镜可以实现反常衍射和饱和自散焦非线性的平衡，从而十分方便地激发导带以及禁带中的孤子。实验结果和理论模拟相符得很好。

We fabricated a backbone nonlinear photonics lattice in the self-defocusing lithium niobate crystal. We observed the formation of four kinds of gap solitons in this backbone nonlinear photonics lattice with normal incidence or Bragg-angle incidence at on-site or off-site excitation. The energy transfer during the formation of gap soliton in the k-space was studied. In addition, pure mode solitons were observed by prism coupling method in one-dimensional periodic optical media. With the help of a cylindrical lens used in a prism coupler retroreflective scheme, linear modes in conduction bands and extended nonlinear modes inside forbidden gaps of a waveguide array in lithium niobate are easily excited in numbers of channels to balance the anomalous diffraction and the saturable defocusing nonlinearity. The results are coincided with numerical calculations.

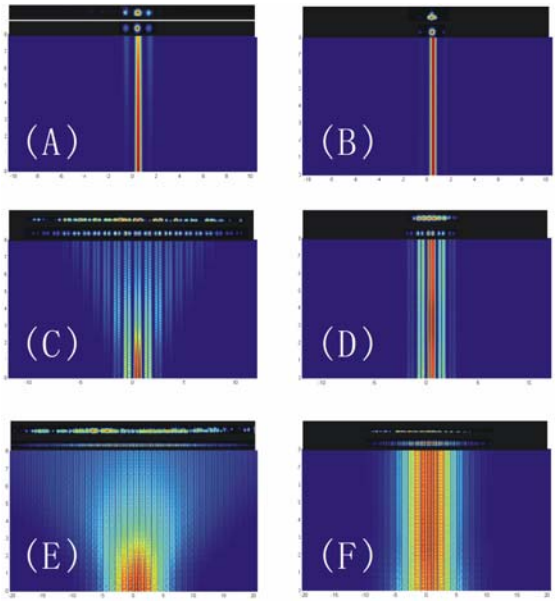

图6 离散孤子的理论模拟和实验结果（每幅小图上方为实验结果，下方为晶体中光传播的模拟图），左侧三图为线性情况，右侧三图为离散孤子情形。

Fig. 6 Experimental observation and simulation of discrete soliton. Experimental images at the output crystal face are superimposed on the theoretical plots showing propagation dynamics inside the crystal. (B) (D) and (F) are solitons, (A) (C) and (E) are linear cases.

我们使用飞秒激光在纯水中制备出银的纳米颗粒，并测量了纳米颗粒悬浊液的吸收光谱，发现了吸收峰的红移现象。利用原子力显微镜和动态光散射研究了纳米颗粒的形状以及大小分布，发现制备出的纳米颗粒主要有两类，一类大小约为 30nm，另一类大小约为 120nm。

纳米颗粒的大小可以很容易通过实验条件来操控。

Silver nanoparticles were fabricated in water by femtosecond laser pulses. The optical properties of the silver nanoparticles were studied by UV-Vis absorption spectrum. And the shape and the size disitribution of the nanoparticles were measured by an atomic force microscope and dynamic light scattering, respectively. The results showed that there were two kinds of nanoparticles. One was the small particles with diameter about 30nm, the other was the large one with diameter about 120nm. The diameter of nanoparticles could be easily controlled by experimental conditions

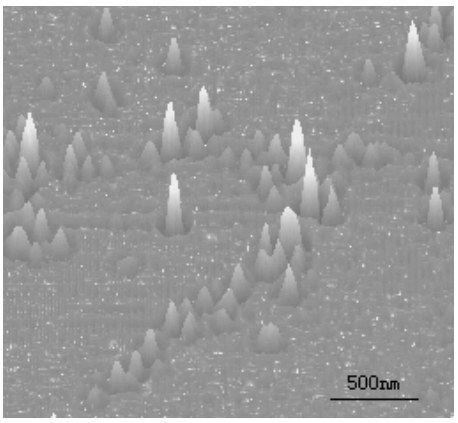

图7 原子力显微镜下的银纳米颗粒形貌图。

Fig.7 The Shape of silver nanoparticles by Atomic Force Microscope.

研究了数字式弱光探测和强度相关测量的理论和工作原理，并对构建的实验平台的性能检测和优化。我们利用数字式弱光探测和强度相关测量平台，系统地研究了弱激光一阶相干性、热光和准热光的二阶相干性，以及热光和准热光的光子统计性质，重点讨论了测量中的取样时间对时间结果的影响。在对光子统计性质的研究中，我们提出了更适于描述光场统计性质的约化 Q 参数，即<Q>的概念，并展示了<Q>相比 Mandel 定义的 Q 参数在表征的时间依赖光子统计上的优势。

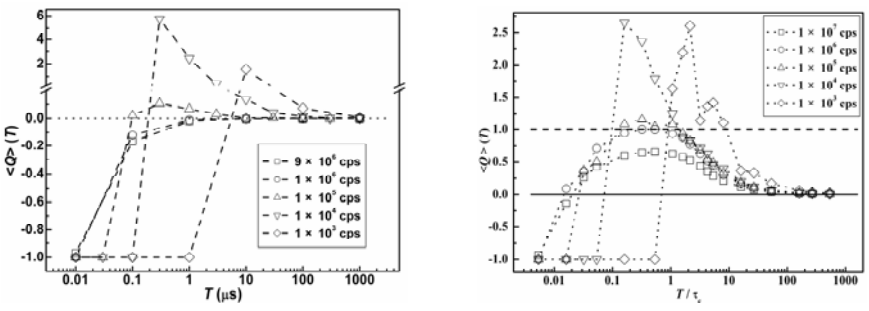

(a) (b)

图8 不同平均光功率下光场的<Q>参数对取样时间的依赖: (a) 弱激光；(b) 准弱光。

Fig. 8 The dependence of normalized Q parameter on sampling time under different light intensity: (a) laser, (b) pseudo thermal light.

The principle and theories of digital measuring technique of weak light and measurement of coherence and light intensity correlation were systemically introduced. Then the characterization and the optimization of the experimental setup were investigated in detail. Using this setup, we systemically studied the first-order coherence, the second-order coherence, and the statistical properties of strongly attenuated laser; as a contrast, the second-order coherence and the statistics of strongly attenuated pseudo thermal light were also studied. During the measurements, the influences of experiment conditions, especially sampling time on the results were discussed. When we investigated the photon statistics of both the laser and pseudo thermal light, we introduced a new parameter named as normalized *Q* parameter, and presented its advantage in characterizing photon statistics over the original *Q* parameter defined by Mandel.

本方向 2007 年在研经费 1000 余万元。张国权教授获得天津市青年科技奖，楼慈波博士获得饶毓泰基础光学奖二等奖。

The research fund in 2007 amounts to more than 10 millions RMB. Professor Guoquan Zhang won the Tianjin youngster for science and technology award, Dr. Cibo Lou won the Rao-Yutai fundamental optics award (the second prize).

光谱表征及传感技术/Spectral Charaterization and Sensing Techniques

负责人：臧维平

本方向涉及激光器，上转换发光材料，光纤器件，稀土掺杂发光材料，应用光谱学和光谱仪器等方面。本年度发表论文 15 篇；申请发明专利 4 项，申请实用新型专利 2 项；在研课题经费 213 万元；结题项目 2 项。取得的代表性成果如下：

In this field, we mainly focused on the laser ,up conversion luminescent material ,fiber optic, rare earth dope glass , applied spectroscopy and spectral instrument . 15 papers were published in international academic journals, and six patents applicanted. The total reasearching founds are more than 2 millions. This year, we obtained some important results, they are mainly shown as following:

一、高增益铒玻璃的发光和激光特性

1、 上转换特性：测量铒镱共掺磷酸盐玻璃激光器在不同泵浦功率和输出功率下的上转换荧光光谱，计算共协上转化和能量转移效应对激光输出的影响，根据计算出的理论结果，对激光器的设计参数进行优化。

2、 热效应：测量和计算铒镱共掺磷酸盐玻璃激光器中的热透镜焦距、分数热沉积。研究热效应对激光光束品质因子M^2、模式匹配等参数的影响。

3、 腔内损耗：测量和计算铒镱共掺磷酸盐玻璃激光器的腔内损耗，并对不同谐振腔结构的腔内损耗进行分析。

Luminescent and laser character of high gain erbium glass , including character of up conversion , thermal loading in laser diode pumped erbium ytterbium codoped phosphate glass microchip laser , model of longitudinally laser diode pumped Erbium–Ytterbium-Codoped phosphate glass microchip laser with up conversion , and cavity loss in laser diode pumped erium : ytterbium-phosphate glass microchip lasers.

二、高增益光纤的发光和激光特性

1、 设计并制作了自动光纤拉制设备。在拉丝过程中对光纤直径进行动态测量及计算机自动调整电机转速，达到实时控制拉丝速度从而自动控制光纤直径。现已拉出直径在 100—130μm 的光纤,光纤有涂敷保护。

2、 国内首次利用长度为 12cm 的高增益 Er/Yb 共掺磷酸盐玻璃光纤实现了功率达 130mW 的激光连续运转。

3、 首次观测了 10 厘米量级的高增益 Er/Yb 共掺磷酸盐玻璃光纤在 976nm 半导体激光器抽运下的超荧光发光现象。

Luminescent and laser character of high gain fiber , we designed and fabricated equipment of auto pulling fiber , using computer auto adjust the rotational speed of motor , to control the diameter of fiber real time , now we can fabricate diameter 100-130 micrometer fiber with protection coating. We get 130mW continuous laser output using 12cm high gain Er/Yb glass fiber and observed the super fluorescence effect in 10cm 976nm diode laser pumped high gain Er/Yb

glass fiber.

三、稀土掺杂玻璃材料上转换发光特性

利用稀土掺杂上转换玻璃材料制备了红外激光检测卡，并申请了发明专利。

Up conversion character of rare earth doped glass , we using this kind material fabricated the card of view infrared laser and applied the patent.

四、应用光谱学和光谱仪器领域

应用光谱领域继续进行肿瘤组织表面增强拉曼光谱研究；光谱学仪器方面，设计了小型化拉曼光谱仪样机，其中的像散纠正平场光谱仪具备优异的成像功能，在 10㎜ 高度谱面上，使用 50 微米直径光纤，可以同时获得 8 路光谱信号。

Apply spectroscopy and spectral instrument , we continued research in the Raman character of cancer tissue. We designed the astigmatism correction flat spectral field spectrometer and get better performance.

半导体生长技术和半导体器件/ Semiconductor Growth and Devices

负责人：舒永春

2007 年度本方向主要在以下方面取得了进展:

This year, we obtained some important results, they are mainly shown as following:

1. 设计与加工液氮压力控制和气液分离系统，配置新的捕集系统，降低了 MBE 系统液氮消耗 20%～30%，解决了 MBE 的固体磷源安全使用与控制技术的难题，实现含磷材料连续可控生长。

   Liquid nitrogen system pressure control and detachment of gas and liquid system were designed and machined in 2007. By configurating new entrapping system, the liquid nitrogen consumption is decreased about 20%~30% in MBE system. By resolving the difficult problem of safely using and controlling solid phosphorus in MBE system, the phosphorated materials were grown safely controlled.

2. 开发了应力补偿技术；应力补偿技术有效的降低了应力和深能级缺陷对发光的影响，获得了高质量的 GaAsP 应力补偿的 InGaAs/GaAs 多层量子阱结构材料（见图 1）。对开发大功率器件具有重要意义。

   The stress compensation technique is researched, which decrease the influence of stress and deep level on the photoluminescence effectively, and obtained the high-grade InGaAs/As multiple layers quantum well materials with the GaAsP stress compensation (shown in Fig.1). It is significant to exploit superpower device.

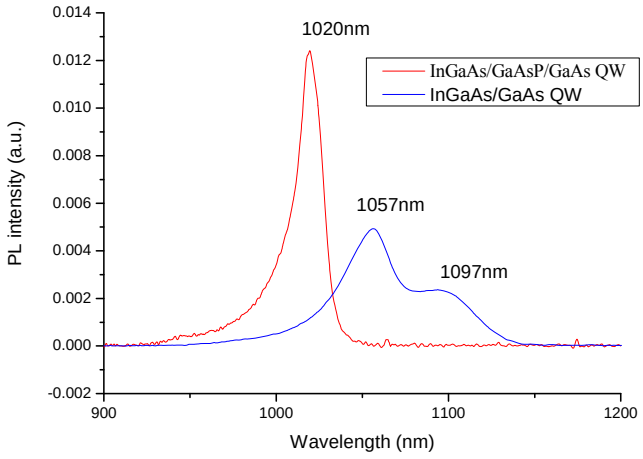

图 1 应变补偿和无应变补偿的比较

Fig.1 Compared of stress compensation and none stress compensation

3. 深入研究 GaAs 基和 InP 基生长三元化合物半导体材料，首次将应力和脱附因素引入热力学分析之中，建立了新的三元和四元含磷化合物半导体的热力学分析模型，并在实验中得到验证（见图 2 和图 3）。获得了高质量的 InGaP/GaAs 和 InGaAs/InP 晶格匹配材料，并实现可控生长，为含磷化合物半导体材料与器件的开发奠定基础。

   The ternary semiconductors based on GaAs and InP substrate were thoroughly researched.

By introducing the stress and desorption into the thermal analysis firstly, new thermal dynamical analytical model about ternary and quaternary phosphorated semiconductor was established and proved in the experiment (shown in Fig. 2 and Fig. 3). The high quality InGaP/GaAs and InGaAs/InP lattice matching materials were grown by controllable method, and the condition of developing the phosphorated semiconductor and devices is realized.

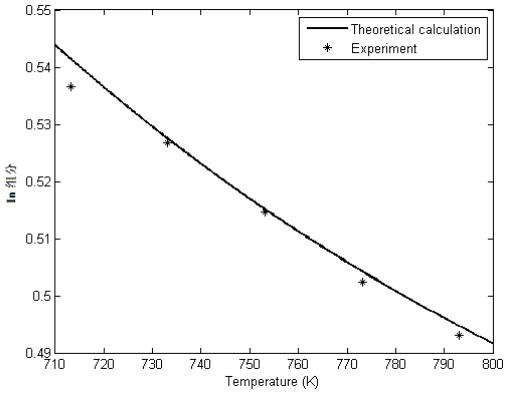

图 2 生长温度对 $In_xGa_{1-x}P/GaAs$ 的组分 x 的影响

Fig.2 The influence of growth temperature on x in $In_xGa_{1-x}P/GaAs$

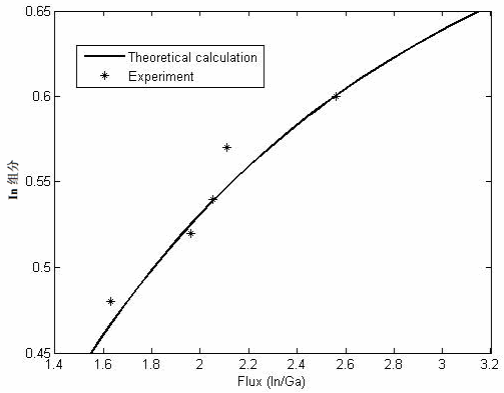

图 3 In/Ga 束流比对 $In_xGa_{1-x}As/InP$ 的组分 x 的影响

Fig.3 The influence of In/Ga flux ratio on x in $In_xGa_{1-x}As/InP$

4. 深入研究了 MBE 生长工艺参数对 AlAs/GaAs 的界面和反射谱的影响，获得了反射率达到 99.6%的高反射率的 BDR 材料。并获得了较为理想的 1064nm 半导体垂直外腔表面发射激光器芯片材料，进入光泵浦试验阶段（国家 863 项目 2006～2008）。

   The influence of growth parameters on AlAs/GaAs interface and reflectance spectrum was researched, and the DBR materials that high reflectance index could be 99.6% were obtained. The relative ideal VCSEL chip materials on 1064nm wavelength were grown successfully, and the National 863 project of China was researched into the optical pumping period.

5. 首次利用 F 共注入掺杂和毫秒闪光灯退火方法使 ITO/SiO_2:Gd/Si 硅基紫外电致发光器件的量子效率提高了四倍以上。通过采用 F 离子共掺降低了 SiO_2 薄膜中的空位缺陷在导带下的陷阱能级对国过热电子的散射。通过闪光灯快速退火抑制了稀土离子的团簇形成。目前器件的量子效率超过 5 %，达到同波段 GaAIN 基 LED 的水平。

   Efficient ultraviolet electroluminescence UVEL is obtained from metal-oxide-silicon MOS structures with the SiO_2 :Gd/F active layers prepared by flash lamp annealing and Gd and F coimplantation. We observed a doubling of both the UVEL intensity and the defect related luminescence by increasing the fluorine concentration. This is due to suppression of the hot electron scattering on the donor-type level of the E_1' center, the number of which is reduced by fluorine, and to increase of the optical active Gd^{3+} centers by Gd–F_3 molecule formation. Also, fluorine coimplantation has no influence on the operating time of the MOS diode. Additionally, the flash lamp annealing doubled the ultraviolet electroluminescence from SiO_2 layers implanted by gadolinium alone or in combination with fluorine. This is related to the suppression of cluster formation of rare earth atoms occurring during conventional annealing methods.

6. 制造出首次报道了 ITO/SiO_2:Eu/Si 结构的硅基的可变色硅基电致发光器件。通过改变电流的注入使稀土 Eu 离子从三价转变为二价，实现了发光颜色由红到蓝的变化。

   A Si metal-oxide-semiconductor electroluminescent device structure is reported which emits two colors, while being doped with a single rare-earth element. Thermally grown SiO_2 oxide layers were implanted with Eu and subseqently annealed. Depending on the electrical excitation current, the luminescence is red or blue, which can be ascribed to electronic transitions in tri- and divalent europium Eu^{3+} and Eu^{2+}, respectively.

发表论文/Publications in Journal

1. Cibo Lou, Xiaosheng Wang, Jingjun Xu, Zhigang Chen, Jianke Yang, "Nonlinear Spectrum Reshaping and Gap-Soliton-Train Trapping in Optically Induced Photonic Structures", *Phys. Rev. Lett.* 98, 213903 (2007). *
2. Xiaosheng Wang, Anna Bezryadina, K. G. Makris, D. N. Christodoulides, G. I. Stegeman and Zhigang Chen, "Observation of Two-Dimensional Surface Solitons", *Phys. Rev. Lett.* 98, 123903 (2007).
3. X. Wang, Zhigang Chen, J. Wang and J. Yang, "Observation of embedded lattice solitons", *Phys. Rev. Lett.* 99, 243901(2007).
4. A. Szameit, X. Wang, K. G. Makris, Y. V. Kartashov, T. Pertsch, S. Nolte, A. Tünnermann, A. Bezryadina, Z. Chen, D. N. Christodoulides, L. Torner, and G. I. Stegeman, "Two-dimensional surface lattice solitons", *Optics & Photonics News*, 18**,** 42 (2007) (December special issue, "Optics in 2007").
5. Xinyuan Qi, Simin Liu, Guoquan Zhang, Ru Guo, Zhaohong Liu, Lipeng Zhou, and Yuan Li, "Gap solitons in optically induced two-dimensional square photonic lattices in $LiNbO_3$:Fe crystals", *Appl. Phys. Lett.* 91, 131111 (2007).
6. S. Prucnal, J. M. Sun, W. Skorupa, and M. Helm, "Switchable two-color electroluminescence based on a Si metal-oxide-semiconductor structure doped with Eu", *Appl. Phys. Lett.* 90, 181121 (2007).
7. S. Prucnal, J. M. Sun, L. Rebohle, and W. Skorupa, "Fourfold increase of the ultraviolet (314nm) electroluminescence from SiO2:Gd layers by fluorine coimplantation and flash lamp annealing", *Appl. Phys. Lett.* 91, 181107 (2007).
8. Yong-Fa Kong, Shi-Guo Liu, Yan-Jun Zhao, Hong-De Liu, Shao-Lin Chen, Jing-Jun Xu, "Highly optical damage resistant crystal: Zirconium-oxide-doped lithium niobate", *Appl. Phys. Lett.* 91, 081908 (2007). *
9. Wen-Bo Yan, Hong-Jian Chen, Li-Hong Shi, Shi-Guo Liu, Yong-Fa Kong, "Investigations of the light-induced scattering varied with HfO_2 codoping in $LiNbO_3$:Fe crystals", *Appl. Phys. Lett.* 90, 211108 (2007).
10. Li Wu, Yi. Zhang, Yong-Fa Kong, Tong-Qing Sun, Jing-Jun Xu, Xiao-Long Chen, "Structure determination of novel orthoborate $NaMgBO_3$: A promising birefringent crystal", *Inorg. Chem.* 46, 5207-5211 (2007).
11. Zhang-Cheng Xu, Ya-Ting Zhang, Randall L. Headrick, Hua Zhou, Lan Zhou, Tomoe Fukamachi, "Self-organized growth of microsized Ge wires on Si (111) surfaces", *Phys. Rev. B* 75, 233310 (2007).
12. Zhang-Cheng Xu, Ya-Ting Zhang, J. M. Hvam, "Influence of in situ annealing on carrier dynamics in InGaAs/GaAs quantum dots", *Nanotechnology* 18, 325401 (2007).
13. S. Prucnal, J. M. Sun, H. Reuther, W. Skorupa, and Ch. Buchal, "Strong Improvement of the Electroluminescence Stability of SiO2:Gd Layers by Potassium Co-implantation", *Electrochem. Solid-State Lett.* 10, J30 (2007).
14. S. Prucnal, J. M. Sun, A. Muecklich, and W. Skorupa, "Flash Lamp Annealing vs Rapid Thermal and Furnace Annealing for Optimized Metal-Oxide-Silicon-Based Light-Emitting Diodes", *Electrochem. Solid-State Lett.* 10, H50 (2007).
15. Wen-Bo Yan, Yang-Xian Li, Li-Hong Shi, Hong-Jian Chen, Shi-Guo Liu, Ling Zhang, Zi-Heng Huang, Shao-Lin Chen, Kong-Fa Kong, "Photochromic effect in $LiNbO_3$:Fe:Co", *Opt. Exp.* 15(25), 17010-17018 (2007).

* 选录论文/Selected papers

16. Guoquan Zhang, Weiyue Che, Bin Han, and Yiling Qi, “Recursion formula for reflectance and the enhanced effect on the light group velocity control of the stratified and phase-shifted volume index gratings”, *Opt. Exp.* 15(5), 2055-2066 (2007). *

17. Zhi-Bo Liu, Xiao-Qing Yan, Jian-Guo Tian, Wen-Yuan Zhou, and Wei-Ping Zang, “Nonlinear ellipse rotation modified Z-scan measurements of third-order nonlinear susceptibility tensor”, *Opt. Exp.* 15, 13351-13359 (2007). *

18. Liqin Tang, Cibo Lou, Xiaosheng Wang, Daohong Song, Xingyu Chen, Jingjun Xu, Zhigang Chen, H. Susanto, K. Law, P. G. Kevrekidis, “Observation of dipole-like gap solitons in self-defocusing waveguide lattices”, Opt. Lett. 32, 3011 (2007). *

19. T. H. Zhang, X. K. Ren, B. H. Wang, C. B. Lou, Z. J. Hu, W. W. Shao, Y. H. Xu, H. Z. Kang, J. Yang, D. P. Yang, L. Feng, and J. J. Xu, “Surface waves with photorefractive nonlinearity”, *Phys. Rev.* A 76: 013827 (2007).

20. Jiwei Qi, Jingjun Xu, Yudong Li, Fanlei Kong and Qian Sun, “Magnetophotorefractive effect of holographic recording in $LiNbO_3$:Fe crystals”, *J. Appl. Phys.*, 101: 083116 (2007).

21. Jing Chen, Yudong Li, Wenqiang Lu, Jiwei Qi, Guoxin Cui, Hongbing Liu, Jingjun Xu, and Qian Sun, “Observation of surface-plasmon-polariton transmission through a silver film sputtered on a photorefractive substrate”, *J. Appl. Phys.* 102: 113109 (2007).

22. Liu S, Song F, Cai H, “Investigation of the roundtrip cavity loss in laser diode pumped erium : ytterbium-phosphate glass microchip lasers”, *J. Appl. Phys.* 102(10): 103101 (2007).

23. Li Wu, Y. Zhang, Xiao-Long Chen, Yong-Fa Kong, Tong-Qing Sun, Jing-Jun Xu, Y. P. Xu, “The Na2O-SrO-B2O3 diagram in the B-rich part and the crystal structure of NaSrB5O9”, *J. Solid State Chem.* 180, 1470-1475 (2007).

24. Song F, Han L, Zou C, “Upconversion blue emission dependence on the pump mechanism for Tm^{3+}-heavy-doped $NaY(WO_4)(2)$ crystal”, *Appl. Phys.* B-Lasers and Optics, 86(4), 653-660 (2007).

25. Xiao-Chun Li, Yong-Fa Kong, Yun-Cai Wang, Li-Zhong Wang, Fu-Cai Liu, Hong-De Liu, Ya-Nan An, Shao-Lin Chen, Jing-Jun Xu, “Nonvolatile holographic storage of near-stoichiometric $LiNbO_3$:Cu:Ce with green light”, *App. Opt.* 46, 7620-7624 (2007).

26. Meixiu Sun, Chunping Zhang, Zhaofeng Hao, Jianguo Tian, “Effect of surface roughness on determination of tissue optical properties obtained by diffusion approximation”, *Appl. Opt.* 46 (17), 3649-3652 (2007).

27. FengSong, Xin Zhang, Yanxiong Wu, Shujing Liu, “Simplified transformation circle theory in analyzing a laser resonator”, *Appl. Opt.* 46(13), 2492-2497 (2007).

28. Feng Song, Shujing Liu, “Determination of the thermal loading in laser diode pumped erbium ytterbium codoped phosphate glass microchip laser”, *J. Opt. Soc Am.* B, 24(9), 2327-2332 (2007).

29. Zhi-Bo Liu, Yong-Liang Liu, Bin Zhang, Wen-Yuan Zhou, Jian-Guo Tian, Wei-Ping Zang, Chun-Ping Zhang, “Nonlinear absorption and optical limiting properties of carbon disulfide in short-wavelength region” *J. Opt. Soc. Am.* B 24, 1101-1104 (2007).

30. Haijun Qiao, Jingjun Xu, Yasuo Tomita, Dengsong Zhu, Bo Fu, Guoquan Zhang, Guangyin Zhang, “UV-light-induced one-color and two-color photorefractive effects in congruent and near-stoichiometric $LiNbO_3$:Mg crystals”, *Opt. Mater.* 29, 889-895 (2007).

31. Shengwen Qi, Chunping Zhang, Xiuqin Yang, Kuan Chen, Lianshun Zhang, Guang Yang, Xing Liang, Tang Xu and Jianguo Tian, “Absorption characteristic and limiting effect of Congo red doped PVA film”, *Opt. Mat.* 29(11), 1348-1351 (2007).

32. Shao-Lin Chen, Hong-De Liu, Yong-Fa Kong, Zi-Heng Huang, Jing-Jun Xu, Guang-Yin Zhang, “The resistance against optical damage of near-stoichiometric $LiNbO_3$:Mg crystals

prepared by vapor transport equilibration", *Opt. Mat.* 29, 885-888 (2007).

33. Xiao-Chun Li, Yong-Fa Kong, Hong-De Liu, Lei Sun, Jing-Jun Xu, Shao-Lin Chen, Ling Zhang, Zi-Heng Huang, Shi-Guo Liu, Guang-Yin Zhang, "Origin of the generally defined absorption edge of non-stoichiometric lithium niobate crystals", *Solid State Commun.* 141, 113-116 (2007).

34. Shengwen Qi, Chunping Zhang, Xiuqin Yang, Kuan Chen, Lianshun Zhang, Yongliang Liu, Tang Xu and Jianguo Tian, "Effective indexes of refraction and limiting properties of ethyl red"，*Optik*-International Journal for Light and Electron Optics 118(9), 425-429 (2007).

35. W. Liu, Y. Sun, W. Li, C.-J. Li, F.-Y. Li, J.-G. Tian, "Influence of different precursor surface layerson Cu*(*In1−*x*Ga*x)*Se2 thin film solar cells", *Appl. Phys.* A 88(4), 653-656 (2007).

36. Dengsong Zhu, Jingjun Xu, Haijun Qiao, Wei Li, Yanli Shi, Feng Gao, Zhenhua Wang, Bo Fu, Guoquan Zhang, "Temperature dependence of photorefractive effect in reduced near stoichiometric $LiNbO_3$ crystals", *Opt. Commun.* 272, 391-394 (2007).

37. Chunfu Huang ,Ru Guo, Simin Liu, Zhahong Liu, "Interaction of incoherent white light solitons", *Opt. Commun.* 269, 174-178 (2007).

38. Shu-Qi Chen, Wei-Ping Zang, Zhi-Bo Liu, Wen-Yuan Zhou, Yong-Fa Kong, Jian-Guo Tian, "Method for measurements of second-order nonlinear optical coefficient based on Z-scan", *Opt. Commun.* 274, 213-217 (2007).

39. Zhaohong Liu, Simin Liu, Ru Guo, Tao Song, Nan Zhu, "Interaction between a dark spot and a two-dimensional nonlinear photonic lattice with fully incoherent white light", *Phys. Lett.* A 363, 243-249 (2007).

40. Yan Zhu, Yi-Zhou Zhu, Hai-Bing Song, Jian-Yu Zheng, Zhi-Bo Liu, Jian-Guo Tian, "Synthesis and Crystal Structure of 21,23-Dithiaporphyrins and Their Nonlinear Optical Activities", *Tetra Lett.* 48, 5687-5691 (2007).

41. Feng Song, Shujing Liu, "Model of Longitudinally Laser Diode Pumped Erbium–Ytterbium-Codoped Phosphate Glass Microchip Laser With Upconversion", IEEE J. Quantum Electronics 43(9), 817-823 (2007).

42. Biao Pi, Yongchun Shu, Yaowang Lin, Jiaming Sun, Shengchun Qu, Jianghong Yao, Xiaodong Xing, Bo Xu, Qiang Shu, Zhanguo Wang and Jingjun Xu, "Morphological and electrical properties of InP grown by solid source molecular beam epitaxy", *J. Crystal Growth*, 299 243–247(2007).

43. Lin Zhang, Xinyu Wang, Meixiu Sun, Ying Cai, Zhaofeng Hao, Chunping Zhang, "Monte Carlo Simulation for the light propagation in two-layered cylindrical biological tissues", *J. Mod. Opt.* 54(10), 3649-3652 (2007).

44. Zhang T. H., Yang, J., Kang H. Z., Feng L., Lou C.B., Ren X. K.; Yang D. P., Lu, Y. Z., Wang B. H., Hu Z. J., Xu Y. H., Shao, W. W., Zhang, C. P., Xu J. J., "Photorefractive surface waves at the interface of Sr0.6Ba0.4NbO3 and air with diffusion mechanism", *J. Mod. Opt.* 54(8): 1165-1171 (2007).

45. Zhang T. H., Ren X. K., Wang B. H., Hu Z. J., Shao, W. W., Yang, J., Kang H. Z., Yang D. P., Lu, Y. Z., Feng L., Wang W. J., Xu J. J., "Modes of photorefractive surface waves", *J. Mod. Opt.* 54(10): 1445–1452 (2007).

46. Bao-Rong Liu, Li-Juan Zhao, Jian Sun, Hua Yu, Jie Song, Jing-Jun Xu, "Broadband and high efficient 1530nm emission from oxyfluoride glass ceramics codoped with Er3+ and Yb3+ ions", *Chin. Phys. Lett.* 24(2), 527-529 (2007).

47. Hong-De Liu, Yong-Fa Kong, Qian Hu, Ri-Wen Wu, Wen-Jie Wang, Xiao-Chun Li, Shao-Lin Chen, Shi-Guo Liu, Jing-Jun Xu, "Light-induced domain inversion in Mg-doped near stoichiometric lithium niobate crystals", *Chin. Phys. Lett*. 24, 1720-1723 (2007).

48. Bi-Fen Gao, Ying Ma, Ya-An Cao, Zhan-Jun Gu, Guang-Jin Zhang, Jian-Nian Yao, “Preparation and photocatalytic properties of Ti1-xZrxO2 solid solution”, *Chin. J. Chem.* 25, 484-489 (2007).

49. Zhaohong Liu, Simin Liu, Ru Guo, Yuanmei Gao, Tao Song, Nan Zhu, Di Qu, “Interaction between two-dimensional white-light photovoltaic dark spatial solitons”, *Chin. Phys. Lett.*, 24(2), 446-449 (2007).

50. Xinyuan Qi， Simin Liu，Ru Guo, Yi Lu, Zhaohong Liu, Lipeng Zhou, Yuan Li, “Defect solitons in optically induced one-dimensional photonic lattices in LiNbO3:Fe crystal”, *Chin. Phys. Lett*,.24(2), 446－449 (2007).

51. Yuanmei Gao, Simin Liu, “White-light nonlinear photonic lattices in self-defocusing media”, *Chin. Phys. Lett.*, 24(6), 1596-1599 (2007).

52. Li-Hong Shi, Wen-Bo Yan, and Yong-Fa Kong, **“**OH^- absorption band in $LiTaO_3$ with varied composition and hydrogenation”, *Eur. Phys. J. Appl. Phys.* 40, 77-81 (2007).

53. 齐继伟，李玉栋，许京军，崔国新，孔凡磊，孙骞，“铌酸锂中的磁光折变效应研究”，物理学报 56（12），7015-7022（2007）。

54. 涂燕飞，张国权，陈聪，高峰，薄方，刘建彬，许京军，“固体介质中的电磁感应透明效应及其应用”，物理 36（5），391-396（2007）。

55. 黄春福，郭儒，刘思敏，“多个部分非相干光孤子的相互作用”，物理学报 56（2），908-915（2007）。

56. 张冰，刘智波，陈树琪，周文远，臧维平，田建国，罗代兵，朱志昂，“新型卟啉衍生物反饱和吸收研究”，物理学报 56（9），5252-5257（2007）。

57. 刘玮，孙云，李凤岩，何青，李长健，田建国，“利用 Raman 散射光谱研究铜铟镓硒薄膜表面的掺杂调节作用”，光谱学与光谱分析 27（4），716-719（2007）。

58. 杨光，蒲守智，杨天赦，杨秀芹，张春平，郝召锋，田建国，“二芳基乙烯化合物的光学性质和光限制效应”，南开大学学报（自然科学版）40（5），63-67（2007）。

59. 杨光，张春平，陈桂英，杨秀芹，田建国，“光学新事物滤波器及其应用”，激光与光电子学进展 44（11），24-29（2007）。

60. 郝召锋，孙美秀，王新宇，许棠，李晓霞，田建国，张春平，“会聚光在柱状模拟生物组织中的实验研究”，光子学报 36（7），1302-1306（2007）。

61. 皮彪，孙甲明，林耀望，姚江宏，邢晓东，蔡莹，舒强，贾国治，刘如彬，李丹，王占国，“Unstable Growth in InP Homoepitaxy: Mound Formation”，人工晶体学报 36（2），263~266（2007）。

62. Biao Pi, Yongchun Shu, Yaowang Lin, Bo Xu, Shengchun Qu, Zhanguo Wang, “Growth Modes of InP Epilayers Grown by Solid Source Molecular Beam Epitaxy”, 半导体学报，28 卷增刊 45～49（2007）。

63. 舒强，舒永春，刘如彬，陈琳，姚江宏，许京军，王占国，“半导体可饱和吸收镜实现超短高功率脉冲激光研究进展”，激光与红外 37（3），197~199（2007）。

64. 贾国治，姚江宏，刘国梁，柏天国，刘如彬，邢晓东，“俄歇复合对应变量子阱激光器阈值电流的影响”，量子电子学报 24（1），105~109（2007）。

65. 贾国治，姚江宏，舒永春，王占国，“近红外波段 InAs 量子点结构与光学特性”，发光学报 28（1），104~107（2007）。

66. 王栋栋，陈云琳，李兵，颜彩繁，许京军，张光寅，“利用光栅衍射效应探测周期极化

微结构晶体”，物理学报 56(12)，7153-7157（2007）。

67. 周斌斌，陈云琳，袁建伟，陈绍林，颜彩繁，许京军，张光寅，“准相位匹配光参量振荡器理论研究与优化设计”，红外与毫米波学报 26（4），293-296（2007）。

68. 陈云琳，袁建伟，周斌斌，颜采繁，许京军，张光寅，“掺镁铌酸锂微结构多周期调谐光学参量振荡器”，红外与激光工程 36（4），515-517（2007）。

69. 王淑香，陈云琳，颜彩繁，詹鹤，张光寅，“微片激光器的最新研究进展”，量子电子学报 24（4），401-406（2007）。

70. 徐章程，宁海波，张雅婷，何本桥，“宽吸收带 MEH-PPV/PbS 量子点复合材料的制备”，人工晶体学报 36(2)，260-262（2007）。

71. 何龙，赵迪，孙同庆，张康，陈绍林，孔勇发，宋峰，“Er^{3+}:$KLa(WO_4)_2$ 晶体的生长与光谱性质”，中国稀土学报 25（4），479-482（2007）。

72. 张康，苏静，韩琳，闫立华，张学智，宋峰，“Er:NYW 晶体绿光上转换饱和现象研究”，光电子激光，18（1）71-73（2007）。

73. 韩琳，宋峰，万从尚，邹昌光，闫立华，张康，田建国，“自受激拉曼晶体$Nd(^{3+})$:$SrMoO_4$ 的光谱性质研究”，物理学报，56（3），1751-1757（2007）。

74. 宋峰，“Er^{3+}/Yb^{3+}共掺磷酸盐玻璃的发光与 1.54μm 激光性能”，激光与光电子学进展，名家讲坛约稿，15-25（2007）。

75. 韩琳，宋峰，邹昌光，苏静，闫立华，田建国，张光寅，“Tm^{3+}离子掺杂的钨酸钇钠晶体中浓度猝灭效应的研究”，物理学报，56（7），4187-4193（2007）。

76. 何龙，赵迪，孙同庆，张康，陈绍林，孔勇发，宋峰，“Er^{3+}：Kla（WO_4）$_2$ 晶体的生长与光谱性质”，中国稀土学报，25（4），479-482（2007）。

77. 田彬，邹万芳，何真，刘淑静，宋峰，“脉冲 Nd: YAG 激光除漆实验”，清洗世界 23（10）1-5（2007）。

78. 宋峰，邹万芳，田彬，刘淑静，“一维热应力模型在激光除漆中的应用”，中国激光 34（11），1577-1581（2007）。

79. 于舸，张攀，谭恩忠，张存洲，“人体肿瘤组织的拉曼光谱相关系数成像”，光谱学与光谱分析，27（2）295-298（2007）。

80. 许家林，徐晓轩，周新勇，张攀，张存洲，“光诱导雄黄矿物同质异象变化的显微成像拉曼散射研究”，光谱学与光谱分析 27（3），577-580（2007）。

81. 刘燕楠，邹祖全，刘燕青，徐晓轩，俞钢，张存洲，“肺正常组织与癌变组织的表面增强拉曼光谱”，光谱学与光谱分析 27（10），2045-2048（2007）。

书籍出版情况/Publications of Book

1. Guoquan Zhang, Fang Bo, Jingjun Xu, “*Slow and fast lights in photorefractive materials*”, in **Photorefractive Materials and Their Applications--Springer Series in Optical Science**, Eds. P. Günter and J. -P. Huignard, (Springer, 2007).
2. Z. Chen, J. Yang, “Controlling light in reconfigurable photonic lattices”, Review Book Chapter, in **Nonlinear Optics and Applications**, H. Abdeldayem ed. (Research Signpost, 2007)

专利/Patents

申请专利/ Patents Applied

[1] 200710056669.2；红外激光检测卡及其制备方法；发明；赵丽娟，余华。

[2] 200710057516.X；一种制备三元素掺杂高活性二氧化钛催化剂的方法；发明；曹亚安，王恩君，赵路松，龙绘锦。

[3] 200710150784.6；一种光纤预制棒的新型制作方法；发明；宋峰，程振洲，邹昌光，于晓晨，张家祥，蒋雪萍，田建国

[4] 200710057724.X；点光源装置；发明；张春平，田建国，郭磊，叶青，傅汝廉。

[5] 200710057891.4；高活性氮锡离子共掺杂纳米二氧化钛光催化剂的制备方法；发明；曹亚安，王恩君，赵路松。

[6] 200710058008.3；LD 泵浦微片固体激光器腔内损耗的测量方法及使用该方法的装置；发明；宋峰，蔡虹，刘淑静，李腾，田建国

[7] 200710058844.1；铌酸锂 pn 结及其制备方法；发明；孔勇发，黄自恒，肖罗生，陈绍林，刘士国，张玲，许京军。

[8] 200710059504.0；高可见光活性氮铟共掺杂纳米二氧化钛光催化剂的制备方法；发明；曹亚安，王恩君。

[9] 20071006163.6；超声检测窄脉宽激光除污机及其除污物方法；发明；宋峰，田彬，邹万芳，何真，刘淑静，牛孔贞，田建国

[10] 200720096496.2；牛角形光导管装置；实用新型；张春平，田建国，郭磊，叶青，傅汝廉。

[11] 200720099795.1；窄脉宽激光自动除污机；实用新型；宋峰，田彬，邹万芳，何真，刘淑静，牛孔贞，田建国

[12] 200720096684.5；新型光纤涂敷系统；实用新型；宋峰，程振洲，邹昌光，苏瑞渊，于小晨，张家祥，蒋雪萍，田建国

授权专利/ Patents Approved

［1］ZL200410019454.X；熔体注入法生长近化学比铌酸锂晶体系统及其工艺；发明；孙军，孔勇发，张玲，许京军，阎文博，黄自恒，刘士国，陈绍林，李剑韬，李兵。

国际合作与交流/International Cooperation and Exchange

来访人员名单/Visitors List

序号	姓名	国家或地区	单位	职称或职位	来访时间	来访目的
1.	Jenny Zhang	美国	The University of Texas at el Paso	博士	2007. 4	学术交流
2.	蒋仕彬	美国	亚利桑那大学光学中心	南开大学兼职教授	2007. 8	学术访问
3.	Conelia Denz	德国	明斯特大学应用物理学院	教授 院长	2007.9.8-20	讲学
4.	Lifeng Chi	德国	明斯特大学纳米中心	教授	2007.9.8-20	讲学
5.	Rudolf Friedrich	德国	明斯特大学理论物理学院	教授	2007.9.10-18	讲学
6.	Tilmann Kuhn	德国	明斯特大学非线性科学中心	教授	2007.9.10-18	讲学
7.	Wulfhard Lange	德国	明斯特大学应用物理学院	教授	2007.9.8-20	讲学
8.	Berenike Meyer	德国	明斯特大学动物和基因系	教授	2007.9.8-20	讲学
9.	Helmut Zacharias,	德国	明斯特大学物理学院	教授	2007.9.9-19	讲学
10.	Björn Kemper	德国	明斯特大学生物物理系	博士	2007.9.8-20	讲学
11.	Jörg Imbrock	德国	明斯特大学应用物理学院	博士	2007.9.8-20	讲学
12.	张鹏	西安	西北工业大学	讲师	2007.9	交流合作
13.	Yasuo Tomita	日本	The University of Electro-Communications	教授	2007.9.20-9.29	合作研究 讲学

出访人员名单/Personnel exchange Researchers List

序号	姓名	国家或地区	单位	职称或职位	出访时间	出访目的
1.	徐章程	日本	早稻田大学	教授	2006.11-2007.1	合作研究
2.	楼慈波	美国	旧金山州立大学物理天文系	讲师	2006.10-2007.2	访问学习

3.	宋　峰	美国	University of California, Los Angeles University of Arizona	教授	2007.4	学术访问
4.	武　莉	德国	亚琛工业大学	讲师	2006.7-2007.8	洪堡研究学者
5.	陈云琳	美国	阿肯色大学	教授	2006.11-2007.11	合作研究
6.	宋　峰	香港	City University of Hong Kong, Polytechnic University of Hong Kong	教授	2007.12	学术访问, 交流合作
7.	乔海军	加拿大	加拿大维多利亚大学	副教授	2006.4–2008.3	合作研究
8.	吴　强	美国	麻省理工	讲师	2006.12-2008.4	合作研究

研究生交流情况/Personnel exchange Students List

序号	姓名	国家或地区	单位	博士生/硕士生	出访时间	出访目的
1.	刘建彬	美国	University of Maryland	博士生	2007.9	联合培养
2.	祁轶舲	英国	University of Oxford	博士生	2007.10	联合培养
3.	王　喆	德国	Clausthal 工业大学	博士生	2007.8-10	合作研究
4.	杨程亮	德国	Clausthal 工业大学	硕士生	2007.10-12	合作研究

引进人才名单/New Staff

序号	姓名	性别	出生年月	职称	研究方向
1	薄　方	男	1979.12	讲师	非线性光学
2	Romano A. Rupp	男	1952.1	教授	光折变非线性光学
3	刘宏德	男	1978.11	讲师	光学材料

国内、国际会议报告/Talks at Conferences

1. 楼慈波，唐莉勤，陈志刚，许京军，“光子晶格中新颖的空间孤子” 第七届全国光学前沿问题讨论会，桂林（2007.10.28-11.1）**(饶毓泰奖报告)**
2. Z. Chen, "Linear and Nonlinear Control of Light in Photonic Lattices", Workshop on Mesoscopic Optics and Its Applications, Tianjin, China, January 2007. (**invited talk**)
3. Z. Chen, X. Wang, "Nonlinear Optical Waves in Photonic Lattices", Workshop on Topics in Nonlinear Dynamics and Complexity, Puebla, Mexico, Feb 2007. (**invited talk**)
4. Z. Chen, “Linear and nonlinear guidance in two-dimensional optically induced bandgap structures”, International Seminar and Workshop on Nonlinear Physics in Periodic Structures and Metamaterials, Dresden, Germany, March 2007. (**invited talk**)
5. Z. Chen, “Linear and nonlinear localization of light in discrete optical structures", the Fifth IMACS Conference, Georgia, April, 2007. (**invited talk**)
6. 宋峰，“用脉冲 Nd:YAG 进行除漆实验研究”，第七届全国清洗行业技术进步与清洁产业发展论坛，成都（2007.7.31-2007.8.3）。（**邀请报告**）
7. 孙甲明，W.Skorupa，S. Prucnal，“Efficient electroluminescence devices from rare-earth implanted SiO_2 MOS structures”，第 11 届全国发光学学术会议，长春（2007.8.20-25）。（**邀请报告**）
8. 舒永春，“MBE 生长 InGaP/GaAs 热力学研究”，中国物理学会 2007 年秋季学术会议，南京（2007.9.18-20）。（**邀请报告**）
9. 张国权，付博，刘祥明，徐庆君，陈绍林，孔勇发，许京军，“掺镁、锌和铟铌酸锂晶体的双色非挥发全息记录和紫外光激活中心热激活能测量”，中国物理学会 2007 年秋季学术会议，南京（2007.9.18-20）。（**邀请报告**）
10. Guoquan Zhang, “Slow and fast light with moving and stationary gratings”, 2007 summer school on frontiers in optics: from nonlinear to extreme optics, sponsored by DAAD, Teda Applied Physics School, Nankai University, Tianjin, China (2007.9.10-21).(**invited talks)**
11. Z. Chen, X. Wang, and J. Yang, "Linear and Nonlinear localization of light in light-induced lattices", Annual Meeting of the Optical Society of America, San Jose, Sept. 2007. (**invited talk**)
12. 徐晓轩，“Study on the Degradation of PLEDs by In-Situ Micro-Raman Spectroscopy”，SPIE International Symposium Photonics Asia 2007，北京（2007.11.12-15）。（**邀请报告**）
13. Cibo Lou, Xiaosheng Wang, Daohong Song, Zhigang Chen, “ Optical induction of photonic lattices for localization of novel periodic waves”, The OSA Topical Conference on Nanophotonics, Hangzhou, China (2007.6.18-21).
14. Guoxin Cui, Yudong Li, Jing Chen, Hongbing Liu, Jingjun Xu, Qian Sun, “Fabrication of waveguide using ferroelectric-domain structure in electro-optical crystal slice” The3rd SPIE International Symposium on Advanced Optical Manufacturing and Testing Technology (2007.7.8-11).
15. Qing Ye, Yu Liu, Wen-yuan Zhou and Jian-guo Tian, “Design and implementation of lens for fast biochip detection system”, Proc. of SPIE Vol. 6722, 672247, 成都 (2007.7.8-12).
16. 陈桂英，张春平，尚晓东，杨光，郝召锋，许旭旭，“基于细菌视紫红质中光感生各向异性的全光连续可调图象开关”，第十八届全国激光学术会议，哈尔滨 (2007.8.14-17).

17. 张雅婷，徐章程，“MEH-PPV 溶液及薄膜的研究时间分辨荧光光谱”，第 11 届全国发光学术会议，长春（2007.8.20-25）。

18. 徐章程，张雅婷，J. M. Hvam，“亚单层 InGaAs/GaAs 量子点异质结激光器”，第 11 届全国发光学术会议，长春（2007.8.20-25）。

19. Yating Zhang, Zhangcheng Xu, Haibo Ning, Xijie Chen, “Low-Temperature-Synthesized MEH-PPV/PbS Quantum Dot Composite”, The 2nd Korean-Chinese Student Workshop, Tianjin, China, Aug 27-29(2007).

20. 齐新元，刘思敏，郭儒，陆猗，刘照红，周立鹏，李源，“二维四方光折变光感应光子晶格中的带隙孤子”，中国物理学会 2007 年秋季学术会议，南京 (2007.9.18-20).

21. Yongfa Kong, Shiguo Liu, Shuqi Li, Shaolin Chen, Jingjun Xu, “The photorefractive properties of HfO_2 doped $LiNbO_3$ crystals, Controlling Light with Light: Photorefractive Effects, Photosensitivity, Fiber Gratings”, Photonic Materials and More (PR) Topical Meeting, California, USA, October 14-16 (2007).

22. 舒永春，皮彪，姚江宏，邢晓东，刘如彬，李丹，王占国，“InGaP/GaAs 生长热力学的研究”，第七届全国分子束外延学术会议，南昌（2007.10.20-24）。

23. 姚江宏，贾国治，舒永春，邢晓东，皮彪，王占国，“InAs/GaAs 量子点形貌与光学性质研究”，第七届全国分子束外延学术会议，南昌（2007.10.20-24）。

24. Meixiu Sun, Chunping Zhang, Jianguo Tian, Shengwen Qi, Yeqing Su, “Effect of surface roughness on determination of tissue optical properties”, The 6th International Conference on Photonics and Imaging in Biology and Medicine, 武汉 (2007.11.4-6).

25. Hongbing Liu, Yudong Li, Guoxin Cui, Yanfeng Zhang, Jing Chen, Jingjun Xu, Qian Sun，“Mach-Zehnder optical interferometric polarimeter using two reference beams with different heterodyne frequency”，Photonics Asia 2007，Beijing (2007.11.11-15).

26. Yanfeng Zhang, Yudong Li , Guoxin Cui, Hongbing Liu, Jing Chen, Jingjun Xu, Qian Sun, “Transverse optical trapping of spherical particle with strong absorption in a focused Gaussian beam”，Photonics Asia 2007, Beijing (2007.11.11-15).

主办国内、国际会议/Conferences Sponsored by the Laboratory

1. 介观光学及其应用研讨会（2007.1.3-1.4；天津）

在中国高等科技中心的资助下，介观光学及其应用研讨会于 2007 年 1 月 3 日—4 日在天津滨海新区泰达学院召开。研讨会顾问委员为甘子钊院士，由南开大学许京军教授和北京大学龚旗煌教授组织会议。

本次研讨会邀请了国内和部分国外从事介观光学及其应用方面研究的专家学者。国内参会专家分别来自北京大学、清华大学、南开大学、中国科学技术大学、上海交通大学、浙江大学、中山大学、哈尔滨工业大学、华东师范大学、华南师范大学、山西大学和中国科学院物理研究所等单位。会议还邀请了德国 Technische Universität Clausthal 的 Detlef Kip 教授和美国旧金山州立大学陈志刚教授。会议一共组织了 21 个报告，内容涉及介观体系材料的制备、性能表征以及器件应用等各个方面，共有 120 余人参加并聆听了报告。

研讨会组委会首先介绍了会议的基本情况，许京军教授代表南开大学致欢迎词，甘子钊院士就光学的发展历程、趋势以及介观光学研究的必要性和重要性作了重要的讲话。会议主要就以下两个方面展开了讨论和交流：（1）介观光学效应及其基本物理问题；（2）微/纳光子学材料、器件及其应用。

本次研讨会有近百名来自全国各大院校和研究所的研究生及高年级本科生聆听了报告，这使得本次研讨会不仅仅成为一个学术交流平台，同时也为拓宽研究生视野，提高研究生科学素质提供了一次难得的机会。会议取得了圆满的成功，与会者一致认为本次研讨会是介观光学领域的一次盛会，必将对今后一段时期内国内介观光学领域的研究产生重要的影响。与会者一致认为应该在国内形成有关介观光学及其应用方面的系列专题会议，以提供学术交流的平台，适应该领域迅猛发展的趋势，促进我国在介观光学及其应用这一新兴交叉学科的发展，为我国在该领域取得原创性进展作出贡献。本次会议得到了南开大学和南开大学泰达学院的部分资助和大力支持。

2. 纳米生物科学中韩联合研讨会（2007.8.27-8.29；天津）

2007 年 8 月 27 日至 8 月 29 日在天津经济技术开发区南开大学泰达应用物理学院召开了纳米生物科学中韩联合研讨会。会议组委会主席由南开大学泰达应用物理学院院长 Romano Rupp 教授和韩国釜山大学 Se-Young Jeong 教授共同担任。

本次研讨会除了主办、承办单位外还受到国家纳米技术产业化基地、南开大学生命科学学院以及天津医科大学等有关单位的广泛关注和高度重视，与会成员 60 余人，其中中方代表 40 余人，韩方代表 20 人。共收集论文摘要 50 余篇，23 个会议口头报告，38 个张贴报告，会上设置并产生了中韩双方的最佳口头报告奖和最佳张贴报告奖。

此次学术交流活动受到与会人员的一致好评，大家通过对纳米生物科学最新研究成果的交流学习和对纳米生物科学未来发展方向的探讨，开阔了视野，大家普遍认为会议报告内容丰富，涉及面广，会议学术气氛浓厚，举办成功。此次会议对于吸收并借鉴广大纳米生物医学科技工作者的最新思想和先进科研成果、建立中韩双边友好合作关系、并为我们在南开大学建立起纳米生物医学研究强势学科起到了一定的促进作用。

韩国釜山大学/ BK 21 Nano Fusion Technology Team，Pusan National University，Korea

南开大学弱光非线性光子学教育部重点实验室/ The Key laboratory of Weak Light Nonlinear Photonics (Nankai University, Tianjin 300457), Ministry of Education, China

3. 中德暑期学校（2007.9.9-20；天津）

2007 年 9 月 9 日至 20 日，“中德暑期学校：光学前沿—从非线性光学到极限光学”学术交流活动在南开大学泰达学院举行。

在为期两周的学期内，暑期学校一共邀请到了来自德国明斯特大学的 9 名教授和来自南开大学 11 名教授，他们为来自国内外 15 个高校和科研院所的 52 名学员进行为期两周的全英文授课讲座。授课和讲座的内容涉及激光光学、非线性光学的基本效应和应用、纳米光子学、极限光学和生物光子学等多个主题。参加暑期学校的学员也以张贴报告的形式介绍了自己的工作。同时，为增进暑期学校师生对南开大学、泰达学院以及天津开发区的了解，加强暑期学校师生之间的交流，暑期学校还组织他们参观了南开大学校园、泰达学院实验室、开发区企业等。

本次暑期学校的成功举行对加强与国内外同行之间的交流起到了非常积极的作用。更重要的是本次暑期学校的成功举行，为探索研究生暑期学校办学模式也进行了有益的尝试。据我们所知，本次暑期学校是国内第一次充分利用国外资源（国外资金，DAAD 资助；国外教授，德国明斯特大学 9 名教授）全英文授课讲座的暑期学校。暑期学校综合授课教师的报告和学员的文章摘要出版了论文摘要集一本《Frontiers in Optics: from nonlinear to extreme optics》。本次学术交流活动，主要由德意志学术交流中心（DAAD）资助，同时还得到了南开大学科技处、南开大学国际交流处、泰达学院等部门和单位的大力资助和支持。

德意志学术交流中心/ Sponsored by German Academic Exchange Service, DAAD

南开大学弱光非线性光子学教育部重点实验室/ The Key laboratory of Weak Light Nonlinear Photonics (Nankai University, Tianjin 300457), Ministry of Education, China

学术组织与期刊任职/Academic Service

国内学术组织任职/Service to the Domestic Professional Societies

序号	姓名	任职机构	职位	任期
1	许京军	天津市物理学会	理事长	
2	宋峰	国家自然科学资金委信息科学学部四处	流动项目主任	2006.5~2007.2
3	宋峰	国家教育部	教育部高等学校物理学与天文学教学指导委员会物理基础课程教学指导分委员会委员	2006-2010
4	孔勇发	天津市硅酸盐学会	晶体生长与材料专业委员会副主任	2005-
5	孙骞	天津市光电子学会	常委	2006-
6	宋峰	中国仪器仪表学会光机电技术与系统集成分会	第一届常务理事	2006-2010
7	孙骞	中国光学学会光电技术委员会	委员	2006-
8	徐章程	中国电子学会半导体集成分会	委员	2007-
9	宋峰	教育部高等学校物理基础课程教学指导分委员会	委员，高等学校文科类物理课程教学研究协作组成员	2006-2010
10	宋峰	大学物理课程报告论坛组委会	论坛之友，大学物理课程报告论坛专家	2007

国内期刊任职/Service to the Domestic Journals

序号	姓名	任职机构	职位	任期
1	许京军	Frontiers of Physics in China-Selected publications from Chinese Universities	编委	2005-
2	许京军	《光学学报》	副主编	
3	许京军	《红外与毫米波学报》	编委	
4	许京军	《物理》	编委	
5	孔勇发	《激光技术》编委会	编委	2006-2010
6	张国权	《激光技术》	编委	2007-2011
7	孙骞	《激光技术》	编委	2006-2010

获奖情况/Awards & Honors

离散系非线性光动力学研究
第六届饶毓泰基础光学奖二等奖
获奖者：楼慈波

获奖个人/Award for distinguished scientists

天津市青年科技奖
获得者：张国权

2007 年宝钢教育奖（宝钢优秀教师奖）
获得者：许京军

第九届“挑战杯”天津市大学生课外学术科技作品竞赛优秀指导教师
获得者：宋　峰　张天浩

南开大学首届“良师益友”
获得者：宋　峰　张天浩

获奖学生/Award for excellent students

掺铒钨酸钇钠晶体的多光子上转换发光研究
第十届“挑战杯”全国大学生课外学术科技作品　国家二等奖（2007.11）
获得者：张　康

铒铥共掺钨酸钇钠晶体的三光子间接敏化绿色上转换荧光
第九届“挑战杯”天津市大学生课外学术科技作品竞赛　市级特等奖（2007.9）
获得者：张　康

微小直径纤维测控及拉制设备
第九届“挑战杯”天津市大学生课外学术科技作品竞赛　市级一等奖（2007.9）
获得者：苏瑞渊　邹昌光　程振洲

泰达奖教金优秀学生奖一等奖：齐继伟

南开大学优秀学生干部：　　王慎之

南开大学优秀学生干部：　　肖罗生　张兰兰

南开大学奖学金：
二等奖学金　　张雅婷
三等奖学金　　王慎之　孙　军　胡　茜　薄　方

学位论文/Dissertations

1. 博士学位论文 Dissertation for Doctoral Degree

[1] 薄　方，位相耦合色散效应及光速控制研究，导师：许京军，张国权

[2] 付　博，掺杂铌酸锂晶体的紫外光子学非线性及其应用，导师：张国权

[3] 王振华，新式光学瞬态测量技术及其应用研究；导师：许京军

[4] 崔国新，铌酸锂晶体铁电畴结构应用的研究；导师：许京军，孙骞

[5] 齐继伟，磁场作用下的光折变弱光非线性效应的研究；导师：许京军，孙骞

[6] 唐莉勤，光诱导光子晶格中空间带隙孤子的研究；导师：陈志刚

[7] 刘　玮，溅射后硒化法生长 $Cu(In,Ga)Se_2$ 薄膜材料反应机理研究；导师：田建国

[8] 杨　光，有机光色材料的光学性质及其在光子学的应用；导师：张春平

[9] 舒　强，调制掺杂 GaAs/AlGaAs 2DEG 和 InAs 量子点材料的制备及特性研究；导师：王占国

[10] 贾国治，低维半导体结构的优化设计、可控性制备及机理研究；导师：王占国

[11] 皮　彪，含磷Ⅲ-Ⅴ族化合物半导体材料 MBE 生长与特性研究；导师：王占国

[12] 刘宏德，近化学计量比铌酸锂晶体光折变和畴反转研究；导师：孔勇发

[13] 李晓春，近化学计量比铌酸锂晶体光折变性能的研究；导师：孔勇发

2. 硕士学位论文 Dissertation for Master Degree

[1] 韩　彬，二维光子晶格中的若干光传播现象的研究；导师：张国权

[2] 石艳丽，紫外光敏有机玻璃的制备及基本光学性能的研究；导师：张心正

[3] 王　恒，便携式傅立叶变换光谱技术的研究；导师：田建国

[4] 荣　华，飞秒激光与玻璃相互作用及“光丝”的研究；导师：田建国

[5] 冯　蕾，针状畴 SBN:Nd 准相位匹配二次谐波以及掺铁铌酸锂表面光波导；导师：张天浩

[6] 胡志健，光折变非线性表面光波导；导师：张天浩

[7] 贾　峰，新型光纤信号调制器；导师：张天浩

[8] 郭　磊，激光通过特殊光导管的传输特性研究；导师：张春平

[9] 陈　琳，多层耦合 InAs 量子点的生长及特性研究；导师：舒永春

[10] 王　影，基于光折变效应的 $Al_xGa_{1-x}As/GaAs$ 多量子阱；导师：姚江宏

[11] 柏天国，无铝大功率量子阱激光器结构设计及材料的 SSMBE 生长；导师：邢晓东

[12] 肖罗生，铌酸锂晶体异质结构的制备与性能研究；导师：孔勇发

[13] 吴日雯，光感应铌酸锂晶体畴反转的研究；导师：孔勇发

[14] 张兰兰，新型纳米二氧化钛材料制备及光催化性能研究；导师：曹亚安

[15] 赵路松，Sn、N 离子双相掺杂二氧化钛的光催化活性研究；导师：曹亚安

[16] 王栋栋，准相位匹配周期极化铌酸锂晶体微结构的研究；导师：陈云琳

[17] 王淑香，LD 泵浦紧凑型全固态固体激光器的研究；导师：陈云琳

[18] 宁海波，MHE-PPV/PbS 量子点红外复合材料的制备与表征；导师：徐章程

[19] 王艳丽，镶嵌在氧化铝纳米孔阵列中金属材料的光学性质；导师：徐章程

[20] 王　超，量子点激光器增益与线宽增强因子；导师：王占国，徐章程

[21] 赵艳军，掺锆铌酸锂晶体的生长及其抗光折变性能研究；导师：刘士国

[22] 谈绍峰，高直流电导钽/铌酸锂晶片的制备技术研究；导师：张玲

开放课题/Open Subject

2007 年 11 月 3 日，弱光非线性光子学教育部重点实验室召开了学术委员会扩大会议，学术委员会主任王占国院士主持了会议。会议根据学术委员会委员函审结果审批了开放基金，从申请的 12 项课题中评定出 5 项课题予以开放基金资助（资助名单如下）。

项目编号	项目名称	负责人	职称	工作单位	起止时间
OS 07-1	基于 PPMgLN 微结构波导的二次谐波发生器研究	樊亚仙	副教授	南京大学物理系	2007.11 -2009.9
OS 07-2	有机光致变色薄膜中光群速度传播特性及应用研究	陈桂英	研究员	中国科学院南海海洋研究所	2007.11 -2009.9
OS 07-3	非传统偏置电场对光诱导光子晶格中光波传输行为的调控	张　鹏	讲师	西北工业大学理学院	2007.11 -2009.9
OS 07-4	飞秒激光与生物组织的相互作用研究	祁胜文	教授	德州学院光电信息与技术研究所	2007.11 -2009.9
OS 07-5	掺铪系列铌酸锂晶片的紫外光折变研究	阎文博	助理研究员	河北工业大学材料学院	2007.11 -2009.9

Nonlinear Spectrum Reshaping and Gap-Soliton-Train Trapping in Optically Induced Photonic Structures

Cibo Lou,[1,2] Xiaosheng Wang,[2] Jingjun Xu,[1] and Zhigang Chen[1,2]

[1]*The Key Laboratory of Weak-Light Nonlinear Photonics, Ministry of Education and TEDA Applied Physical School, Nankai University, Tianjin 300457, China*

[2]*Department of Physics and Astronomy, San Francisco State University, San Francisco, California 94132, USA*

Jianke Yang

Department of Mathematics and Statistics, University of Vermont, Burlington, Vermont 05401, USA and Zhou Pei-Yuan Center for Applied Mathematics, Tsinghua University, Beijing 100084, China

(Received 16 February 2007; published 25 May 2007)

We report the first theoretical prediction and experimental demonstration of gap soliton trains in a self-defocusing photonic lattice. Without *a priori* spectral or phase engineering, a stripe beam whose spatial power spectrum lies only in one transverse direction evolves into a gap soliton train with power spectrum growing also in the orthogonal direction due to nonlinear transport and spectrum reshaping. Our results suggest that, in nonlinear k-space evolution, energy can transfer not only between regions of normal and anomalous diffraction, but also from initially excited regions to initially unexcited regions.

DOI: 10.1103/PhysRevLett.98.213903 PACS numbers: 42.65.Tg

The formation of gap solitons is a fundamental phenomenon of wave propagation in nonlinear periodic media. It has been studied in various branches of science including biology [1], condensed matter physics [2], Bose-Einstein condensates [3], as well as nonlinear optics [4,5]. In optics, gap solitons are traditionally considered as a *temporal* phenomenon in one-dimensional (1D) periodic media such as an optical fiber with periodic refractive-index variations [4]. Recently, however, *spatial* gap solitons have been predicted and demonstrated in a number of experiments [5–7]. These gap solitons have their propagation constants located inside the first photonic band gap (between the first and the second optical Bloch bands) of the periodic structure, in contrast to discrete solitons in the semi-infinite gap [8]. Typically, these gap solitons were observed with *off-axis* excitations in which the probe beam was launched at an angle to match the edge of the first Brillouin zone (BZ). Such excitations led to the observation of spatial gap solitons in *self-defocusing* "backbone" lattices (bifurcating from the bottom of the first band at the BZ edge where diffraction is anomalous) [6] or in *self-focusing* lattices (bifurcating from the top of the second band at the BZ edge where diffraction is normal) [7]. While a host of novel phenomena have been demonstrated with a 2D photonic lattice (such as BZ spectroscopy, Bloch oscillations and Zenner-tunneling [9], and band gap guidance by defects [10], to name just a few), a simple *on-axis* excitation of a 2D fundamental gap soliton without *a priori* spectral or phase engineering [11] has not been realized. More importantly, gap soliton trains have never been demonstrated in any nonlinear system to our knowledge, and they could be considered as nonlinearity-induced line defects in photonic band gap structures [12].

In this Letter, we report the first prediction and experimental demonstration of spatial gap soliton trains by a single-beam excitation in a self-defocusing photonic lattice. While a narrow circular beam can evolve into a 2D gap soliton as long as its k-space spectrum covers the entire first BZ (or the four high-symmetry M points of the first Bloch band), self-trapping of a narrow stripe beam into a gap soliton is nontrivial. Surprisingly, we find that a stripe beam (whose Bloch momentum lies initially only in one transverse direction and spectrum covers only two opposite M points) can evolve into the gap soliton train whose k-space momentum grows also in the orthogonal transverse direction after nonlinear spectrum reshaping. This suggests that a gap soliton can arise from Bloch modes even if these modes are not initially excited or only weakly excited. We monitor the nontrivial staggered phase structure of the gap solitons, and find that nonlinear transport under a self-focusing and defocusing nonlinearity shows dramatically different behavior of spectrum reshaping.

Different from our earlier experiments with lattice solitons [13], here we employ a *self-defocusing* nonlinearity to induce a backbone waveguide lattice [6]. The lattice is established by sending a partially coherent light beam through an amplitude mask. Under appropriate negative bias conditions, the periodically modulated input intensity pattern [Fig. 1(a)] induces the lattice, which remains nearly invariant through a 10-mm long photorefractive crystal (SBN:61). The lattice beam is ordinarily-polarized, but the induced index variation (controlled by the lattice beam intensity, coherence, and the bias field) is adjusted to be high enough for opening the first gap [14]. A coherent Gaussian-like probe beam, splitting from the same laser but extraordinarily-polarized, is sent into the crystal and

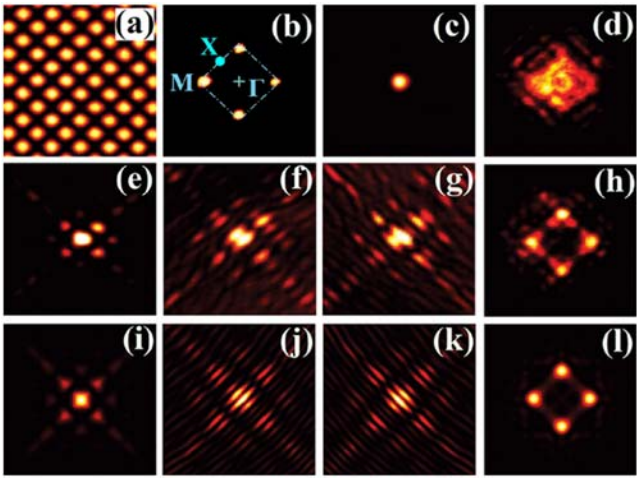

FIG. 1 (color online). Formation of a 2D gap soliton by single-beam on-axis excitation. Experimental results (a)–(h) show lattice pattern (a) and its spectrum with the first BZ and high-symmetry points marked (b), probe beam at input (c) and its linear output spectrum (d) through the lattice, output pattern of the gap soliton (e), its interferograms with a plane wave tilted from two different directions (f),(g) and its nonlinear output spectrum (h). Numerical results (i)–(l) show the gap soliton formation corresponding to (e)–(h).

propagates collinearly with the lattice beam. Linear and nonlinear transport of the probe beam is monitored simply by taking its instantaneous (before nonlinear self-action) and steady-state (after self-action) output patterns from the lattice. The spatial spectrum is obtained by using a lens to do Fourier transform and the far-field spectrum is recorded by a CCD camera positioned in its focal plane.

First, we summarize our results of *on-axis* excitation of a single 2D gap soliton in Fig. 1. Different from previous experimental observations in which either the probe beam was launched *off-axis* to match the edge of the first BZ [6] or its input phase or spectrum was engineered [11], we demonstrate on-axis excitation of a 2D gap soliton without *a priori* phase or spectral engineering. In fact, we show that nonlinear trapping of the probe beam leads to spectrum reshaping even though its initial spectrum is nearly uniform in the entire first BZ. The probe beam is focused into a 2D circular beam and launched into one of intensity minima (index maxima) of the backbone lattice (with about 23 μm spacing). The top panels of Fig. 1 show the input lattice beam, its Fourier spectrum, the input probe beam and its spectrum at output after linear propagation through the lattice, respectively. Under *linear* propagation, the probe beam experiences discrete diffraction, and its spectrum covers the first BZ with most of the power concentrating in the center. The middle panels show the formation of a 2D gap soliton under *nonlinear* propagation at a bias field of -1.3 kV/cm. The interferograms [Fig. 1(f) and 1(g)] show clearly that the gap soliton has a staggered phase structure (i.e., the central peak is out of phase with neighboring peaks), while its power spectrum [Fig. 1(h)] reshapes to have most of its power located in the four corners of the first BZ where diffraction is anomalous. These experimental results are corroborated with our numerical simulations using parameters close to those from experiment, as shown in the bottom panel of Fig. 1.

If the results of Fig. 1 are somewhat expected (although never reported before), our demonstration below on the formation of gap soliton trains is quite intriguing. Let us first illustrate theoretically the existence of such "staggered" gap soliton trains. Our theoretical model is a $(2+1)D$ NLS equation with a saturable self-defocusing nonlinearity and a periodic lattice potential [6,14,15]:

$$iU_z + U_{xx} + U_{yy} - \frac{E_0}{1 + I_L(x,y) + |U|^2} U = 0,$$

where U is the envelope function of the electric field, z is the distance of propagation, (x, y) are the transverse plane, E_0 is the applied dc field, and $I_L(x,y) = I_0 \cos^2[(x+y)/\sqrt{2}] \cos^2[(x-y)/\sqrt{2}]$ is the lattice intensity pattern (with peak intensity I_0). All variables have been normalized [15]. For $I_0 = 10$, and $E_0 = -10$ (corresponding to -2.0 kV/cm), the band gap structure is shown in Fig. 2(a). Using the numerical method developed recently [16], we find a family of spatial gap soliton trains inside the first photonic gap, bifurcating from the right edge of the first band (corresponding to the lattice M-symmetry point). The power curve of these soliton trains is also plotted in Fig. 2(a), where the power is defined over one period along the train direction. At a point near the band edge, the gap soliton train is shown in Fig. 2(b). It exhibits several vertical stripes periodically modulated, and in the central high-intensity region the stripes form a checkerboard pattern as adjacent stripes are out of phase with each other while in phase along the stripe. This gap soliton train can be considered as a bound state of a sequence of single 2D gap solitons (as shown in the middle left panel of Fig. 1). The soliton k-space spectrum is displayed in Fig. 2(c), where the four spots correspond to the four M-symmetry points at the edge of the first BZ.

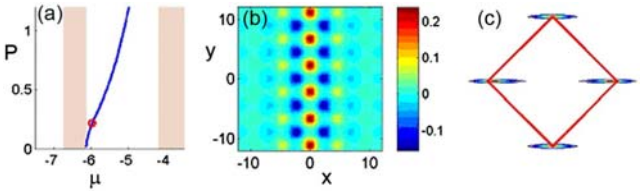

FIG. 2 (color online). Theoretical results showing formation of a gap soliton train. (a) the band gap structure (bands are shaded) and the soliton power curve; (b) a gap soliton train found at the red circle marked in (a), where the color bar shows the amplitude of the field; (c) the power spectrum of the gap soliton train in (b), and the red square marks the first BZ.

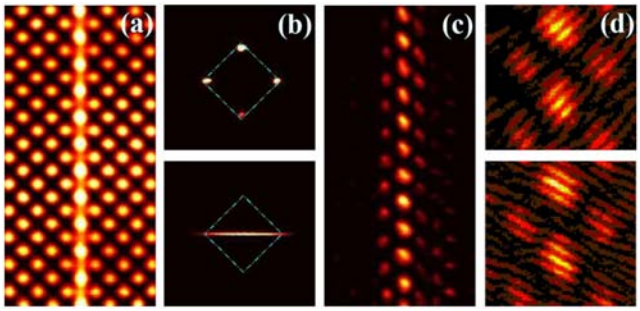

FIG. 3 (color online). Experiment results showing formation of a gap soliton train. (a) Superimposed pattern of a vertically oriented stripe beam and the lattice beam at input; (b) input spectrum of the lattice (top) and probe (bottom) beam with the first BZ marked by dotted line; (c) output pattern of the gap soliton train and its interferograms with a plane wave tilted from two different directions (d).

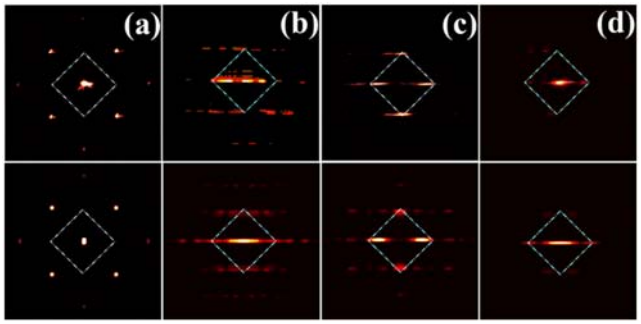

FIG. 4 (color online). Experimental (top) and numerical (bottom) results showing nonlinear spectrum reshaping. (a),(b) show the spectra of a 2D broad circular beam (a) and a 1D narrow stripe beam (b) under *linear* propagation (before self-action takes place) through the lattice. (c),(d) show the spectra of the stripe beam under *nonlinear* propagation (after self-action takes place) with self-defocusing (c) and self-focusing (d) nonlinearity.

Next, we show our experimental demonstration of a gap soliton train excited by a uniform stripe beam. The superimposed intensity pattern of the lattice and stripe beam at input is shown in Fig. 3(a). The vertically oriented stripe beam propagates collinearly with the lattice. Their power spectra are shown in Fig. 3(b), where the spectrum of the stripe beam forms nearly a horizontal line extended to two diagonal M points of the square lattice. Under nonlinear propagation at a bias field of -1.6 kV/cm, the stripe beam evolves into a gap soliton train [Fig. 3(c)], similar to that found in theory [Fig. 2(b)]. The staggered phase structure of the soliton beam is confirmed by its interferograms with a tilted plane wave [Fig. 3(d)], where the breaking and interleaving of interference fringes suggests the out-of-phase relation between the central stripe and two lateral stripes. Separate interferogram measurement shows the in-phase relation between peaks along the stripes in vertical direction.

The above observation poses a question. Different from a circular beam [Fig. 1(c) and 1(d)], a stripe beam has its initial k-space spectrum covering only a small portion of the first BZ, with no spatial frequency in regions near the two vertical M points [Fig. 3(b), bottom]. How does such a beam evolve into a gap soliton train? To answer the above question and better understand the linear and nonlinear transport of the stripe beam through the 2D lattice, we perform a series of experiments and numerical simulations under different conditions. We find that the power spectrum of the stripe beam becomes remarkably different from its initial spectrum after nonlinear propagation: not only does it break up in the horizontal direction into two spots near the two horizontal M points, but significant amount of power grows also near the other two vertical M points [Fig. 4(c)]. This indicates that the power spectrum of the probe beam has been drastically reshaped by nonlinear trapping into that of the exact gap soliton train found in Fig. 2(c).

Examining the spectra from linear and nonlinear propagation of a quasi-2D plane wave (a broad circular beam) and a quasi-1D plane wave (a narrow stripe beam) through the 2D lattice (Fig. 4, top panels), the picture of nonlinear spectrum reshaping becomes clear. According to the theory of Bloch-wave excitation in periodic structures [17], on-axis propagation of a 2D plane wave (with zero transverse k-vector) corresponds to the central high-symmetry Γ point of the first BZ [the brightest spot in Fig. 4(a)]. Because of lattice periodicity, it also excites the central points in the extended BZs of the transmission spectrum as shown in Fig. 4(a), but no excitation at the M points near the edge of the first BZ. With a broad vertically oriented stripe beam, the *linear* spectrum (before self-action takes place) remains the same, except that each bright spot becomes elongated in horizontal direction. When the stripe beam is narrow, the spectrum becomes highly anisotropic, and this elongation turns virtually the bright spots into lines which extend to regions close to the four M points of the first BZ [Fig. 4(b)], although the power is still concentrated in the central bright line. Conversely, the *nonlinear* spectrum (after self-action takes place) changes dramatically, in which the power grows in regions close to the four M points where diffraction is anomalous, but decays almost to zero in the center where diffraction is normal [Fig. 4(c)]. For comparison, the *nonlinear* spectrum for the same stripe beam with *self-focusing* nonlinearity is shown in Fig. 4(d), where a discrete soliton train arising from the central Γ point is formed in the semi-infinite gap [18]. These observations agree perfectly with our numerical results from beam-propagation simulations [Fig. 4, bottom panels].

Finally, the orientation of the stripe beam is changed from vertical to diagonal (i.e., along one of the principle axes of the square lattice) [Fig. 5]. When the stripe beam is launched straight into the lattice (on-axis excitation), new features such as embedded solitons related to excitation of

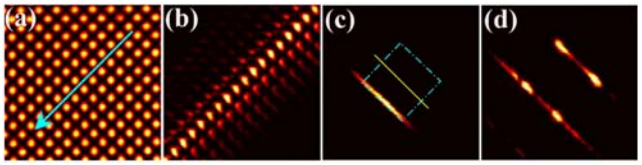

FIG. 5 (color online). Formation of a gap soliton train orientated along the lattice principle axis. (a) Lattice intensity pattern with an arrow illustrating the orientation and tilting direction of the probe beam; (b) output intensity pattern of the gap soliton train; (c) spectrum of the stripe beam tilted at the Bragg angle (yellow line marks spectrum location with no tilting angle); (d) spectrum of the gap soliton train.

Bloch modes at X points are observed, but a gap soliton train cannot arise from the M points since in this case the k-space spectrum of the probe beam covers X points [Fig. 5(c)] but provides no ''seeding'' momentum to the M points. However, once the stripe beam is tilted such that its spectrum ''touches'' one edge of the first BZ (off-axis excitation), a gap soliton train is realized again with modes arising from the four M points [Fig. 5(d)] due to Bragg reflection and spectrum reshaping. Interferograms reveal that, for this type of gap soliton train, adjacent spots are out of phase in directions both along and perpendicular to the initial stripe, characteristic of the Bloch modes close to M points of the first band [17] [see also Fig. 2(b)]. We have theoretically found such diagonally oriented (but tilted off-axis) gap soliton trains as well.

In summary, we have predicted and demonstrated the formation of gap soliton trains due to nonlinear transport and spectrum reshaping of a stripe beam in 2D induced lattices. The soliton trains arise from Bloch modes from the high-symmetry M points of the first photonic band, although some of these modes are initially not or only weakly excited from lattice scattering or diffraction. We note that in nonlinear spectrum reshaping (k-space evolution), while energy transfer between regions of normal diffraction and anomalous diffraction is not surprising [9], energy transfer from regions initially excited to regions initially unexcited is unexpected, as also mentioned in recent work with random-phase lattice solitons [19]. These results may have direct impact on the study of nonlinear Bloch-wave interaction and localization in periodic systems beyond optics such as condensed matter physics or Bose-Einstein condensates [2,3], where 2D gap solitons might arise from electronic or atomic Bloch modes weakly populated in the ground state by quantum fluctuations even if complete preparation of coherent wave packets at the corresponding band edge is not feasible.

This work was supported by NSF, AFOSR, PRF, and the 973 Program, 111 Project, NSFC and PCSIRT in China.

[1] S. Davydov, *Biology and Quantum Mechanics* (Pergamon, Oxford, 1982).
[2] W. P. Su *et al.*, Phys. Rev. Lett. **42**, 1698 (1979); M. Aïn *et al.*, *ibid.* **78**, 1560 (1997).
[3] B. Eiermann *et al.*, Phys. Rev. Lett. **92**, 230401 (2004); H. Saito and M. Ueda, *ibid.* **93**, 220402 (2004); E. A. Ostrovskaya and Y. S. Kivshar, *ibid.* **90**, 160407 (2003).
[4] W. Chen and D. L. Mills, Phys. Rev. Lett. **58**, 160 (1987); J. E. Sipe and H. G. Winful, Opt. Lett. **13**, 132 (1988); D. N. Christodoulides and R. I. Joseph, Phys. Rev. Lett. **62**, 1746 (1989); B. J. Eggleton *et al.*, *ibid.* **76**, 1627 (1996).
[5] Y. S. Kivshar, Opt. Lett. **18**, 1147 (1993).
[6] J. W. Fleischer *et al.*, Phys. Rev. Lett. **90**, 023902 (2003); Nature (London) **422**, 147 (2003).
[7] D. Mandelik *et al.*, Phys. Rev. Lett. **92**, 093904 (2004); D. N. Neshev *et al.*, *ibid.* **93**, 083905 (2004).
[8] D. N. Christodoulides and R. I. Joseph, Opt. Lett. **13**, 794 (1988); H. S. Eisenberg *et al.*, Phys. Rev. Lett. **81**, 3383 (1998).
[9] G. Bartal *et al.*, Phys. Rev. Lett. **94**, 163902 (2005); H. Trompeter *et al.*, *ibid.* **96**, 053903 (2006).
[10] I. Makasyuk *et al.*, Phys. Rev. Lett. **96**, 223903 (2006).
[11] F. Chen *et al.*, Opt. Express **13**, 4314 (2005); G. Bartal *et al.*, Opt. Lett. **31**, 483 (2006).
[12] S. I. Bozhevolnyi *et al.*, Phys. Rev. Lett. **86**, 3008 (2001); M. Notomi *et al.*, *ibid.* **87**, 253902 (2001).
[13] Z. Chen and K. McCarthy, Opt. Lett. **27**, 2019 (2002); H. Martin *et al.*, Phys. Rev. Lett. **92**, 123902 (2004).
[14] N. K. Efremidis *et al.*, Phys. Rev. Lett. **91**, 213906 (2003).
[15] J. Yang, New J. Phys. **6**, 47 (2004).
[16] J. Yang and T. I. Lakoba, Stud. Appl. Math. **118**, 153 (2007).
[17] A. A. Sukhorukov *et al.*, Phys. Rev. Lett. **92**, 093901 (2004); D. Trager *et al.*, Opt. Express **14**, 1913 (2006).
[18] Z. Chen *et al.*, Phys. Rev. Lett. **92**, 143902 (2004).
[19] O. Cohen *et al.*Nature (London) **433**, 500 (2005).

Highly optical damage resistant crystal: Zirconium-oxide-doped lithium niobate

Yongfa Kong,[a] Shiguo Liu, Yanjun Zhao, Hongde Liu, Shaolin Chen, and Jingjun Xu
The MOE Key Laboratory of Weak-Light Nonlinear Photonics, Nankai University, Ministry of Education, Tianjin 300457, China

(Received 6 June 2007; accepted 30 July 2007; published online 21 August 2007)

Usage of lithium niobate in nonlinear optics is seriously hampered by optical damage, in particular, where high intensity is needed. Doping with magnesium can improve its resistance against optical damage. However, since a rather large dopant concentration is required (more than 4.6 mol % MgO) and since the distribution coefficient is unfavorable, it is difficult to grow crystals of high optical quality. The authors show that by doping with zirconium, one can obtain at the same time a higher resistance against optical damage, a lower doping threshold (only 2.0 mol % ZrO_2), a distribution coefficient near 1.0, and a low coercive field that is only one-third of that of congruent $LiNbO_3$. These properties suggest that zirconium-doped lithium niobate is an excellent choice for nonlinear optical applications. © *2007 American Institute of Physics*. [DOI: 10.1063/1.2773742]

Lithium niobate ($LiNbO_3$) (LN) is one of the most important synthetic crystals. Since it has good electro-optic, acousto-optic, elasto-optic, piezoelectric, pyroelectric, and nonlinear properties, it is considered as the all-star material of nonlinear optics. Because of its availability, widespread use, and versatility, it has been dubbed by many as the "silicon of nonlinear optics."[1] Laser-induced optical damage was discovered in $LiNbO_3$ and $LiTaO_3$ crystals,[2] later also in various materials such as electro-optical dielectrics, semiconductors, and even organic polymers.[3] Although this effect, also called photorefraction, can be utilized in holographic storage, laser physics, information processing, and computation,[4,5] it hinders the usage of LN as frequency doubler, optical parametric oscillator, *Q*-switch, or optical waveguide. Therefore, the suppression of optical damage is one of the most important objectives for optical devices based on LN. A breakthrough was achieved by doping LN with magnesium. Above 4.6 mol % MgO (so-called threshold value),[6,7] the optical resistance improves by two orders of magnitude, thus, promoting practical applications of LN in nonlinear optics at high light intensities.

Another aspect concerns periodically poled $LiNbO_3$ (PPLN). This material permits to exploit the very high second-order nonlinear coefficient along the optical axis (up to 20 pm/V) and thus became one of the most popular nonlinear materials in the 1990s.[8–11] However, the large reversal field (21 kV/mm) of nominally pure congruent $LiNbO_3$ (CLN) limits the thickness of PPLN. It turned out that Mg-doped congruent $LiNbO_3$ (MgLN) crystals have the additional advantage of a much lower coercive field compared to undoped ones.[12] Therefore, periodically poled Mg-doped $LiNbO_3$ (PPMgLN) is the preferred material for ferroelectric domain engineering.

Today, MgLN crystal is among the most often used crystals in nonlinear optics.[13] Yet, two circumstances, namely, the high threshold (usually 5 mol % MgO for CLN) and the large distribution coefficient (~1.2), make it difficult to grow MgLN crystals of high optical quality. Other dopants that were found to reduce optical damage, such as Zn^{2+}, Sc^{3+}, In^{3+}, and Hf^{4+} ions,[14–17] suffer from the same drawbacks: large thresholds (7.0 mol % for Zn^{2+}, 5 mol % for In^{3+}, and 4.0 mol % for Hf^{4+} in the melt) and distribution coefficients deviating significantly from one above their threshold. As a consequence, none of these dopants became as popular as Mg^{2+}.

The demand for even higher optical damage resistance can be matched by increasing the doping concentration of MgO and especially the content of Li_2O. It was reported that Li-rich MgLN crystal can withstand one order of magnitude higher light intensities than Mg:CLN.[18] Further, near-stoichiometric $LiNbO_3$ (NSLN) crystals doped with Mg at low concentrations show four orders of magnitude improved optical damage resistance than conventional CLN.[19,20] Recently, the optical damage resistance of Mg:NSLN produced by vapor transport equilibration (VTE) has even reached 26 MW/cm^2.[21]

In this letter, we investigate zirconium-doped $LiNbO_3$ (ZrLN). We show that the crystals not only have similar optical damage resistance as Mg:NSLN but also have a doping threshold lower than 2.0 mol % and a distribution coefficient close to one. These properties make Zr an excellent choice for doping of $LiNbO_3$ against optical damage.

A series of ZrLN crystals were grown along the *c* axis with the conventional Czochralski method. The melt composition was Li/Nb=48.4/51.6, and 1.0, 1.5, 1.7, 2.0, 3.0, 4.0, and 5.0 mol % ZrO_2 was added into the melt. The samples were labeled as Zr1N, Zr1.5LN, Zr1.7LN, Zr2LN, Zr3LN, Zr4LN, and Zr5LN, respectively. Two thin plates were cut from the top and the tail part of each of the as-grown crystals for x-ray fluorescence analysis. Then, 3 and 1 mm thick *y* plates were cut from the crystal for characterization of photorefraction and absorption, and 0.5 mm thick *z* plates for domain reversal studies. All plates were polished to optical grade. For comparison, CLN and MgLN crystals doped with 6.5 mol % MgO (labeled as Mg6.5LN) were also grown.

Optical damage is indicated by a transmitted light beam becoming smeared and elongated along the *c* axis and furthermore by a decrease of the intensity of its central part. The ability of ZrLN crystals to resist optical damage was therefore roughly characterized by the intensity threshold at

[a]Electronic mail: kongyf@nankai.edu.cn

0003-6951/2007/91(8)/081908/3/$23.00

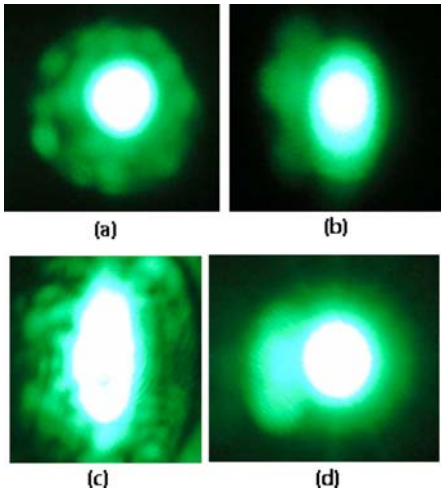

FIG. 1. (Color online) Distortion of transmitted argon laser beam spots after 5 min of irradiation. [(a)–(c)] Zr1.7LN; (d) Zr2LN. The light intensities are (a) 1.3×10^3 W/cm^2, (b) 1.3×10^4 W/cm^2, (c) and (d) 2.0×10^7 W/cm^2.

which an onset of distortion of a transmitted laser beams passing through a 3 mm *y*-cut plate is observed. Figure 1 shows four transmitted light spots for different samples and intensities after 5 min of irradiation by an argon laser (514.5 nm). As the doping concentration reaches 2.0 mol % ZrO_2, ZrLN crystals can withstand the highest intensities that we could produce (2.0×10^7 W/cm^2) without noticeable beam smearing [Fig. 1(d)]. In the case of Zr1.7LN and for lower doping, the transmitted light spot apparently diffused along the *c* axis [Fig. 1(c)]. At the same conditions, Mg6.5LN can withstand only a maximum intensity of 5.0×10^5 W/cm^2 without spot distortion. From these results, we conclude that the optical damage resistance of sample Zr2LN is at least 40 times larger than that of Mg6.5LN.

In order to characterize the optical damage of these crystals quantitatively, the light-induced change of the refractive index n_e of these crystals was measured by two-beam holography.[22] Refractive index changes resulting from an irradiation of 150 mW/cm^2 over 1 min are plotted in Fig. 2 for all ZrLN samples. At this exposure time, the refractive index change is in saturation. We can see from this figure that the change of refractive index drops rapidly with increasing doping concentration of ZrO_2 and becomes practically independent of doping above a threshold of 2.0 mol % with a value of about 7×10^{-7}. Under similar testing conditions, the change of the saturation refractive index of Mg6.5LN is 7.6×10^{-6}; i.e., photorefraction of all ZrLN samples is smaller than that of Mg6.5LN. For samples doped above 2.0 mol % ZrO_2, the refractive index change is even one order of magnitude smaller.

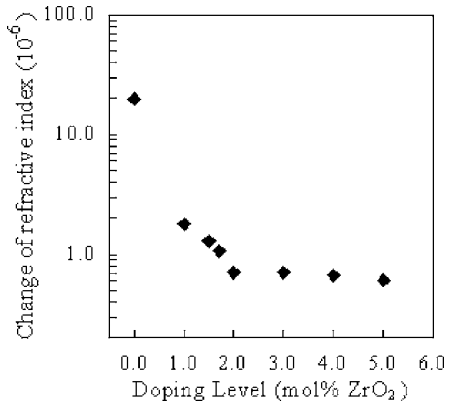

FIG. 2. Light-induced change of the refractive index in saturation as a function of the level of doping with ZrO_2.

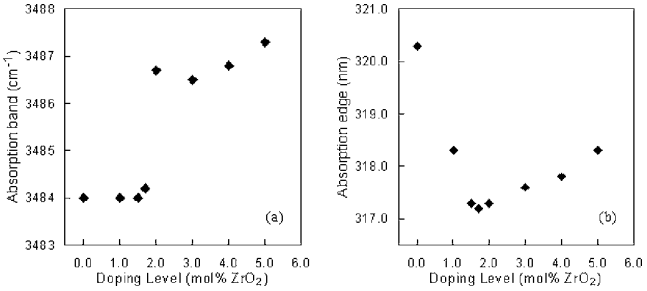

FIG. 3. Relationship between absorption spectra and level of doping of ZrO_2. (a) OH^- absorption band and (b) absorption edge.

It is well known that OH^- absorption bands of doped $LiNbO_3$ crystals exhibit striking shifts from the position at 3484 cm^{-1} of pure $LiNbO_3$ toward higher wave numbers when the doping concentration exceeds a certain threshold. Furthermore, the absorption edge has a violetshift below the threshold and a redshift above the threshold with increasing doping. We therefore measured infrared and UV-visible absorption spectra at room temperature with a Magna-560 Fourier transform infrared spectrophotometer and a Beckman DU-8B spectrophotometer, respectively, with light transmitting through 1 mm thick *y* plates. Figure 3(a) shows the shift of the position of the OH^- absorption bands of ZrLN samples. The absorption band shifts rather abruptly from 3484 to 3487 cm^{-1} at a doping concentration of ZrO_2 of 2 mol %. Figure 3(b) shows the shift of the absorption edges of ZrLN crystals as a function of ZrO_2 doping. Here, the absorption edge was defined as the wavelength where the absorption coefficient is equal to 20 cm^{-1}. Obviously, the above-mentioned characteristics at the threshold can also be seen in ZrLN and indicate that the doping threshold is between 1.7 and 2.0 mol % ZrO_2.

The distribution coefficients were calculated from the concentrations of Zr as determined by x-ray fluorescence analysis. To this purpose, samples from the top plate, the tail plate, and the polycrystalline material left in the crucible were cracked and milled to fine powder (diameter below 40 μm). The distribution coefficients shown in Fig. 4 are the average values found for the top and tail plates. From Fig. 4, we see that the distribution coefficient of Zr in $LiNbO_3$ has only a small fluctuation around 1.0 for the whole doping range from 1.0 to 5.0 mol %. The maximum value is 1.04 and the minimum value is 0.97; i.e., the distribution coefficient of Zr^{4+} is much closer to one than that of Mg. In fact, 10 cm long Zr2LN single crystals of 8.0 cm diameter have been grown and the concentration variation of Zr from top to bottom turned out to be less than 3%.

The domain reversal behavior was investigated by the conventional electric-field method in which a poling voltage was applied with a uniform electrode consisting of LiCl electrolyte. For this study 0.5 mm thick *z* plates were employed. The electric coercive field was defined as the one where the corresponding poling current density exceeds 1.1 μA/cm^2. Figure 5 shows the domain reversal field in ZrLN as a function of zirconium doping. With increasing doping, the coer-

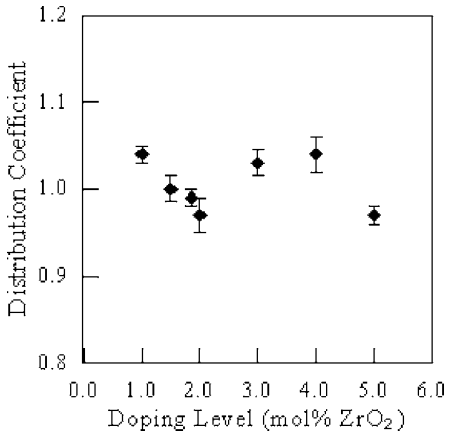

FIG. 4. Dependence of the distribution coefficient of Zr^{4+} ions in ZrLN crystals on various doping levels of ZrO_2.

cive field decreases rapidly at first, reaches a minimum (7.2 kV/mm) at 2.0 mol % ZrO_2, and then slightly increases. The coercive field of sample Zr2LN is roughly one-third of that of CLN but larger than that for sample Mg6.5LN (5.2 kV/mm).

As mentioned above, the optical damage resistance of Mg:NSLN crystals grown from K_2O added solution and from Li_2O excess melt is in the range of 2–8 MW/cm^2,[19,20] which is close to ZrLN. However, the composition of these crystals is changing along the length of the crystal. In principle, this problem could be solved, but only at the costs of using a more sophisticated method than the conventional Czochralski method, namely, the double crucible mothed.[23] Further, optical damage resistance of Mg:NSLN crystal could be pushed up to 26 MW/cm^2 by VTE with a refractive index change decreased to as low as 4.6×10^{-7}.[21] These values are better than those of ZrLN; however, this technique can only be applied to thin wafers. Therefore, ZrLN is still the best choice if crystals of large diameter are required and an optical damage resistance up to 10^7 W/cm^2 is sufficient.

Although both, Hf^{4+} and Zr^{4+}, are tetravalent ions, the threshold concentration of Zr is just half of that of Hf (4 mol % in the melt), and the saturation refractive index change of Zr2LN is one order of magnitude smaller than that of Hf4LN (8.7×10^{-6}).[24] The question remains, why ZrLN has such excellent resistance against optical damage as compared with HfLN and MgLN. We think that it might be connected to the fact that the chemical element Zr is the neighbor of Nb and that the replacement of Zr^{4+} ions against Nb^{5+} on Li sites is energetically favored. However, more experimental investigations are needed to clarify this question.

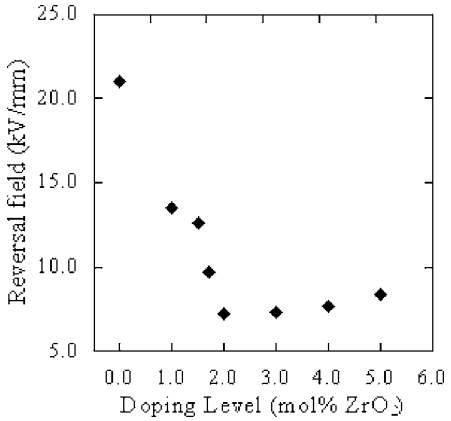

FIG. 5. Switching field of ZrLN crystal as a function of doping level of ZrO_2.

In summary, ZrO_2-doped lithium niobate crystals were grown. The doping threshold for optical damage resistance is below 2.0 mol % ZrO_2, while the distribution coefficient is close to one. Above threshold, the optical damage resistance of ZrLN is more than 40 times better than that of Mg6.5LN. The refractive index change of sample Zr2LN is one order of magnitude smaller than that of sample Mg6.5LN. The experimental results support the conclusion that ZrLN might replace MgLN since it has better properties and possibly a broader range of practical applications.

This work was financially supported by Chinese National Key Basic Research Special Fund (No. 2006CB921703), National Basic Research Program of China (No. 2007CB307002), Program for Changjiang Scholars and Innovative Research Team in University, and National Natural Science Foundation of China (60578019). The authors greatly appreciated valuable advice by Romano Rupp (Nankai University-TEDA Applied Physics School & Vienna University-Faculty of Physics), and support by the Chinese-Austrian exchange programme (OeAD-WTZ CN24/2007) is greatfully acknowledged.

[1] N. Broderick, Nat. Mater. (2002), 16 November update.
[2] A. Askin, G. D. Boyd, J. M. Dziedzic, R. G. Smith, A. A. Ballman, J. J. Levinstein, and K. Nassau, Appl. Phys. Lett. **9**, 72 (1966).
[3] Y. Zhang, R. Burzynski, S. Ghosal, and M. Casstevens, Adv. Mater. (Weinheim, Ger.) **8**, 111 (1996).
[4] J. F. Heanue, M. C. Bashaw, and L. Hesselink, Science **265**, 749 (1994).
[5] K. Buse, A. Adibi, and D. Psaltis, Nature (London) **393**, 665 (1998).
[6] G. Zhong, J. Jin, and Z. Wu, *Proceedings of the 11th International Quantum Electronics Conference* (IEEE, New York, 1980), p. 631.
[7] D. A. Bryan, R. Gerson, and H. E. Tomaschke, Appl. Phys. Lett. **44**, 847 (1984).
[8] M. Yamada, N. Nada, M. Saitoh, and K. Watanabe, Appl. Phys. Lett. **62**, 435 (1993).
[9] L. E. Myers, R. C. Eckardt, M. M. Fejer, R. L. Byer, W. R. Bosenberg, and J. W. Pierce, J. Opt. Soc. Am. B **12**, 2102 (1995).
[10] S. Zhu, Y. Zhu, and N. Ming, Science **278**, 843 (1997).
[11] Y. Lu, Y. Zhu, Y. Chen, S. Zhu, N. Ming, and Y. Feng, Science **284**, 1822 (1999).
[12] K. Mizuuchi, K. Yamamoto, and M. Kato, Electron. Lett. **32**, 2091 (1996).
[13] D. N. Nikogosyan, *Nonlinear Optical Crystals: A Complete Survey* (Springer, New York, 2005), Vol. 4, p. 162.
[14] T. R. Volk, V. J. Pryalkin, and M. M. Rubinina, Opt. Lett. **15**, 996 (1990).
[15] J. K. Yamamoto, K. Kitamura, N. Iyi, S. Kimura, Y. Furukawa, and M. Sato, Appl. Phys. Lett. **61**, 2156 (1992).
[16] Y. Kong, J. Wen, and H. Wang, Appl. Phys. Lett. **66**, 280 (1995).
[17] E. P. Kokanyan, L. Razzari, I. Cristiani, V. Degiorgio, and J. B. Gruber, Appl. Phys. Lett. **84**, 1880 (2004).
[18] J. Wen, L. Wang, Y. Tang, and H. Wang, Appl. Phys. Lett. **53**, 260 (1988).
[19] Y. Furukawa, K. Kitamura, S. Takekawa, K. Niwa, and H. Hatano, Opt. Lett. **23**, 1892 (1998).
[20] Y. Furukawa, K. Kitamura, S. Takekawa, A. Miyamoto, M. Terao, and N. Suda, Appl. Phys. Lett. **77**, 2494 (2000).
[21] S. Chen, H. Liu, Y. Kong, Z. Huang, J. Xu, and G. Zhang, Opt. Mater. (Amsterdam, Neth.) **29**, 885 (2007).
[22] H. Kogelnik, Bell Syst. Tech. J. **48**, 2909 (1969).
[23] K. Kitamura, Y. Furukawa, Y. Ji, M. Zgonik, C. Medrano, G. Montemezzani, and P. Günter, J. Appl. Phys. **82**, 1006 (1997).
[24] S. Li, S. Liu, Y. Kong, D. Deng, G. Gao, Y. Li, H. Gao, L. Zhang, Z. Hang, S. Chen, and J. Xu, J. Phys.: Condens. Matter **18**, 3527 (2006).

Recursion formula for reflectance and the enhanced effect on the light group velocity control of the stratified and phase-shifted volume index gratings

Guoquan Zhang, Weiyue Che, Bin Han, and Yiling Qi

Photonics Center, College of Physics Science, Nankai University, Tianjin 300071, China and The Key Laboratory of Advanced Technique and Fabrication for Weak-Light Nonlinear Photonics Materials, Ministry of Education, Nankai University, Tianjin 300457, China and Tianjin Key Laboratory of Photonics Materials and Technology for Information Science, Nankai University, Tianjin 300457, China

zhanggq@nankai.edu.cn

Abstract: We derived a recursion formula for the reflectance of the stratified and phase-shifted volume index gratings. The characteristics of the reflectance spectra of the stratified and phase-shifted volume index gratings were studied based on the recursion formula. It is shown that narrow bandwidth transparency peaks appear within the stop-band of the reflectance spectrum of the volume index gratings due to the intervention of the homogeneous buffer layers that induce the phase-shifts between neighboring volume index gratings. The spectral positions of the transparency peaks can be shifted within the stop-band by controlling the phase-shift, i.e., the buffer layer thickness. The described properties may find applications in addressable band-pass filter, switching, wavelength division multiplexing, and de-multiplexing. The dispersion near the transparency peaks of the stratified and phase-shifted volume index grating is found to be sharply enhanced as compared to the uniform volume index gratings. Significantly enhanced control on the group velocity of light by several orders of magnitude while keeping high transmittance is demonstrated in the stratified and phase-shifted volume index grating.

OCIS codes: (230.4170) Multilayers; (260.2030) Dispersion; (050.2770) Gratings; (060.1810) Couplers, switches, and multiplexers.

References and links

1. P. Yeh, *Optical Waves in Layered Media* (Wiley, New York, 1988).
2. J. D. Joannopoulos, R. D. Meade, and J. N. Winn, *Photonic Crystals: Molding the Flow of Light* (Princeton University Press, Princeton, 1995).
3. R. C. Alferness, C. H. Joyner, M. D. Divino, M. J. R. Martyak, and L. L. Buhl, "Narrowband grating resonator filters in InGaAsP/InP waveguides," Appl. Phys. Lett. **49**, 125–127 (1986).
4. G. P. Agrawal and S. Radic, "Phase-Shifted Fiber Bragg Gratings and their Application for Wavelength Demultiplexing," IEEE Photon. Technol. Lett. **6**, 995–997 (1994).
5. R. Zengerle and O. Leminger, "Phase-shifted Bragg-Grating Filters with Improved Transmission Characteristics," J. Lightwave Technol. **13**, 2354–2358 (1995).
6. L. Wei and J. W. Y. Lit, "Phase-Shifted Bragg Grating Filters with Symmetrical Structures," J. Lightwave Technol. **15**, 1405–1410 (1997).

7. F. Bakhti and P. Sansonetti, "Design and Realization of Multiple Quater-Wave Phase-Shifts UV-Written Bandpass Filter in Optical Fibers," J. Lightwave Technol. **15**, 1433–1437 (1997).
8. Ch. Martinez and P. Ferdinand, "Analysis of phase-shifted fiber Bragg gratings written with phase plate," Appl. Opt. **38**, 3223–3228 (1999).
9. S. Longhi, M. Marano, P. Laporta, O. Svelto, and M. Belmonte, "Propagation, manipulation, and control of picosecond optical pulses at 1.5 μm in fiber Bragg gratings," J. Opt. Soc. Am B **19**, 2742–2757 (2002).
10. Y. Painchaud, A. Chandonnet, and J. Lauzon, "Chirped fibre gratings produced by tilting the fibre," Electron. Lett. **31**, 171–172 (1995).
11. B. Malo, S. Thériault, D. C. Johnson, F. Bilodeau, J. Albert, and K. O. Hill, "Apodised in-fibre Bragg grating reflectors photoimprinted using a phase mask," Electron. Lett. **31**, 223-225 (1995).
12. Ch. Martinez, S. Magne, and P. Ferdinand, "Apodized fiber Bragg gratings manufactured with the phase plate process," Appl. Opt. **41**, 1733–1740 (2002).
13. R. V. Johnson, A. R. Tanguay, "Stratified volume holographic optical elements," Opt. Lett. **13 ,** 189–191 (1988).
14. G. P. Nordin, R. V. Johnson, A. R. Tanguay, "Diffraction properties of stratified volume holographic optical elements," J. Opt. Soc. Am. A **9 ,** 2206–2217 (1992).
15. R. De Vré and L. Hesselink, "Analysis of photorefractive stratified volume holographic optical elements," J. Opt. Soc. Am. B **11**, 1800–1808 (1994).
16. J. J. Stankus, S. M. Silence, W. E. Moerner, and G. C. Bjorklund, "Electric-field-switchable stratified volume holograms in photorefractive polymers," Opt. Lett. **19**, 1480–1482 (1994).
17. V. M. Petrov, C. Caraboue, J. Petter, T. Tschudi, V. V. Bryksin, and M. P. Petrov, "A dynamic narrow-band tunable optical fliter," Appl. Phys. B **76**, 41–44 (2003).
18. Y. Lai, W. Zhang, L. Zhang, J. A. R. Williams, and I. Bennion, "Optically tumable fiber grating transmission filters," Opt. Lett. **28**, 2446–2448 (2003).
19. A. D'Orazio, M. De Sario, V. Petruzzelli, and F. Prudenzano, "Photonic band gap filter for wavelength division multiplexer," Opt. Express **11**, 230–239 (2003).
20. M. Yamada and K. Sakuda, "Analysis of almost-periodic distributed feedback slab waveguides via a fundamental matrix approach," Appl. Opt. **26**, 3474–3478 (1987).
21. M. McCall, "On the application of coupled mode theory for modeling fiber Bragg gratings," J. Lightwave Technol. **18**, 236–242 (2000).
22. M. A. Rodriguez, M. S. Malcuit, and J. J. Butler, "Transmission properties of refrective index-shifted Bragg gratings," Opt. Commun. **177**, 251–257 (2000).
23. S. Khorasani and K. Mehrany, "Differential transfer-matrix method for solution of one-dimensional linear non-homogeneous optical sturctures," J. Opt. Soc. Am. B **20**, 91–96 (2003).
24. S. Khorasani and A. Adibi, "New analytical approach for computation of band structure in one-dimensional periodic media," Opt. Commun. **216**, 439–451 (2003).
25. J. J. Monzón, T. Yonte, and L. L. Sánchez-Soto, "Charcterizing the reflectance of periodic layered media," Opt. Commun. **218**, 43–47 (2003).
26. I. S. Nefedov and S. A. Tretyakov, "Photonic band gap structure containing metamaterial with negative permittivity and permeability," Phys. Rev. E **66**, 036611-1–4 (2002).
27. J. R. Birge and F. X. Kärtner, "Efficient analytic computation of dispersion from multilayer structures," Appl. Opt. **45**, 1478-1483 (2006).
28. D. Yevick and L. Thylén, "Analysis of gratings by the beam-propagation method," J. Opt. Soc. Am. **72**, 1084–1089 (1982).
29. L. Thylen and D. Yevick, "Beam propagation method in anisotropic media," Appl. Opt. **21**, 2751–2754 (1982).
30. L Thylen and Ch. M. Lee, "Beam-propagation method based on matrix diagonalization," J. Opt. Soc. Am. A **9**, 142–146 (1992).
31. Y. Tsuji, M. Koshiba, and N. Takimoto, "Finite element beam propagation method for anisotropic optical waveguides," J. Lightwave Technol. **17**, 723–728 (1999).
32. P. K. Kelly and M. Piket-May, "Propagation characteristics for a one-dimensional grounded finite height finite length electromagnetic crystal," J. Lightwave Technol. **17**, 2008–2012 (1999).
33. L. A. Coldren and S. W. Corzine, *Diode Lasers and Photonic Integrated Circuits* (Wiley, New York, 1995).
34. M. Scalora, R. J. Flynn, S. B. Reinhardt, R. L. Fork, M. J. Bloemer, M. D. Tocci, C. M. Bowden, H. S. Ledbetter, J. M.Bendickson, and R. P. Leavitt, "Ultrashort pulse propagation at the photonic band edge: large tunable group delay with minimal distortion and loss," Phys. Rev. E **54**, R1078-R1081 (1996).
35. S. H. Lin, K. Y. Hsu, and P. Yeh, "Experimental observation of the slowdown of optical beams by a volume-index grating in a photorefractive $LiNbO_3$ crystal," Opt. Lett. **25**, 1582–1584 (2000).
36. S. Zhu, N. Liu, H. Zheng, and H. Chen, "Time delay of light propagation through defect modes of one-dimensional photonic band-gap structures," Opt. Commun. **174**, 139-144 (2000).
37. J. Liu, B. Shi, D. Zhao, and X. Wang, "Optical delay in defective photonic bandgap structures," J. Opt. A: Pure Appl. Opt. **4**, 636–639 (2002).
38. S. Bette, C. Caucheteur, M. Wuilpart, P. Mégret, R. Garcia-Olcina, S. Sales, and J. Capmany, "Spectral characterization of differential group delay in uniform fiber Bragg gratings," Opt. Express **13**, 9954-9960 (2005).

1. Introduction

The spectral properties of the periodically layered structures such as volume index gratings and one-dimension photonic crystals have been intensively studied because of their many potential applications in optical communication and information processing [1, 2]. To get a desired spectral response, modification on structure parameters such as refractive index and structure periods or structure defects is introduced to the periodically layered structure; therefore, structures such as the phase-shifted gratings [3-8], the chirped [9, 10], and the apodized gratings [11, 12] in optical fiber and the stratified volume holographic optical elements [13-16] have been proposed. Many device applications such as the narrow-bandwidth band-stop or band-pass filters [3, 5, 6, 17, 18] as well as wavelength division multiplexer and de-multiplexer [4, 19] have also been suggested and demonstrated experimentally. Practically, to design a periodically layered structure for a specific application, a precise knowledge on the spectral response of the periodically layered structure is necessary. Various methods were developed to calculate the spectral response of the periodically layered structure. The transfer matrix approach [20] is one of the most popular methods, and it has been extended and modified [21-25] to calculate various types of the periodically layered structures. In this approach, the layered structure is divided into short segments with uniform grating parameters. The fundamental matrices are determined for each segment based on the coupled wave theory, and the spectral response characteristics of the layered structure is obtained by multiplying these fundamental matrices in certain phase conditions of the grating at the interface between two adjacent segments. The transfer matrix approach was also applied to calculate the light propagation in one-dimension photonic crystal with a negative permittivity and permeability, the photonic bandgap was found to be enhanced dramatically in these metamaterials [26]. Recently, Birge and Kärtner [27] demonstrated an inductive method to compute derivatives of reflection phase for layered media by using the transfer matrix formalism, which leads to an efficient way for accurately computing dispersion significantly faster than with standard finite-difference methods. The beam propagation method [28-31] is another flexible and broadly applicable numerical tool to characterize the beam propagation behaviors in periodically layered structures, where the distributed optical inhomogeneities of a periodically layered structure are approximated by a discrete sequence of physically and mathematically infinitesimally thin phase and/or polarization modulation layers, which is intervened with optically homogeneous layers of finite thickness. The stratified volume holographic optical elements [13-16] were suggested based on the concept of separating the volume holographic structure into a sequence of discrete thin modulation layers used in the beam propagation method. In a stratified volume holographic optical element, a sequence of thin photosensitive holographic recording layers are interleaved with photo-insensitive buffer layers. Although a grating recorded in any individual photosensitive layer exhibits Raman-Nath characteristics because of its thin thickness, a stratified volume holographic optical element with even a small number of photosensitive layers, each spaced from its neighbors by a buffer layer of appropriate thickness, shows a Bragg-like diffraction behavior. The finite-difference time-domain simulation code is a powerful numerical method to simulate the light propagation behaviors in various material systems. It was employed recently to calculate the propagation characteristics of a one-dimension photonic crystal with finite length and finite height [32].

In this paper, we have designed a periodically layered structure, a stratified and phase-shifted volume index grating (SPVIG), consisting of a sequence of discrete thick volume index gratings interleaved with optically homogeneous buffer layers. A recursion formula for the reflectance of the SPVIGs is derived, and its reflectance properties are studied under various conditions. As compared to a single uniform volume index grating (SG), an enhanced effect on the control of light group velocity with a high transmittance by using the SPVIGs is demonstrated.

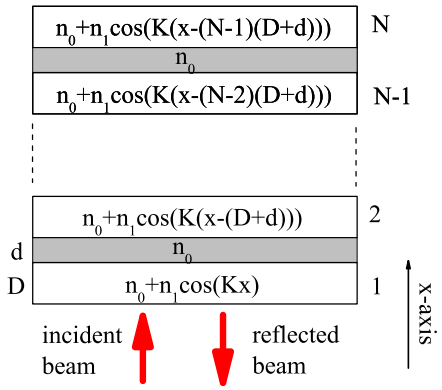

Fig. 1. The structure of the SPVIG.

2. The structure of SPVIG

Figure 1 shows the structure of the SPVIG, in which N discrete thick volume index grating layers are interleaved with N-1 optically homogeneous buffer layers. The buffer layers provide the phase-shifts between the neighboring grating layers. The thicknesses of the volume index grating layers and the buffer layers are D and d, respectively. For the sake of simplicity, the averaged refractive indices for both the grating layers and the buffer layers are set to be n_0. The refractive index modulation amplitude for the grating layers is n_1, and the grating wave vector along x-axis is $K = 2\pi/\Lambda$ with Λ being the grating spacing. Therefore the refractive index distribution of the j-th grating layer can be expressed as $n_j(x) = n_0 + n_1\cos(K(x-(j-1)(D+d)))$.

3. Derivation of the recursion formula for the reflectance of SPVIG

Supposing a TE (or TM) polarized plane wave $E(x,t) = E(x)\exp(-i\omega t)$ is incident normally onto the SPVIG at $x = 0$, where $E(x)$ is the complex amplitude of the electric field of the light and ω is the angular frequency of the light. The wave equation describing the light propagation along the x-axis is given by [1]

$$\frac{\partial^2 E(x)}{\partial x^2} + [\frac{\omega}{c}n(x)]^2 E(x) = 0, \tag{1}$$

with c being the light speed in vacuum. For the simplest case when there is only one grating layer, the solution of Eq. (1) can be expressed as

$$E_1(x) = A_1(x)e^{ik_0 x} + B_1(x)e^{-ik_0 x}, \tag{2}$$

where $A_1(x)$ and $B_1(x)$ are the complex amplitudes of the forward and the backward propagating waves, respectively, and $k_0 = 2\pi n_0/\lambda$ with λ being the wavelength of the incident light in vacuum. By substituting the refractive index $n(x)$ into Eq. (1), and neglecting the terms higher than $\sim n_1^2$, under the slowly varying amplitude approximation, we obtain two coupled differential equations for $A_1(x)$ and $B_1(x)$

$$\frac{\partial A_1(x)}{\partial x} = i\kappa B_1(x)e^{-i\Delta kx}, \tag{3}$$

and

$$\frac{\partial B_1(x)}{\partial x} = -i\kappa A_1(x)e^{i\Delta kx}, \tag{4}$$

respectively. Where $\kappa = \pi n_1/\lambda$ is the coupling constant, $\Delta k = 2k_0 - K$ is the momentum mismatch. The general analytical solutions for $A_1(x)$ and $B_1(x)$ can be written as

$$A_1(x) = (A_1(0)\cosh(sx) + C_1\sinh(sx))e^{-i\Delta kx/2}, \tag{5}$$

and

$$B_1(x) = -\frac{i}{\kappa}e^{i\Delta kx}\frac{\partial A_1(x)}{\partial x}, \tag{6}$$

respectively. Where $A_1(0)$ is the amplitude of the incident light at $x = 0$, s is given by $s = (\kappa^2 - (\Delta k/2)^2)^{1/2}$, and C_1 is a parameter determined by the boundary conditions. Under the boundary condition $B_1(D) = 0$, the reflection coefficient of the grating layer is given by

$$r_1 = \frac{B_1(0)}{A_1(0)} = \frac{i\kappa\sinh(sD)}{s\cosh(sD) - i(\Delta k/2)\sinh(sD)}. \tag{7}$$

Now supposing we know the reflection coefficient r_N of a N-layer SPVIG with N grating layers interleaved with N-1 buffer layers, we will derive a recursion formula for the reflection coefficient r_{N+1} of a $(N+1)$-layer SPVIG. Such a recursion technique for calculation of reflection coefficient is generally used in distributed feedback laser [33].

It is evident that the amplitude of the electric field $E_j(x)$ in the j-th grating layer is the summation of the forward and the backward propagation waves $E_j(x) = A_j(x)\exp(ik_0(x-(j-1)(D+d))) + B_j(x)\exp(-ik_0(x-(j-1)(D+d)))$. The amplitudes of the forward and backward propagation waves in the first layer are described by Eqs. (5) and (6), regardless of the layer number of the SPVIG. In each case, the parameter C_1 is determined by the boundary conditions at the two interfaces of the buffer layer sandwiched between the first and the second grating layers. These boundary conditions can be expressed as

$$A_1(D)e^{ik_0d} = A_2(D+d), \tag{8}$$

and

$$B_1(D) = B_2(D+d)e^{ik_0d}, \tag{9}$$

respectively. By combining the expression of the reflection coefficient of the N-layer SPVIG $r_N = B_2(D+d)/A_2(D+d)$, we obtain the parameter C_1 as a function of r_N

$$C_1 = \frac{i\kappa r_N\cosh(sD)e^{-i\Delta kD+2ik_0d} + i\frac{\Delta k}{2}\cosh(sD) - s\sinh(sD)}{-i\kappa r_N\sinh(sD)e^{-i\Delta kD+2ik_0d} - i\frac{\Delta k}{2}\sinh(sD) + s\cosh(sD)}A_1(0). \tag{10}$$

By substituting Eq. (10) into Eqs.(5) and (6), we obtain the recursion formula for the reflection coefficient r_{N+1} of the (N+1)-layer SPVIG

$$r_{N+1} = \frac{B_1(0)}{A_1(0)} = \frac{sr_N\cosh(sD)e^{-i\Delta kD+2ik_0d} + i\frac{\Delta k}{2}r_N\sinh(sD)e^{-i\Delta kD+2ik_0d} + i\kappa\sinh(sD)}{-i\kappa r_N\sinh(sD)e^{-i\Delta kD+2ik_0d} - i\frac{\Delta k}{2}\sinh(sD) + s\cosh(sD)}. \tag{11}$$

Therefore the reflectance of the (N+1)-layer SPVIG is $R_{N+1} = |r_{N+1}|^2$ and the transmittance T_{N+1} can be obtained through $T_{N+1} = 1 - R_{N+1}$. The recursion formula (11) provides a precise prediction of the characteristics of the reflectance spectra of the SPVIGs with a normal incident light. It is worthy of mention that for the case of oblique incidence the results will be different

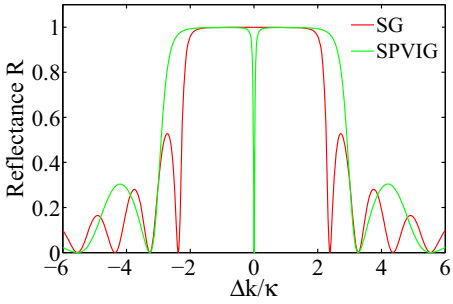

Fig. 2. Reflectance spectra of a SG (red) and a 2-layer SPVIG (green). The grating parameters for both cases are $\Lambda = 0.5\ \mu$m and $n_1 = 4 \times 10^{-4}$. Other parameters are set to be D = 3 mm, d = 2.25 μm and $n_0 = 1.55$, respectively. The thickness of the SG is 6 mm for comparison.

for the TE and the TM waves, however, a detailed discussion on the oblique incidence case deserves another full-length paper and is beyond the scope of this paper.

In the following section, we will discuss the characteristics of the reflectance spectra of the SPVIGs.

4. Characteristics of the reflectance spectra of SPVIGs

To study the characteristics of the reflectance spectra and to understand the effects of the buffer layers on the reflectance spectra, let us first consider the simplest SPVIG with N=2, where a buffer layer is sandwiched between two volume index grating layers. By substituting Eq. (7) into Eq. (11), we obtain the reflection coefficient for the 2-layer SPVIG

$$r_2 = \frac{i\kappa \sinh(sD)\left(1 + \frac{s\cosh(sD)+i\frac{\Delta k}{2}\sinh(sD)}{s\cosh(sD)-i\frac{\Delta k}{2}\sinh(sD)} e^{-i\Delta kD+i2k_0 d}\right)}{\frac{\kappa^2\sinh^2(sD)}{s\cosh(sD)-i\frac{\Delta k}{2}\sinh(sD)} e^{-i\Delta kD+i2k_0 d} + s\cosh(sD) - i\frac{\Delta k}{2}\sinh(sD)}. \tag{12}$$

In the case with a Bragg-matched incident wavelength λ_0 for the volume index grating layer, i.e., $\Delta k = 0$, the reflection coefficient of the 2-layer SPVIG can be simplified to be

$$r_2 = \frac{i\kappa \sinh(sD)(1 + e^{i2k_0 d})}{\frac{\kappa^2\sinh^2(sD)}{s\cosh(sD)} e^{i2k_0 d} + s\cosh(sD)}. \tag{13}$$

It is evident that the reflection coefficient r_2 is equal to zero under the condition $2k_0 d = (2m+1)\pi$, where m is an integer. Therefore a transparency peak appears in the stop-band of the reflectance spectrum of the volume index grating, as shown in Fig. 2, where the reflectance spectrum of a 2-layer SPVIG is shown. Similar phenomena were also reported in phase-shifted fiber Bragg gratings [4, 5, 6, 7, 8]. In the simulation, the structure parameters for the 2-layer SPVIG are $n_0 = 1.55$, $n_1 = 4 \times 10^{-4}$, $\Lambda = 0.5\ \mu$m, $\lambda_0 = 1.55\ \mu m$, D = 3 mm and d = 2.25 μm, respectively. It is evident that such a transparency peak is a result of the interference between the forward waves and the backward waves reflected from the first and the second volume index grating layers. For comparison, the reflectance spectrum of a 6-mm SG with the same grating

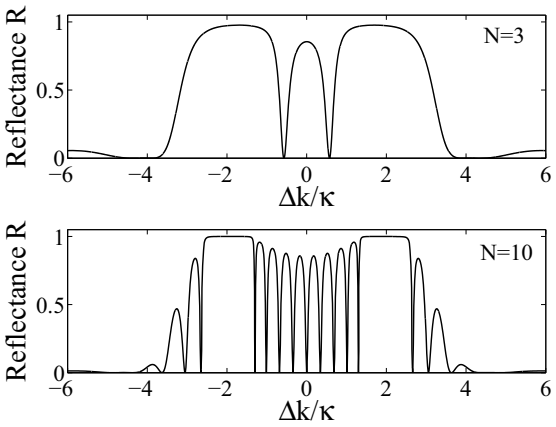

Fig. 3. The reflectance spectra of the SPVIGs with N=3 (a) and N=10 (b), respectively. The parameters for both cases are set to be $n_0 = 1.55$, $n_1 = 4 \times 10^{-4}$, D = 2 mm, $\Lambda = 0.5$ μm, and d = 2.25 μm, respectively.

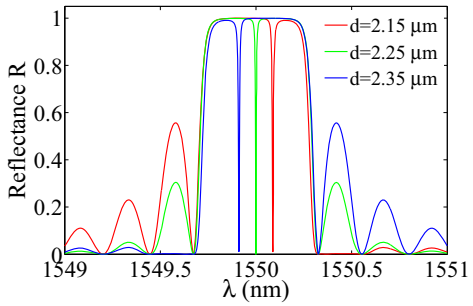

Fig. 4. Shift of the transparency wavelength within the stop-band by controlling the thickness of the buffer layer in a 2-layer SPVIG. The thicknesses of the buffer layers are 2.15, 2.25 and 2.35 μm for the red, green and blue curves, respectively. Other parameters are the same for three curves: $n_0 = 1.55$, $n_1 = 4 \times 10^{-4}$, D = 3 mm, and $\Lambda = 0.5$ μm, respectively.

parameters is also shown in Fig. 2. A broadening effect of the stop-band of the reflectance spectrum is also found for the SPVIG due to the interleave of the buffer layer.

The reflectance spectrum of a multilayer SPVIG can be calculated easily by using the recursion formula (see Eq. (11)). Figure 3 shows the reflectance spectra of a 3-layer (a) and a 10-layer (b) SPVIGs as examples. The structure parameters are the same as those of Fig. 2 except for D = 2 mm in Fig. 3. It is found that the number of the transparency peaks within the stop-band is equal to N-1, i.e., the number of the buffer layers in the structure. Therefore, two and nine transparency peaks appear in the reflectance spectra of the 3-layer and the 10-layer SPVIGs, respectively. On the other hand, a transparency peak appears at $\Delta k = 0$ when N is an even integer, whereas this is not the case when N is an odd integer. This is because the total phase-shift induced by the buffer layers of the SPVIGs is $(N-1) \times 2k_0 d = (N-1) \times (2m+1)\pi$.

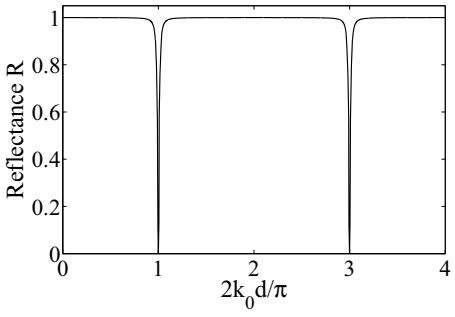

Fig. 5. The periodical transparency peaks at the Bragg-matched wavelength $\lambda_0 = 1.55\ \mu$m with the variation of the phase-shift $2k_0d$ induced by the buffer layer in a 2-layer SPVIG, where $n_0 = 1.55$, D = 3 mm, $\Lambda = 0.5\ \mu$m and $n_1 = 4 \times 10^{-4}$, respectively.

An even integer N will result in a destructive interference, whereas an odd integer N leads to a constructive interference. It is evident that the coupled mode solution provides a clear physical insight into the formation of the band structure of the reflectance spectra.

The positions of the transparency peaks can be controlled by adjusting the phase-shift induced by the buffer layer. Figure 4 shows the possibility to shift the transparency wavelength by controlling the thickness of the buffer layer in a 2-layer SPVIG. The transparency wavelength is blue-shifted with an increase in the thickness of the buffer layer, while it is red-shifted with a decrease in the buffer layer thickness. On the other hand, at the Bragg-matched wavelength λ_0 the transparency peak appears periodically as a function of the phase-shift $2k_0d$ whenever the condition $2k_0d = (2m+1)\pi$ is satisfied, as is shown in Fig. 5. These properties can be applicable to addressable wavelength filters, wavelength division multiplexing and de-multiplexing, and switching.

5. Dispersion properties of the SPVIGs and group velocity control

It is well known that a periodical structure is highly dispersive [1, 2] and such a dispersive property can be used to control the group velocity v_g of light beams [9, 34-38]. Lin et al. [35] studied the dispersive property of a SG and demonstrated the possibility to control the group velocity of light through a SG recorded in an iron-doped lithium niobate crystal. The group velocity of a SG can be expressed as [35]

$$v_g = v_p \frac{(\Delta k/2)^2 - \kappa^2 \cosh^2(sD)}{(\Delta k/2)^2 - \kappa^2 \frac{\sinh(sD)}{sD} \cosh(sD)}, \tag{14}$$

where $v_p = c/n_0$ is the phase velocity of lights in the host medium in the absence of the volume index grating. A group index $n_g = c/v_g$ of 7.5 was obtained in a 3.5-cm lithium niobate crystal with a refractive index modulation of 2.1×10^{-5}.

We study the dispersive properties of the SPVIG and find that the dispersion of the SPVIG is greatly enhanced as compared to that of the SG. Therefore, the SPVIG offers a great feasibility to control the group velocity of lights to a large extent through the design of the SPVIGs. In the following, we take a 2-layer SPVIG as an example without loss of the generality to illustrate the enhanced dispersion effect and its application to the control of the group velocity of light. Through a lengthy but straightforward calculation (see appendix A), we obtain the phase shift

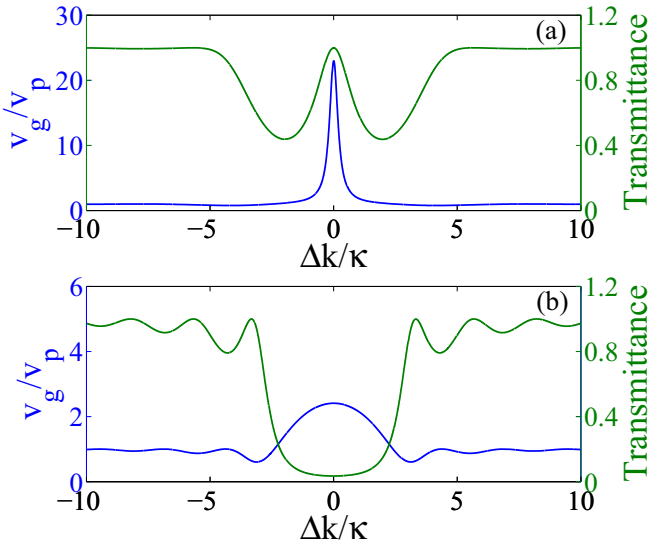

Fig. 6. The group velocity and the transmittance T of the light incident normally onto a 2-layer SPVIG (a) and a SG (b), respectively. The blue curves and the green curves are for the group velocity and the transmittance, respectively. The Bragg-matched wavelength is set to be 1.55 μm. The parameters for the 2-layer SPVIG are set to be $n_0 = 1.55$, D = 1.46 mm, d = 0.25 μm, $\Lambda = 0.5$ μm and $n_1 = 4\times10^{-4}$, respectively. The grating parameters for the SG are the same as those of the SPVIG, and the thickness of the SG is equal to 2D+d.

Φ of the transmitted light through a 2-layer SPVIG

$$\Phi = \frac{2\pi}{\Lambda}D + 2k_0 d + \arctan\left(\frac{\sinh^2(sD)\sin\varphi + \sin\gamma\cos\gamma\sinh(2sD)}{\sinh^2(sD)\cos\varphi + \sin^2\gamma\cosh^2(sD) - \cos^2\gamma\sinh^2(sD)}\right). \quad (15)$$

Where we set $\sin\gamma = s/\kappa$, $\cos\gamma = \Delta k/2\kappa$, and $\varphi = \Delta kD - 2k_0 d$ for convenience. The group velocity of lights through a 2-layer SPVIG can be obtained by differentiating the phase shift per unit length with respect to the angular frequency ω

$$v_g = (2D+d)\left(\frac{\partial\Phi}{\partial\omega}\right)^{-1}. \quad (16)$$

Figure 6 (a) shows the numerical results of the group velocity and the transmittance T of lights through a 2-layer SPVIG with $n_0 = 1.55$, D = 1.46 mm, d = 0.25 μm, $\Lambda = 0.5$ μm and $n_1 = 4\times10^{-4}$, respectively. For comparison, the group velocity and the transmittance of a SG with $n_0 = 1.55$, a thickness of 2D + d, $\Lambda = 0.5$ μm and $n_1 = 4\times10^{-4}$ are also shown in Fig. 6 (b). Note that we neglect the dispersion of the refractive index n_0 in the calculation because what we consider here is the dispersion induced by the structure of the refractive index distribution instead of the refractive index of the material itself. This is reasonable for most optical materials such as photorefractive lithium niobate crystals and optical fibers without involvement of the nonlinear effects. It is seen that superluminal light propagation is demonstrated at/near the Bragg-matched wavelength in both cases, while the group velocity in the 2-layer SPVIG case is faster by a factor of $\sim$10 as compared to that in the SG case. Moreover, the transmittance of the superluminal lights in the 2-layer SPVIG case is larger than 80%, whereas that in the

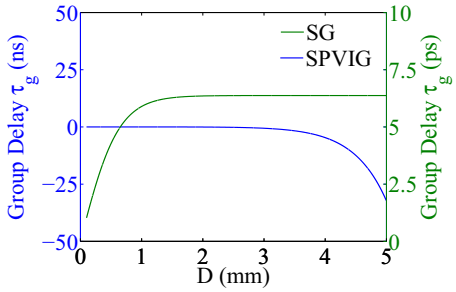

Fig. 7. The group delays τ_g of a 2-layer SPVIG (blue curve) and a SG (green curve) versus the variation of D. The wavelength is set at Bragg-matched and is at 1.55 μm. The parameters for the 2-layer SPVIG are set to be $n_0 = 1.55$, d = 0.25 μm, $\Lambda = 0.5$ μm and $n_1 = 4 \times 10^{-4}$, respectively. The thickness of the SG is equal to 2D+d.

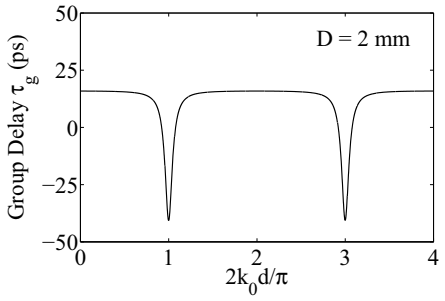

Fig. 8. The group delay τ_g of a 2-layer SPVIG versus the phase variation $2k_0d$ induced by the buffer layer. The wavelength is set to be Bragg-matched at 1.55 μm. The parameters for the 2-layer SPVIG are set to be $n_0 = 1.55$, D = 2 mm, $\Lambda = 0.5$ μm and $n_1 = 4 \times 10^{-4}$, respectively.

SG case is less than 5% due to the Bragg-reflection effect. Figure 7 shows the group delay τ_g (defined as $\tau_g = L/v_g$, where L is the total thickness of the SPVIG or the SG) as a function of the thickness D for the 2-layer SPVIGs and the SGs at the Bragg-matched wavelength $\lambda_0 = 1.55$ μm. The parameters for n_0, d, Λ and n_1 are set to be 1.55, 0.25 μm, 0.5 μm and 4×10^{-4}, respectively. The thickness of the SG is $L = 2D + d$. It is seen that the group delay in the SG case increases first but then tends to be saturated with the increase of D. The group delay in the 2-layer SPVIG case varies first slowly but then becomes negative and decreases rapidly with the increase of D. A negative group delay of $\sim$ 30 ns is possible with D = 5 mm. This is because the transparency peak becomes sharper and sharper; therefore, the dispersion slope becomes steeper and steeper with increasing D in the 2-layer SPVIG case. Note that the time scale for the SPVIG is nano-second while that for the SG is pico-second in Fig. 7. Figure 8 illustrates the control of the group delay through the phase variation $2k_0d$ induced by the buffer layer. The parameters for the SPVIG is $n_0 = 1.55$, D = 2 mm, $\Lambda = 0.5$ μm, and $n_1 = 4 \times 10^{-4}$, respectively. The operating wavelength is set to be Bragg-matched at 1.55 μm. We see that, whenever the condition $2k_0d = (2m+1)\pi$ is satisfied which corresponds to the appearance of the transparency peak at the Bragg-matched wavelength, a sharp increase in the group delay is observed. These results clearly illustrate the versatility and the effectiveness of the SPVIG on the control of the group velocity of light through the design of its structure parameters. Experiments on group velocity control through a 2-layer SPVIG by using a photorefractive lithium niobate crystal are currently going on in our laboratory. The photosensitive optical fiber could be an additional good material candidate to fabricate the stratified and phase-shifted volume index gratings.

6. Conclusion

In conclusion, we have obtained the recursion formula for the reflectance of the SPVIGs and studied the spectral characteristics of the SPVIGs based on the recursion formula. Transparency peaks appear within the stop-band of the volume index grating due to the interleave of the homogeneous buffer layers in the SPVIG. The spectral positions of the transparency peaks can be controlled through the phase-shift induced by the buffer layer. The dispersion slope is found to be very steep at/near the transparency peaks in the SPVIG and it can be used to control the group velocity of light to a large extent. The group delay experienced by the light through the SPVIG can be controlled by adjusting the phase shift induced by the buffer layer. Negative group delay in the order of tens of nano-seconds with high transmittance is possible with a centimeter-length SPVIG. Such properties can be applicable to addressable filter, wavelength division multiplexer and de-multiplexer, switching, and controllable optical delay/advance line. As compared to the SG, the SPVIG offers more feasibility and versatility to modify the spectral response and to control the group velocity.

Acknowledgments

This work is financially supported by the Key Project of Chinese Ministry of Education under grant 104054, the National Natural Science Foundation of China (grants 60308005, 60678021 and 10334010), the Program for New Century Excellent Talents in University under grant NCET-04-0234, the Program for Changjiang Scholars and Innovative Research Team in University, the Cultivation Fund of the Key Scientific and Technical Innovation Project, Ministry of Education of China under grant 704012, the Municipal International Cooperation Program of Tianjin under grant 06YFGHHZ00500, the National Basic Research Program of China under grant 2007CB307002, and CNKBRSF under grant 2006CB921703.

Appendix

A. Derivation of the phase shift Φ of the transmitted light through a 2-layer SPVIG

The amplitude of the electric field $E_2(x)$ in the second grating layer is the summation of the forward and the backward propagation waves

$$E_2(x) = A_2(x)e^{ik_0(x-(D+d))} + B_2(x)e^{-ik_0(x-(D+d))}, \tag{17}$$

where $A_2(x)$ is

$$A_2(x) = (A_2(D+d)\cosh(s(x-(D+d))) + C_2\sinh(s(x-(D+d))))\, e^{-i\Delta k(x-(D+d))/2}, \tag{18}$$

and $B_2(x)$ satisfies

$$B_2(x) = -\frac{i}{\kappa}e^{i\Delta k(x-(D+d))}\frac{\partial A_2(x)}{\partial(x)}. \tag{19}$$

By combining the boundary conditions expressed by Eqs. (8) and (9), we obtain

$$C_2 = \frac{1}{s}\left(i\kappa B_1(D)e^{-ik_0 d} + i\frac{\Delta k}{2}A_1(D)e^{ik_0 d}\right). \tag{20}$$

Where $A_1(D)$ and $B_1(D)$ can be obtained by substituting Eqs. (7) and (10) into Eqs. (5) and (6) under the boundary condition $B_2(2D+d) = 0$. The amplitude $E_2(2D+d)$ is then expressed as

$$E_2(2D+d) = A_2(2D+d)e^{ik_0 D}, \tag{21}$$

where $A_2(2D+d)$ is

$$A_2(2D+d) = \frac{s^2}{\kappa^2}\frac{A_1(0)}{ARe - iAIm}e^{ik_0 d}e^{-i\Delta kD}, \tag{22}$$

with the parameters ARe and AIm being

$$ARe = \sinh^2(sD)\cos\varphi + \sin^2\gamma\cosh^2(sD) - \cos^2\gamma\sinh^2(sD) \tag{23}$$

and

$$AIm = \sinh^2(sD)\sin\varphi + \cos\gamma\sin\gamma\sinh(2sD), \tag{24}$$

respectively. By taking account of the propagation phase shift $k_0(D+d)$ induced by the first grating layer and the buffer layer, we obtain the phase shift Φ of the transmitted light through a 2-layer SPVIG shown by Eq. (15).

Nonlinear ellipse rotation modified Z-scan measurements of third-order nonlinear susceptibility tensor

Zhi-Bo Liu, Xiao-Qing Yan, Jian-Guo Tian,* Wen-Yuan Zhou, and Wei-Ping Zang

Key Laboratory of Weak Light Nonlinear Photonics, Ministry of Education, Teda Applied Physics School, Nankai University, Tianjin 300457, China
**Corresponding author: jjtian@nankai.edu.cn*

Abstract: We present a method that combines the Z-scan technique with nonlinear ellipse rotation (NER) to measure third-order nonlinear susceptibility components. The experimental details are demonstrated, and a comprehensive theoretical analysis is given. The validity of this method is verified by the measurements of the nonlinear susceptibility tensor of a well-characterized liquid, CS_2.

OCIS codes: (190.0190) Nonlinear optics; (190.3270) Kerr effect; (190.4710) Optical nonlinearities in organic materials.

References and links

1. R. L. Sutherland, ed., *Handbook of Nonlinear Optics* (Marcel Dekker, New York, 1996).
2. S. R. Friberg and P. W. Smith, "Nonlinear optical glasses for ultrafast optical switches," IEEE J. Quantum Electron. **QE-23**, 2089–2094 (1987).
3. G. Boudebs, M. Chis, and J. P. Bourdin, "Third-order susceptibility measurements by nonlinear image processing," J. Opt. Soc. Am. B **13**, 1450–1456 (1996).
4. P. D. Maker, R. W. Terhune, and C. M. Savage, "Intensity-dependent changes in the refractive index of liquids," Phys. Rev. Lett. **12**, 507–509 (1964).
5. P. D. Maker and R. W. Terhune, "Study of optical effects due to an induced polarization third order in the electric field strength," Phys. Rev. **137**, A801–A818 (1965).
6. M. Sheik-Bahae, A. A. Said, T. H. Vei, D. J. Hagan, and E. W. Van Stryland, "Sensitive measurement of optical nonlinearities using a single beam," IEEE J. Quantum Electron. **26**, 760–769 (1990).
7. W. Zhao and P. Palffy-Muhoray, "Z-scan technique using top-hat beams," Appl. Phys. Lett. **63**, 1613–1615 (1993).
8. T. Xia, D. J. Hagan, M. Sheik-Bahae, and E. W. Van Stryland, "Eclipsing Z-scan measurement of Lambda/104 wave-front distortion," Opt. Lett. **19**, 317–319 (1994).
9. R. W. Boyd, *Nonlinear Optics*, 2nd ed. (Academic Press, San Diego, 2003).
10. A. J. Van Wonderen, "Influence of transverse effects on self-induced polarization changes in an isotropic Kerr medium," J. Opt. Soc. Am. B **14**, 1118–1130 (1997).
11. M. Lefkir and G. Rivoire, "Influence of transverse effects on measurements of third-order nonlinear susceptibility by self-induced polarization state changes," J. Opt. Soc. Am. B **14**, 2856–2864 (1997).
12. M. Sheik-Bahae and M. P. Hasselbeck, "Third-order optical nonlinearities," in *OSA Handbook of Optics*, (McGraw-Hill 2001), Vol. IV, Chap. 17.

1. Introduction

A variety of experimental methods are used for measurements of third-order nonlinear susceptibility, such as four-wave mixing [1,2], nonlinear imaging techniques [3], nonlinear ellipse rotation (NER) [4,5], and Z-scan [6-8]. Among these methods, NER and Z-scan use only one optical wave and measure either spatial profile changes or polarization changes of the wave. The NER method permits the determination of the nonlinear susceptibility component $\chi^{(3)}_{xyyx}$, and its history goes back to the classic work of Maker *et al.* [4]. The Z-scan method has been employed extensively because of its simplicity, sensitivity, accuracy, and the ease of separation of nonlinear refraction (NLR) and nonlinear absorption (NLA). However, it

is practically impossible for any single technique or method to unambiguously separate the different nonlinearities at once. Every technique or method has advantages and disadvantages. For example, degenerate four-wave mixing (DFWM) can measure different tensor components of $\chi^{(3)}$ in a single experimental setup for isotropic materials. It is not necessary for the beams employed in the experiment to be perfect TEM_{00} Gaussian modes as long as they are well-characterized. The time dependence of the nonlinearity can be studied readily. However, the disadvantages of this technique include the fact that only the modulus of $\chi^{(3)}$ (*i.e.*, $\left|\chi^{(3)}\right|$) can generally be measured. A far more complicated experimental apparatus is needed; in general, the technique must be supplemented with another measurement to extract the real and imaginary parts of $\chi^{(3)}$. Hence, different measurements are usually required to unravel the underlying physical mechanism by varying parameters such as irradiance and polarization state, or even the use of different measurement methods [1].

For an isotropic medium, the third-order susceptibility tensor has three independent components, $\chi^{(3)}_{xxyy}$, $\chi^{(3)}_{xyxy}$, and $\chi^{(3)}_{xyyx}$ [9], which have not been taken into account in Z-scan measurements as yet. NER and other nonlinear polarization dynamics are owing to the existence of $\chi^{(3)}_{xyyx}$. Moreover, polarization-dependent NLR can be observed in the isotropic medium based on the effect of $\chi^{(3)}_{xyyx}$ [9]. Therefore, it is expected that different tensor components of $\chi^{(3)}$ can be obtained by Z-scan measurements using linearly, circularly, and elliptically polarized light. In this work, the polarization dependence of NLR in CS_2 is studied. This molecule has been studied thoroughly in NER and presents large molecular reorientation nonlinearities in the subnanosecond regime. We combine the Z-scan technique and NER to carry out a sensitive and simple measurement of $\chi^{(3)}_{xyyx}$. The theoretical analysis is made and the obtained transmittance formulae allow direct estimation of the component $\chi^{(3)}_{xyyx}$.

2. NER modified Z-scan technique

In Z-scan measurements, the sample is moved along the propagation direction (*z*-axis) of a tightly focused beam, and the variation of the far-field intensity is used to determine the NLR. Although Z-scan has the simplicity of both experimental setup and data analysis, a high-quality Gaussian TEM_{00} beam for absolute measurements is required. Sample distortions or wedges, or a tilting of the sample during translation, can cause the beam to walk off the far-field aperture. This produces unwanted fluctuations in the detected signal. Even if these are kept under control, beam jitter will produce the same effect. The technique cannot be used to measure off-diagonal elements of the susceptibility tensor except when a second nondegenerate frequency beam is employed.

Another widely used technique, NER, is a single-beam experiment also using an elliptically polarized wave. A linearly polarized wave is incident on a quarter-wave plate, with its direction of polarization making an angle α with respect to the slow axis of the wave plate. This creates an elliptically polarized beam with left-circularly and right-circularly polarized components E_+ and E_-, respectively. Without NLA or scattering, when the elliptically polarized beam propagates through the nonlinear medium, the orientation of the polarization ellipse will rotate an angle θ as a function of input intensity under a given sample length *d*. The beam going through the nonlinear medium passes through the second quarter-wave plate oriented crosswise to the first and then a polarizer oriented for extinction of the beam in the absence of the nonlinear sample. NER can determine only one component $\chi^{(3)}_{xyyx}$, but not the total third-order nonlinear susceptibility $\chi^{(3)}$.

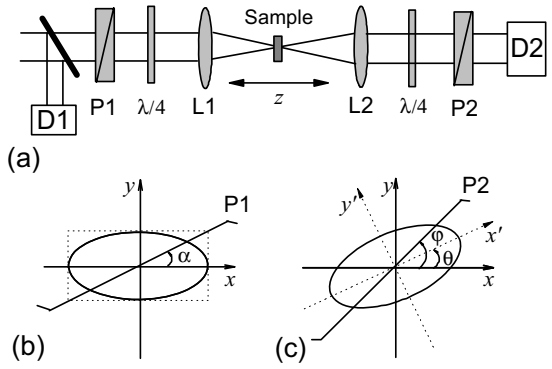

Fig. 1. (a) Experimental arrangement for NER modified Z-scan. D1 and D2 are the detectors. (b) and (c) are the geometry of incident and the transmitted polarization ellipse, respectively. The slow axis of the first λ/4 plate is taken along the *x*-axis. α is the angle between the first polarizer direction and the *x*-axis. θ is the rotating angle of the polarization ellipse induced by nonlinearity. φ is the angle of the analyzer.

Since the rotation angle θ of the polarization ellipse depends upon the intensity of the input beam, the tight-focus geometry in Z-scan can be also used in NER. It is possible to combine the advantages of Z-scan and NER to measure the component $\chi^{(3)}_{xyyx}$ simply and sensitively. Figure 1(a) gives the configuration of the NER modified Z-scan method, which is the same as that of an open-aperture Z-scan except that two paralleled polarizers and two crossed quarter-wave plates are used. When the sample is far away from focus, the beam irradiance is low and NLR is negligible; the polarization state remains unchanged for incident and transmitted beams. Hence, all of the transmitted irradiance through the sample is collected into detector D2, and the transmittance [D2/D1, in Fig. 1(a)] remains relatively constant. As the sample is brought closer into focus, the beam irradiance increases, thus leading to the rotation of the polarization ellipse. The rotation of the polarization ellipse permits only part of the transmitted irradiance to pass the second polarizer, and a decrease in the measured transmittance occurs. Such Z-scan traces with NER are expected to be symmetric with respect to the focus ($z = 0$); they have minimum transmittance at focus. The coefficient of $\chi^{(3)}_{xyyx}$ can be calculated easily from such transmittance.

3. Theory

Let us consider a linearly polarized beam propagating along the *z*-axis. The electric field can be written as $E_{lin} = E_0(r,z)\exp[i(kz-\omega t)]$, where $k = n\omega/c$ is the wave vector, ω is the frequency of light, and *n* is the linear refractive index of the medium. We assume a stationary regime, and thus the amplitude $E_0(r,z)$ does not depend on the time *t*. When the linearly polarized beam passes the λ/4 plate with angle α [with $-\pi/2 \le \alpha \le \pi/2$ being the angle between the linear polarization direction and the λ/4 plate slow axis—see Fig. 1(b)], it can be converted into an elliptically polarized beam. The electric field *E* of such an elliptically polarized beam can always be decomposed into a linear combination of the *x*- and *y*-direction components (E_x and E_y), or left- and right-hand circular components (E_+ and E_-) with the unitary transformation $E_+ = (E_x - iE_y)/\sqrt{2}$ and $E_- = (E_x + iE_y)/\sqrt{2}$. If we define the λ/4 plate slow axis as the *x*-axis, the electric field of *x*- and *y*-direction components can be written as

$$E_x = E_0 \cos\alpha \exp[i(kz-\omega t)], \tag{1a}$$

$$E_y = E_0 \sin\alpha \exp\left[i(kz - \omega t + \Delta)\right], \tag{1b}$$

where Δ is the phase retardation. $\Delta = \pi/2$ for the λ/4 plate.

For the choice of frequencies given by $\chi^{(3)}_{ijkl}(\omega = \omega + \omega - \omega)$, the condition of intrinsic permutation symmetry requires that $\chi^{(3)}_{xxyy}$ be equal to $\chi^{(3)}_{xyxy}$. Hence, there are only two independent elements of the susceptibility tensor describing the NLR of an isotropic medium. Following the notation of Maker *et al.* [4], the nonlinear polarization $\mathbf{P}^{\mathrm{NL}}$ can be written as

$$\mathbf{P}^{\mathrm{NL}} = A(\mathbf{E}\bullet\mathbf{E}^*)\mathbf{E} + \frac{1}{2}B(\mathbf{E}\bullet\mathbf{E})\mathbf{E}^*, \tag{2}$$

where $A = 6\chi^{(3)}_{xxyy}$ and $B = 6\chi^{(3)}_{xyyx}$. Hence, the total refractive indexes of two circular components is given by [9]

$$n_{\pm} = n_0 + \frac{2\pi}{n_0}\left[A\left|E_{\pm}\right|^2 + (A+B)\left|E_{\mp}\right|^2\right]. \tag{3}$$

We see from Eq. (3) that the change in refractive index $\delta n_{\pm}$ is different for two circular components and depends upon ellipticity e, where $e = \left\|E_+\right| - \left|E_-\right\| / \left(\left|E_+\right| + \left|E_-\right|\right)$. First, we consider two specific cases. One case is for a circularly polarized beam with $e = 1$; this means that only one of two circular components is present. Thus, the change of the refractive index can be given by $\delta n = (2\pi/n_0)A\left|E\right|^2$, which clearly depends on A but not B. The NLR coefficient n_2 of the total beam should reach a minimum in this case. Another case is for a linearly polarized beam. Since a linearly polarized beam is a combination of equal amounts of left- and right-hand circular components (i.e. $\left|E\right|^2 = 2\left|E_+\right|^2 = 2\left|E_-\right|^2$), the change of the refractive index can be given by $\delta n = (2\pi/n_0)(A + B/2)\left|E\right|^2$, and n_2 reaches a maximum. For the case of arbitrary ellipticity, n_2 can be written as

$$n_2 = \frac{(1-q^2)n_{2cir} + 2qn_{2lin}}{1+q^2}, \tag{4}$$

where $q = (1-e)/(1+e)$, and n_{2cir} and n_{2lin} are the NLR coefficients in the case of circularly and linearly polarized beams, respectively.

We can see from Eq. (3) that the left- and right-hand circular components of the beam propagate with different phase velocities because of different $\delta n_{\pm}$ and cause the rotation of the polarization ellipse of the transmitted wave [see Fig. 1(c)]. The angle of rotation can be written as

$$\theta = \frac{1}{2}(n_+ - n_-)\frac{\omega}{c}d = \frac{\pi\omega}{cn}\left(\left|E_-\right|^2 - \left|E_+\right|^2\right)d = QE_0^2, \tag{5}$$

where $Q = -(2\pi\omega/cn)Bd\sin\alpha\cos\alpha$ and d is the sample length. In new $x'-y'$ coordinates taken along the major and minor axes of the ellipse, we can write the electric field E as

$$\mathbf{E}_{(x'-y')} = E_0\left(\cos\alpha\hat{x}' + i\sin\alpha\hat{y}'\right)\exp\left[i(kz - \omega t)\right], \tag{6}$$

where $\hat{x}'$ and $\hat{y}'$ are the polarization unit vectors in the new coordinates system with $\hat{x}' = \hat{x}\cos\theta - \hat{y}\sin\theta$ and $\hat{y}' = \hat{x}\sin\theta + \hat{y}\cos\theta$. Therefore, by transforming the electric field vector from $x'-y'$ coordinates to $x-y$ coordinates, **E** can be written as

$$\mathbf{E} = E_0\left[\left(\cos\alpha\cos\theta - i\sin\alpha\sin\theta\right)\hat{x} + \left(\cos\alpha\sin\theta + i\sin\alpha\cos\theta\right)\hat{y}\right]\exp\left[i\left(kz-\omega t\right)\right]. \quad (7)$$

The output beam is then directed to another λ/4 plate crossing to the input λ/4 plate. Its phase retardation is Δ. If the orientation of the analyzer (second polarizer) has an angle of φ ($-\pi/2 \le \varphi \le \pi/2$) relative to the *x*-axis, the output electric field $\mathbf{E}_{out}$ through the analyzer can be written as

$$\begin{aligned}\mathbf{E}_{out} = E_0\left[\left(\cos\alpha\cos\theta - i\sin\alpha\sin\theta\right)\left(\cos\Delta + i\sin\Delta\right)\cos\varphi + \right.\\ \left.\left(\cos\alpha\sin\theta + i\sin\alpha\cos\theta\right)\sin\varphi\right]\exp\left[i\left(kz-\omega t\right)\right]\end{aligned}. \quad (8)$$

Assuming a TEM_{00} Gaussian beam of beam waist radius w_0 traveling in the +*z* direction, we can write the input *E* as

$$E_0(r,z) = E_{00}\frac{w_0}{w_z}\exp\left[-\frac{r^2}{w_z^2} - \frac{ikr^2}{2R_z}\right], \quad (9)$$

where E_{00} is the on-axis electric field at focus, $w_z^2 = w_0^2\left(1+z^2/z_0^2\right)$ is the beam radius, $R_z = z\left(1+z_0^2/z^2\right)$ is the radius of curvature of the wavefront at *z*, and $z_0 = kw_0^2/2$ is the diffraction length of the beam. For the spatial Gaussian beam, the influence of transverse effects on self-induced polarization changes must be considered [10,11]. Hence, the transmitted power through the analyzer is obtained by spatially integrating $\mathbf{E}_{out}$ up to infinity:

$$P(z) = \varepsilon_0 n_0 c\pi\int_0^{+\infty}\left|E_{out}\right|^2 r\mathrm{d}r. \quad (10)$$

Substituting Eqs. (8) and (9) into Eq. (10) and completing the spatial integration, we can obtain an expression of transmitted power as a function of *z* as follows:

$$\begin{aligned}P_{non}(z) = \frac{\varepsilon_0 n_0 c\pi w_z^2}{8Q}\left\{\frac{1}{2}\cos 2\alpha\left[\sin(2QP)\cos 2\varphi - \cos(2QP)\sin 2\varphi\cos\Delta\right.\right.\\ \left.\left. + \sin 2\varphi\cos\Delta\right] + QP\left(1+\sin 2\alpha\sin 2\varphi\sin\Delta\right)\right\}\end{aligned}, \quad (11)$$

where ε_0 is the permittivity of vacuum and $P = E_{00}^2 w_0^2/w_z^2$. In the case of linear propagation (*i.e.*, $\theta = 0$), the transmitted power can be written as

$$P_{lin} = \frac{\varepsilon_0 n_0 c\pi E_{00}^2 w_0^2}{4}\left(\sin^2\alpha\sin^2\varphi + \cos^2\alpha\cos^2\varphi + \frac{1}{2}\sin 2\alpha\sin 2\varphi\sin\Delta\right). \quad (12)$$

The normalized Z-scan transmittance can be calculated by

$$T(z) = \frac{P_{non}(z)}{P_{lin}}. \quad (13)$$

We first consider the case in which the analyzer is set parallel to the first polarizer, and meanwhile the second λ/4 plate exists, *i.e.*, $\alpha = \varphi$ and $\Delta = \pi/2$. The normalized transmittance $T(z)$ can be written as

$$T(z)=\frac{1+\sin^2 2\alpha}{2}+\frac{\cos^2 2\alpha}{4QP}\sin(2QP)\,. \tag{14}$$

Another case is where the second λ/4 plate is removed, and the sensitivity of the Z-scan measurement is enhanced as analyzed below. The removal of the second λ/4 plate makes $\Delta=0$. Hence, $T(z)$ can be written as

$$T(z)=\frac{R}{2}+\frac{\sin 2\varphi+\sin 2(QP-\varphi)}{4QP}R\cos 2\alpha\,, \tag{15}$$

where $R=1/(\sin^2\alpha\sin^2\varphi+\cos^2\alpha\cos^2\varphi)$.

Now we can easily extend the steady-state results to the transient effects induced by pulsed radiation by using the time-averaged rotation angle $\langle\theta(t)\rangle$:

$$\langle\theta(t)\rangle=\frac{\int_{-\infty}^{\infty}\theta|E_0(t)|^2\,\mathrm{d}t}{\int_{-\infty}^{\infty}|E_0(t)|^2\,\mathrm{d}t}\,. \tag{16}$$

For a nonlinearity having instantaneous response, we obtain for a temporally Gaussian pulse

$$\langle\theta(t)\rangle=\frac{\theta}{\sqrt{2}}\,. \tag{17}$$

4. Experimental results and discussions

Our experiments are carried out on an isotropic nonlinear medium, CS_2. This molecule has been studied extensively by many experimental methods and now is widely used as a reference sample. As the nonlinearities of CS_2 mainly rely on the molecular reorientation effect in the subnanosecond regime, the high ratio of B to A attains 6 [9] and the NLR coefficient $n_2=3.4\times10^{-18}$ m^2/W for linearly polarized light [6,7]. In our experiments, a mode-locked Nd:YAG laser (Continuum Model PY61) was used to generate 30 ps pulses at 532 nm with a repetition rate of 10 Hz. The pulse laser focused by a lens to form a beam waist w_0 of 22 μm was incident to a 1 mm cell containing CS_2. The on-axis peak intensity I_0 was 5.93 GW/cm^2. To keep the intensities of input beams fixed for different polarization states, linear, elliptical, and circular polarizations were realized by altering only the angle between the first polarizer and the λ/4 plate with $\alpha=0$, $\alpha=-22.5^\circ$, and $\alpha=-45^\circ$, *i.e.*, the ellipticity $e=0$, $e=0.4142$, and $e=1$, respectively. The negative sign of α implies that the beam is a left-handed elliptical polarization after passing through the λ/4 plate.

First, we examined the dependence of NLR on the polarization ellipse. Figure 2 gives the normalized transmittance of NLR for linear, circular, and elliptical polarization obtained by a traditional closed aperture Z-scan in which an aperture was used instead of the second λ/4 plate and the analyzer in Fig. 1(a). Among those, the NLR is largest for an elliptically polarized beam and smallest for a circularly polarized beam. The values of n_2, fitted by using the theoretical model of Ref.[6], are 3.0×10^{-18}, 1.6×10^{-18}, and 0.78×10^{-18} m^2/W for linear, circular, and elliptical polarization, respectively. From Eq. (3), one can get the ratio of n_{2lin} to n_{2cir} to be $1+B/2A$. For molecular reorientation nonlinearities, $n_{2lin}/n_{2cir}=4$ owing to $B/A=6$. It is obvious that $n_{2lin}/n_{2cir}=3.8$ obtained experimentally agrees well with the theoretical one. Note that the change of NLR for different polarization states depends upon B but not A. It is identical to NER in which the rotation of the elliptical axis is caused only by B.

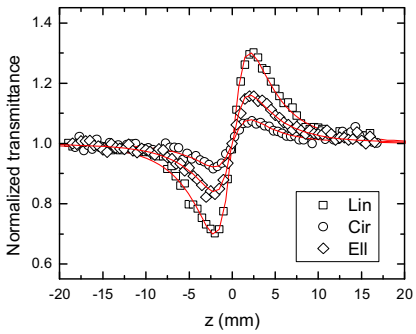

Fig. 2. Z-scan curves for linear, circular, and elliptical polarization obtained by traditional closed aperture Z-scan.

The real part of third-order nonlinear susceptibility $\chi^{(3)}$ is related to the NLR coefficient n_2 through [12]

$$\mathrm{Re}\left(\chi^{(3)}\right)=\frac{4\varepsilon_0 n_0^2 c}{3}n_2 . \tag{18}$$

Therefore, from the results of the Z-scan with a circularly polarized light, we can obtain $A = 2.16\times10^{-20}\mathrm{m}^2/\mathrm{V}^2$, since the changes of refractive index and absorption only depend on A in the case of circular polarization. And then, B can be determined to be $12.8\times10^{-20}\mathrm{m}^2/\mathrm{V}^2$ by the Z-scan experimental results of linear polarization or elliptical polarization, which is 5.9 times as large as that of A. Therefore, B/A is closer to that of theoretical analysis.

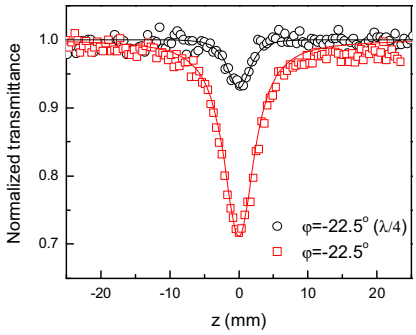

Fig. 3. Z-scan curves of NER modified Z-scan with and without the second λ/4 plate. The polarization directions of the polarizer and the analyzer parallel each other ($\alpha=\varphi=-22.5^\circ$). The solid lines are the theoretical fittings with $B=12.6\times10^{-20}\mathrm{m}^2/\mathrm{V}^2$ and $I_0 = 5.93\ \mathrm{GW/cm}^2$.

To measure the coefficient B directly, we used the experimental setup combining Z-scan and NER as shown in Fig. 1(a), and two paralleled polarizers and two crossed quarter-wave plates were additionally used. The circular symbols in Fig. 3 represent the experimental results of the Z-scan. Using Eq. (14) to fit the experimental data, we obtain coefficient B to be $12.6\times10^{-20}\mathrm{m}^2/\mathrm{V}^2$, which is identical to the results of closed aperture Z-scan measurements within errors. If the second λ/4 plate is removed and other experimental conditions are kept

unchanged, the transmittance change of the polarization ellipse through the analyzer due to the rotation of axis position can be observed directly. The valley of the Z-scan curve has a larger magnitude than that with the second λ/4 plate, indicating that the removal of a λ/4 plate can enhance the sensitivity of Z-scan measurements.

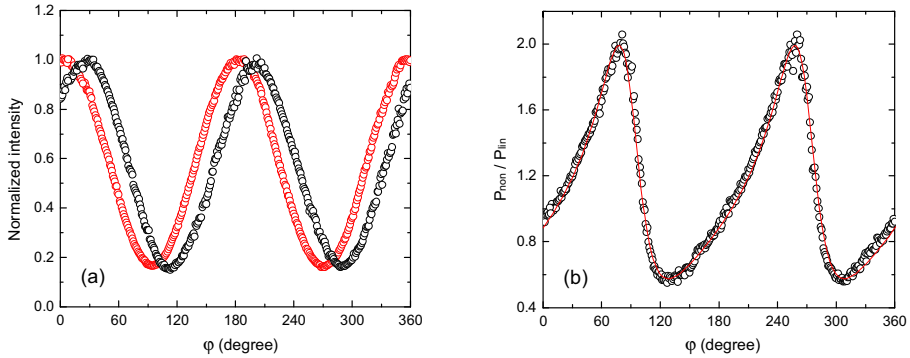

Fig. 4. (a) Normalized transmitted power through the analyzer at linear output and nonlinear output obtained by rotating the analyzer. (b) The ratio of nonlinear transmitted power to linear transmitted power as a function of rotation angle of the analyzer.

Using the experimental setup without the second λ/4 plate and fixing the sample on focus, the information of the ellipse axis and ellipticity e can be obtained by measuring the transmitted power as the analyzer rotates. The normalized transmitted power as a function of φ are shown in Fig. 4(a) for linear output at low input power ($I_0 < 10^6\,\mathrm{W/cm^2}$) and nonlinear output at high input power ($I_0 = 5.93\mathrm{GW/cm^2}$). A 19° rotation of the polarization ellipse at nonlinear output relative to that of linear output can be observed, while no obvious change of ellipticity occurs. Figure 4(b) gives the ratio of transmitted power at nonlinear output to that of linear output. The solid line is the theoretical fit with $B = 12.6\times10^{-20}\,\mathrm{m^2/V^2}$, which is easily obtained by assuming $z = 0$ in Eq. (15). In other words, the ratio in Fig. 4(b) also shows the valley change of the NER-modified Z-scan without the second λ/4 plate as the analyzer rotates. Therefore, if we change the orientation of the analyzer φ, Z-scan curves will give different profiles as shown in Fig. 5. First, $\varphi = 90^\circ$ means that the analyzer is along the minor axis of the polarization ellipse; hence, the rotation of the polarization ellipse causes the increase of transmitted power through the analyzer, and the Z-scan curve exhibits a peak structure as shown in Fig. 5(a). For $\varphi = 80^\circ$ and 76°, the normalized transmittance first decreases and then increases as the sample moves toward focus [see Figs. 5(b) and 5(c)]. The decrease of normalized transmittance is caused by the relative rotation of the analyzer to the minor axis of the polarization ellipse and is terminated while the analyzer is along the minor axis. Thereafter, the polarization ellipse continues to rotate as the sample moves continually, since the maximum rotation angle of polarization ellipse attains 19° ($80^\circ + 19^\circ = 99^\circ$ and $76^\circ + 19^\circ = 95^\circ$ are larger than 90°). Therefore, after the analyzer reaches the minor axis, the analyzer will be away from the minor axis as the input intensity further increases, leading to the increase of transmittance. In the case of $\varphi = 55^\circ$ ($55^\circ + 19^\circ < 90^\circ$), the Z-scan curve exhibits a valley structure as shown in Fig. 5(d), since the analyzer rotates towards but does not reach the minor axis of the polarization ellipse.

As mentioned above, although the nonlinear coefficient measured by the NER modified Z-scan is a real part of the nonlinear susceptibility component $\chi^{(3)}_{xyyx}$, the curves of the NER modified Z-scan are similar to those of an open-aperture Z-scan with multiphoton absorption

or saturable absorption. Furthermore, the experimental setup of the NER modified Z-scan is also similar to an open-aperture Z-scan and has less strict conditions on the beam profile than a closed-aperture Z-scan. This is because the nonlinear effect measured by an open-aperture Z-scan depends upon the amplitude change but not the phase distortion of the beam.

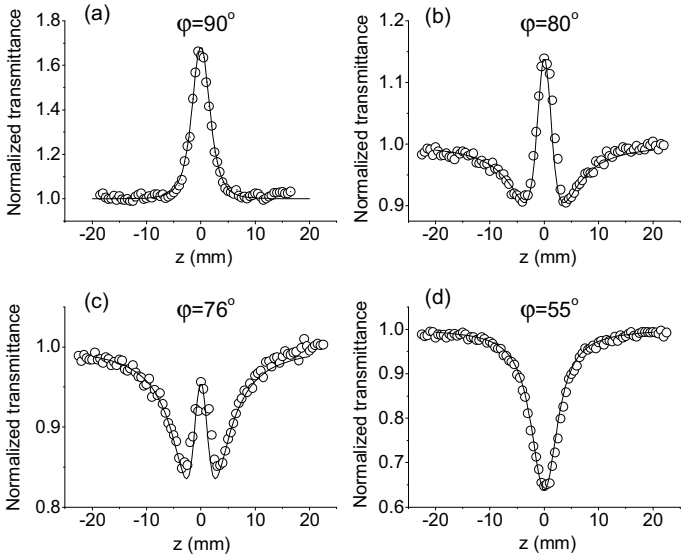

Fig. 5. Z-scan curves of NER modified Z-scan without second λ/4 plate at (a) $\varphi = 90^{\circ}$, (b) $\varphi = 80^{\circ}$, (c) $\varphi = 76^{\circ}$, and (d) $\varphi = 55^{\circ}$. The solid lines are the theoretical fittings with $B = 12.6 \times 10^{-20}\,\mathrm{m^2/V^2}$ and $I_0 = 5.93\ \mathrm{GW/cm^2}$.

5. Conclusion

We present here a method that combines the Z-scan technique with NER to study third-order nonlinear susceptibility tensor of isotropic media. It can obtain complete data on third-order susceptibility tensor properties of a material. Our results show that NLR is dependent on polarization ellipticity. It is expected that this method can be extended to anisotropic media.

Acknowledgments

This work is supported by the Natural Science Foundation of China grant 10574075, the Chinese National Key Basic Research Special Fund grant 2006CB921703, and the Preparatory Project of the National Key Fundamental Research Program grant 2004CCA04400.

#85608 - $15.00 USD Received 23 Jul 2007; revised 4 Sep 2007; accepted 4 Sep 2007; published 28 Sep 2007

Observation of dipole-like gap solitons in self-defocusing waveguide lattices

Liqin Tang,[1] Cibo Lou,[1] Xiaosheng Wang,[2] Daohong Song,[1] Xingyu Chen,[1] Jingjun Xu,[1] Zhigang Chen,[1,2,*] H. Susanto,[3] K. Law,[3] and P. G. Kevrekidis[3]

[1]*The Key Laboratory of Weak-Light Nonlinear Photonics, Ministry of Education and TEDA Applied Physical School, Nankai University, Tianjin 300457, China*
[2]*Department of Physics and Astronomy, San Francisco State University, San Francisco, California 94132, USA*
[3]*Department of Mathematics and Statistics, University of Massachusetts, Amherst, Massachusetts 01003, USA*
[*]*Corresponding author: zchen@stars.sfsu.edu*

Received June 6, 2007; revised July 20, 2007; accepted September 1, 2007;
posted September 11, 2007 (Doc. ID 83873); published October 9, 2007

We observe dipole-like gap solitons in two-dimensional waveguide lattices optically induced with a self-defocusing nonlinearity. Under appropriate conditions, two mutually coherent input beams excited in neighboring lattice sites evolve into a self-trapped state, whose spatial power spectrum and stability depend strongly on the initial excitation conditions. Our experimental observations are compared with numerical simulations. © 2007 Optical Society of America

OCIS codes: 190.0190, 190.5330, 250.5530.

Wave propagation in optical periodic structures is known to exhibit fundamental features particular to the presence of photonic bands and forbidden gaps. Under nonlinear propagation, an optical beam can self-trap to form a gap soliton (GS) with its propagation constant residing within a photonic bandgap, in contrast with conventional discrete solitons [1,2] formed in the semi-infinite gap due to total internal reflection. Spatial GSs [3] can arise from Bloch modes in the first band [close to high-symmetry M points, i.e., the edges of the first Brillouin zone (BZ)], where anomalous diffraction is counteracted by self-defocusing nonlinearity [4–6], or the second band (close to X points), where normal diffraction is balanced by self-focusing nonlinearity [7,8]. Recently, a new bound state of GS trains has been demonstrated without *a priori* spectral or phase engineering [9], suggesting that nonlinear spectrum reshaping can lead to energy transfer between regions initially excited and unexcited in the k-space (momentum space).

In this Letter, we report the experimental demonstration of dipole-like spatial GSs in a two-dimensional (2D) optically induced "backbone" lattice [4,9] with a saturable self-defocusing nonlinearity. Our experiments show that two mutually coherent dipole-like beams can evolve into a self-trapped state. The spatial power spectra and phase structures of these dipoles are dramatically different for linear and nonlinear propagation. Our theoretical analysis shows that the stability of these high-order solitons depends strongly on the initial excitation conditions (such as relative location and phase between the two beams).

The experimental setup for our study is similar to those used earlier for the creation of optically induced lattices [10,11]. A partially spatially incoherent beam (488 nm) is generated by using a rotating diffuser. A negatively biased photorefractive crystal (SBN:60 6 mm × 10 mm × 5 mm) is employed to provide a self-defocusing nonlinearity. To generate a 2D-waveguide lattice, we use an amplitude mask to spatially modulate the otherwise uniform beam after the diffuser. The lattice (spacing ~25 μm) beam is diagonally oriented and ordinarily polarized, thus the induced waveguide arrays remain invariant during propagation. A typical lattice intensity pattern, its spatial spectrum, and the dispersion curve for the first band are illustrated in Fig. 1. An extraordinarily polarized probe beam (intensity ~6 times weaker than that of the lattice beam) is sent into a Mach–Zehnder interferometer to create a dipole-like input pattern whose phase is controlled with the piezo-transducer (PZT) mirrors. Taking advantage of the photorefractive noninstantaneous response, we monitor the linear and nonlinear transport of the probe beam simply by recording its instantaneous (before nonlinear self-action) and steady-state (after self-action) output patterns/spectra.

Our motivation is to create multipole gap lattice solitons with a defocusing nonlinearity and to illustrate the similarities and differences in comparison with their counterparts in the focusing case [12]. In particular, we study dipole-like structures (with two peaks) excited at the intensity minima (index maxima) of the 2D "backbone" lattice. For the dipole-like structure, the two intensity peaks can be in phase (IP) or out of phase (OOP), and they can be located [see Fig. 1(a)] either in the two nearest wave-

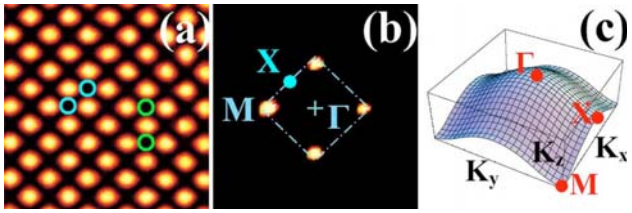

Fig. 1. (Color online) (a) Lattice pattern obtained from experiment with the two left (two right) circles marking the diagonal (vertical) excitation of the probe beam. (b) Fourier spectrum of (a) with dashed lines marking the first BZ. (c) Band structure for the first Bloch band.

guide sites (e.g., diagonal excitation along one direction of the principal axes) or in the two next nearest sites (e.g., vertical excitation along one diagonal direction of the square lattice).

First, we present our experimental results under diagonal excitation [see the two circles on the left in Fig. 1(a)]. Figure 2 shows the intensity patterns, Fourier spectra, and interferograms for both the IP case [Figs. 2(a) and 2(b)] and the OOP case [Figs. 2(c) and 2(d)]. In order to open the first gap in the defocusing lattice, a high-lattice potential is achieved by increasing the lattice intensity and the bias field (with the resulting index change for the lattice on the order of 10^{-4}). Under this lattice condition, we do not see a significant difference in intensity patterns between the linear [Figs. 2(a) and 2(c)] and nonlinear [Fig. 2(b) and 2(d)] cases simply because of the reduced coupling, although nonlinear trapping typically leads to longer "tails" for the dipole. However, remarkable differences can be seen in the spectrum and phase structure of the dipole "tails." Due to constructive phase relation, the linear spectrum of the IP dipole covers the first BZ with most of the power concentrating in the center [Fig. 2(a), middle]. Under a bias field of –1.1 kV/cm, however, the nonlinear spectrum reshapes and the energy transfers from the central region (normal diffraction) toward two lateral regions close to the two X points [where diffraction is anomalous along the y direction, as seen in Fig. 1(c)]. Because of the opposite dispersion/diffraction in two orthogonal directions at the X points in the first bandgap, the power spectrum in each side is elongated along the x direction, as the energy transfers further toward the regions close to M points where the diffraction is anomalous in both transverse directions. We visualize the phase structure of the dipole nonlinear output by taking its interference pattern with a tilted broad beam. The initial IP structure of the dipole is preserved in the central two peaks, while the tails along the dipole direction show signs of the OOP relation between adjacent peaks as the fringes tend to break and shift, as if to match the Bloch modes at the M points of the first band (OOP along the dipole direction [13]).

When the two beams exiting the interferometer are made to be OOP with each other while keeping all other experimental conditions unchanged, we also observe self-trapping of a dipole-like structure [Figs. 2(c) and 2(d)]. The OOP dipole appears to have much longer "tails" along the principal axes. Due to destructive phase relation, the linear spectrum of the diagonally excited OOP dipole covers the four M points [Fig. 2(c)]. Under nonlinear propagation, the spectrum reshapes and the energy transfers quickly to the regions close to the four M points where diffraction is anomalous [Fig. 2(d)]. It can be clearly seen that the dipole has an OOP or "staggered" phase structure not only for the central two peaks but also for any two adjacent peaks in the tails along the dipole direction [Fig. 2(d), bottom], characteristic to Bloch modes at M points of the first band [13].

These observations are compared with our numerical simulations with the initial conditions similar to those of the experiments. The model is similar to that used in [13] but here a self-defocusing nonlinearity is employed. Figure 3 shows the simulation results of the dipole-like structure under diagonal excitation for the IP case (left) and the OOP case (right), corresponding to experimental results in Fig. 2. Excellent agreement can be seen for a propagation distance up to 10 mm (i.e., our crystal length). Although we cannot observe a significant difference between linear and nonlinear propagation within our crystal length, simulations with a longer distance of 40 mm (Fig. 3, bottom panel) clearly show the self-trapping of the gap soliton states. Simulations also show that the spectrum in Fig. 3(b) tends to settle into regions close to the four M points as in Fig. 3(d), and the IP dipoles are more robust than the OOP dipoles under diagonal excitation.

Next, the dipole orientation is changed from diagonal to vertical so as to excite the two next-to-nearest waveguides [see the two green spots in Fig. 1(a)]. Results are presented in Fig. 4. In this case, the linear spectrum of the IP dipole covers the two M points in the horizontal direction, with visible excitation also in regions close to the two M points in the vertical direction [Fig. 4(a)]. Under self-defocusing nonlinearity, the power grows quickly in regions close to these four M points where diffraction is anomalous [Fig. 4(b)]. In contrast, the linear spectrum of the OOP dipole covers only the two M points in the vertical direction [Fig. 4(c)]. With the nonlinearity, the power

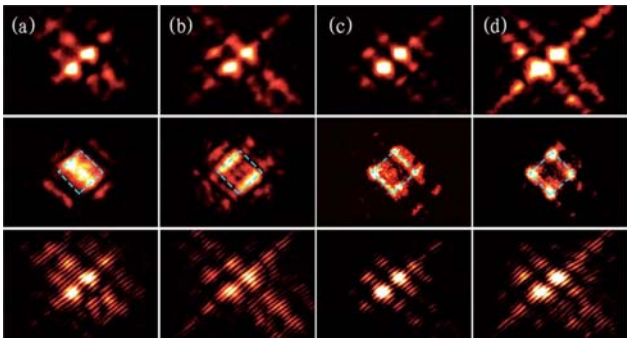

Fig. 2. (Color online) Experimental results on IP (a), (b) and OOP (c), (d) dipole-like gap solitons under diagonal excitation. Shown are output patterns (top), corresponding Fourier spectra (middle), and interferograms (bottom) for linear (a), (c) and nonlinear (b), (d) propagation.

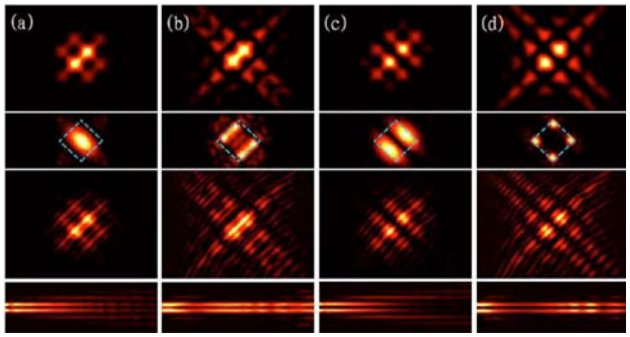

Fig. 3. (Color online) Numerical results obtained by using parameters corresponding to those of Fig. 2. Bottom row: simulation to a longer propagation distance of 40 mm (i.e., 4 times longer than the crystal length).

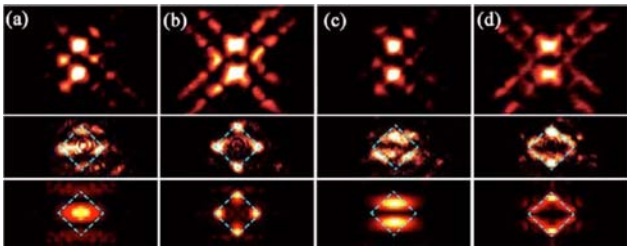

Fig. 4. (Color online) Experimental (rows 1, 2) and numerical (row 3) results on IP (a), (b) and OOP (c), (d) dipole-like gap solitons under vertical excitation. Shown are output patterns (row 1) and corresponding spectra (rows 2, 3) for linear (a), (c) and nonlinear (b), (d) propagation.

grows mainly in regions close to these two points [Fig. 4(d)], but transferring to regions close to the other two horizontal M points is clearly visible as a result of nonlinear k-space evolution [9]. Numerical results for a spectrum with the same propagation distance are shown at the bottom of Fig. 4 for comparison. Simulations to longer distances show that the OOP dipoles are more robust than the IP dipoles under vertical excitation.

Experimentally, it is a challenge to study the stability of these self-trapped dipole structures due to a limited propagation distance (crystal length). We have thus investigated this issue by linear stability analysis for the dipole GS solutions found corresponding to experimental observations. Our analysis shows that the IP nearest dipoles and OOP next-to-nearest dipoles have stability regions in defocusing lattices, whereas the OOP nearest dipoles and IP next-to-nearest dipoles are always linearly unstable. These soliton solutions and corresponding maximal growth rates [maximum real part Re(λ) of the linearization eigenvalues] as a function of the propagation constant μ is illustrated in Fig. 5, where regions of zero growth rate [max(Re(λ))=0] indicate the stability of the dipole solutions. These results show that the nearest IP dipole can be stable (for $4.2 \leqslant \mu \leqslant 4.91$) but the OOP one cannot, in sharp contrast to the self-focusing case [12]. The intuitive picture for such differences might be that in the focusing case the dipole solitons arise from modes at Γ points of the first band, which have a uniform phase, in favor of stable OOP dipole solitons, but in the defocusing case the solitons arise from modes at M points of the first band, which have a checkerboard phase structure [13], thus in favor of stable IP dipole-like GSs. Such stability properties are consistent with earlier analysis based on a staggering transformation with a discrete model [14].

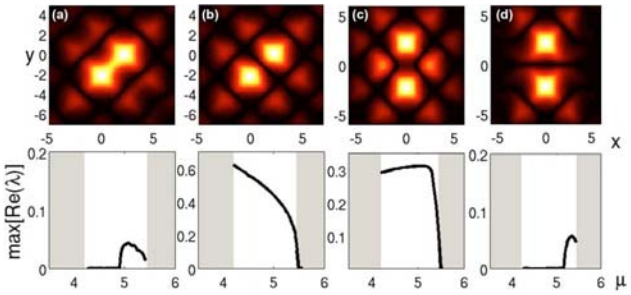

Fig. 5. (Color online) Soliton solutions (top) and stability curves (bottom) for nearest IP (a) and OOP (b), and next-to-nearest IP (c) and OOP (d) dipole gap solitons. Zero growth rates in (a), (d) indicate the stable regions of the dipole solutions.

In summary, we have demonstrated dipole-like spatial gap solitons in a 2D self-defocusing waveguide lattice. Our experimental observations are supported by theoretical analysis and numerical simulations.

This work was supported by the 973 Program, NSFC, PCSIRT, NSF, and AFOSR.

References

1. D. N. Christodoulides and R. I. Joseph, Opt. Lett. **13**, 794 (1988).
2. H. S. Eisenberg, Y. Silberberg, R. Morandotti, A. R. Boyd, and J. S. Aitchison, Phys. Rev. Lett. **81**, 3383 (1998).
3. Y. S. Kivshar, Opt. Lett. **18**, 1147 (1993).
4. J. Fleischer, M. Segev, N. Efremidis, and D. N. Christodoulides, Nature **422**, 147 (2003).
5. F. Chen, M. Stepić, C. Rüter, D. Runde, D. Kip, V. Shandarov, O. Manela, and M. Segev, Opt. Express **13**, 4314 (2005).
6. G. Bartal, O. Cohen, O. Manela, M. Segev, J. W. Fleischer, R. Pezer, and H. Buljan, Opt. Lett. **31**, 483 (2006).
7. D. Mandelik, R. Morandotti, J. S. Aitchison, and Y. Silberberg, Phys. Rev. Lett. **92**, 093904 (2004).
8. D. Neshev, A. A. Sukhorukov, B. Hanna, W. Krolikowski, and Y. S. Kivshar, Phys. Rev. Lett. **93**, 083905 (2004).
9. C. Lou, X. Wang, J. Xu, Z. Chen, and J. Yang, Phys. Rev. Lett. **98**, 213903 (2007).
10. Z. Chen and K. McCarthy, Opt. Lett. **27**, 2019 (2002).
11. H. Martin, E. D. Eugenieva, Z. Chen, and D. N. Christodoulides, Phys. Rev. Lett. **92**, 123902 (2004).
12. J. Yang, I. Makasyuk, A. Bezryadina, and Z. Chen, Stud. Appl. Math. **113**, 389 (2004).
13. D. Träger, R. Fischer, D. N. Neshev, A. A. Sukhorukov, C. Denz, W. Królikowski, and Y. S. Kivshar, Opt. Express **14**, 1913 (2006).
14. P. G. Kevrekidis, H. Susanto, and Z. Chen, Phys. Rev. E **74**, 066606 (2006).